DNA NANOSTRUCTURE BASED NANOFABRICATION

by

Feng Zhou

B. S. in Macromolecular Science, Fudan University, China, 2010

Submitted to the Graduate Faculty of the

Kenneth P. Dietrich School of Arts and Sciences in partial fulfillment

of the requirements for the degree of

Doctor of Philosophy

University of Pittsburgh

2015

UNIVERSITY OF PITTSBURGH

KENNETH P. DIETRICH ARTS AND SCIENCES

This dissertation was presented

by

Feng Zhou

It was defended on

December 10th, 2015

and approved by

Jill Millstone, PhD, Assistant Professor, Department of Chemistry

David Waldeck, PhD, Professor, Department of Chemistry

Lei Li, PhD, Assistant Professor, Department of Chemical and Petroleum Engineering

Dissertation Advisor: Haitao Liu, PhD, Assistant Professor, Department of Chemistry

DNA NANOSTRUCTURE BASED NANOFABRICATION

Feng Zhou, PhD

University of Pittsburgh, 2015

DNA NANOSTRUCTURE BASED NANOFABRICATION

Feng Zhou, PhD

University of Pittsburgh, 2015

Recent advances in DNA nanotechnology make it possible to fabricate arbitrarily-shaped 2D and 3D DNA nanostructures through controlled folding and/or hierarchical assembly of up to several thousands of unique sequenced DNA strands. Both individual DNA nanostructures and their assembly can be made with almost arbitrarily-shaped patterns at a theoretical resolution down to 2 nm. Furthermore, the deposition of DNA nanostructures on a substrate can be made with precise control of their location and orientation, making them ideal templates for bottom-up nanofabrication. However, many fabrication processes require harsh conditions, such as corrosive chemicals and high temperature. It still remains a challenge to overcome the limited stability of DNA nanostructures during the fabrication process.

This dissertation focuses on proof-of-principle studies to transfer the structural information of DNA nanostructure to various kinds of materials. Specifically, Chapter 2 reports the mechanistic study of a DNA-mediated vapor-phase HF etching of SiO_2. Based on the mechanistic studies, we identified conditions for high contrast (> 10 nm deep), high resolution (*ca.* 10 nm) pattern transfer to SiO_2 from DNA nanostructures as well as individual double stranded DNA. Chapter 3 reports the use of a DNA nanostructure as a template for high temperature, solid-state chemistries. By using a thin film of Al_2O_3, programmably-shaped carbon nanostructures were obtained by a shape-conserving carbonization of DNA nanostructures.

Chapter 4 reports a simple but robust method to obtain a free-standing 3D DNA nanostructure on a solid substrate by absorbing uranyl acetate onto a DNA frame followed by lyophilization. Additionally, the resulting DNA nanostructure shows a surprisingly high mechanical strength. This study is the first report on the mechanical properties of a free-standing 3D DNA nanostructure.

TABLE OF CONTENTS

LIST OF TABLES

LIST OF FIGURES

PREFACE

First and foremost, I would like to take this opportunity to express my sincere gratitude to my research advisor Prof. Haitao Liu for all of his support and guidance during my time at University of Pittsburgh. He has given me a firm grounding in the process of my scientific research since my first day in this lab. His knowledge, attitude and enthusiasm always inspire me throughout my graduate study. He also provided me numerous professional guidance and personal support. His patience and consideration makes me feel better when I had to work remotely from China and San Francisco. I would also like to thank Haitao for helping me to improve my writing and presenting skills. Thanks again.

My gratefulness also goes to Prof. Jill Millstone, for all of her time and invaluable advices on my comprehensive exam, proposal preparation and PhD defense. Talks with her always help me understand the fundamental challenges in nanoparticle research and guide me to dig deeper.

I would like to thank Prof. David Waldeck for his time and support as my comprehensive exam and PhD defense committee member.

I would like to thank Prof. Lei Li for his time and support during collaboration and as my PhD defense committee member.

I would also like to thank Prof. Alexander Star, Prof. Daniel S. Lambrecht for their time and questions during my proposal defense.

I am deeply grateful to all my collaborators Prof. Peng Yin, Prof. Shichao Zhao, Dr. Sumedh P. Surwade, Dr. Guomei Zhang, Dr. Wei Sun, Dr. Jie Chen, Dr. Zhiting Li, Karen B. Ricardo, Yongjin Wang, Andrew Kozbial and Muhammad Salim for their great work and contribution to the publications. I also thank my other group members Dr. Cheng Tian, Dr. Raul Garcia Rodriguez, Hyojeong Kim, Anqin Xu, Mina Kim, Justin Hurst, Christopher Kurpiel and Dong Wang for their help and suggestions in my graduate study. I would also like to thank the undergraduate researchers Alexander Hess, Can Cui, Ganesh Shenoy, David Parobek and Brian Michael for their time and efforts while working with me.

I would like to specially thank Dr. Joel G Gillespie for his time teaching and helping me on various characterization techniques throughout the past four years. His valuable suggestions are reflected in all my publications so far.

Finally, this dissertation would not be possible without the support from my family. My parents, Zhongchao Zhou and Xianghua Tang, have provided me numerous supports and great advices in both career and life. They deserve the most credits. I would also like to thank my wife Hao Bai. She is a talented woman who shares insightful ideas with me. She is also a good wife who makes my out-of-lab life colorful. Last but not the least, I want to thank my daughter, Sherry Zhou, for the joyful and rewarding life she brought to me.

1.0 INTRODUCTION

1.1 STRUCTURAL DNA NANOTECHNOLOGY

Over the past several decades, DNA has drawn dramatic attention in material science as structural building blocks. Due to the specificity of base pairing, single stranded DNA (ssDNA) can recognize another strand with a complimentary sequence, producing a predictable DNA nanostructure. Thanks to the programmability of the DNA hybridization, both arbitrary and robust nanostructures with accurate features and a precision of 2-3 nm in dimension can be constructed[1-7] at cost as low as \$6 per m^2.[8] The size of individual 2D and 3D DNA nanostructures can vary from tens of nm to several microns.[9-11] As for the self-assembly of a 2D DNA lattice, up to 1 mm in size has been reported.[12] Furthermore, the deposition of DNA on substrates has been studied to obtain precise control of the location and orientation, which makes it an ideal template for nanofabrication.[13-15] These unique properties of DNA have made it an attractive template for micro- and nanoscale fabrication.

The following sections provide an overview of recent progresses in the fabrication of DNA nanostructures.

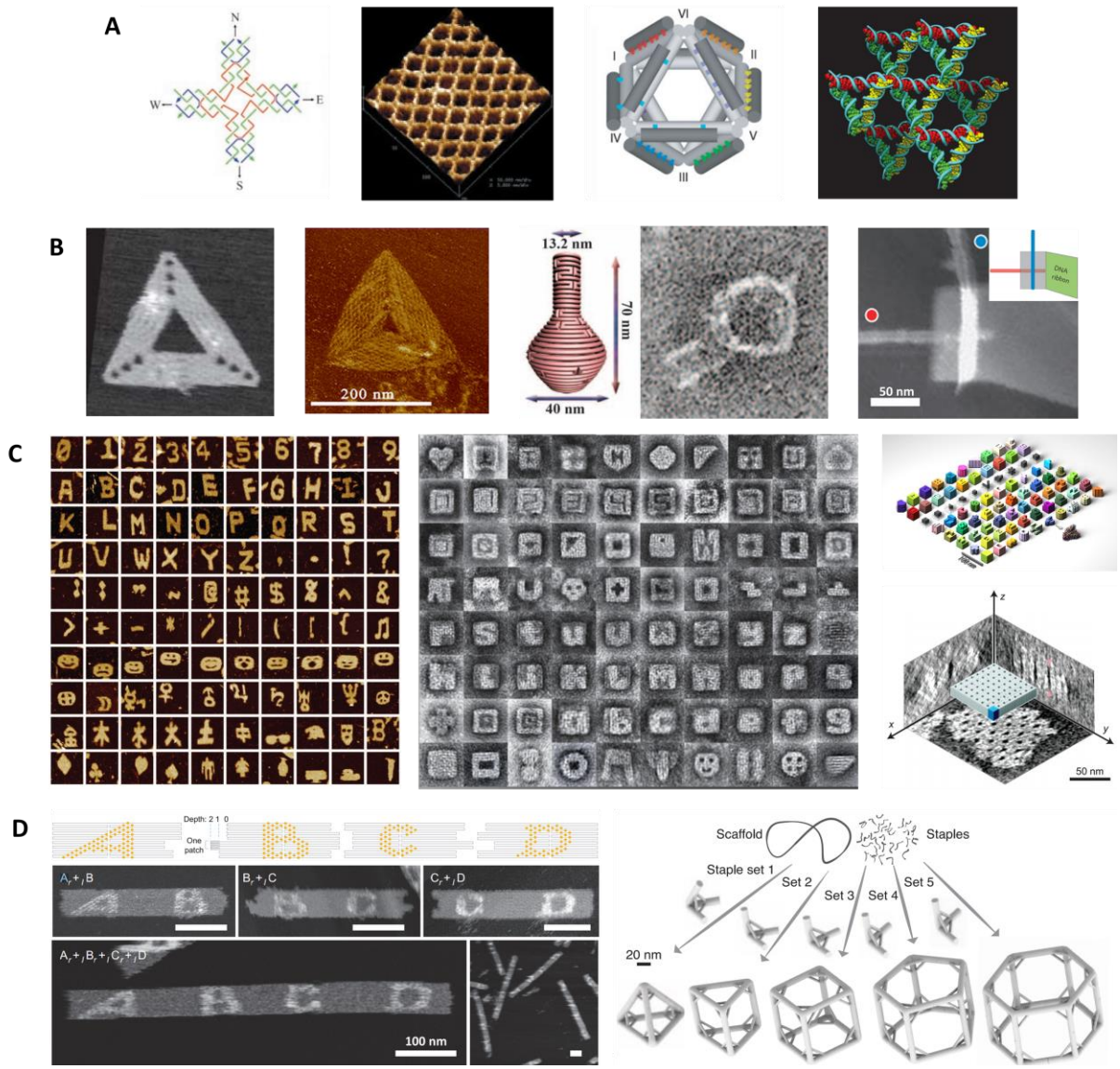

Figure 1: Examples of structural DNA nanotechnology A. DNA tile based self-assembly. The 4 × 4 tile strand structure (left), 2D lattices formed from the 4 × 4 tiles (centre left), a1.7-kilobase single-stranded DNA that folds into a nanoscale octahedron (centre right) and the self-assembled 3D DNA crystal (right). B. DNA origami. Triangular DNA origami folded from single-stranded M13mp18 (left), folded from the fractions of double-stranded λ DNA (centre left), DNA nanoflask with complex curvatures (centre right pair) and DNA origami for assembly of carbon nanotubes (right). C. Self-assembly of DNA single stranded tiles. AFM images of complex 2D shapes self-assembled from single stranded DNA tiles (left), TEM projections of complex 3D structures self-assembled from DNA bricks (centre), computer-generated 3D models of structures in centre (right top) and Cryo-EM 3D reconstruction images of two-dimensional DNA pore crystals (right bottom). D. Self-assembly using DNA nanostructures. Recognition based on complementarity of origami edge shapes (left) and self-assembly of DNA origami polyhedra from DNA tripods (right). Figures reprinted with permission from: A. ref. 19, © 2003 AAAS (left and centre left), ref. 23, © 2004 NPG (centre right), ref. 11, © 2009 NPG (right); B. ref. 9, © 2006 NPG (left), ref. 10, © 2012 ACS (centre left), ref. 6, © 2011 AAAS (centre right pair), ref. 37, © 2009 NPG (right); C. ref. 38, © 2012 NPG (left), ref. 40, © 2012 AAAS (centre and right top), ref. 41, © 2014 NPG (right bottom); D. ref. 45, © 2011 NPG (left), ref. 4, © 2014 AAAS (right).

1.1.1 DNA tile based self-assembly

In 1982, Nadrian Seeman pioneered the idea of creating a mechanically robust tile structure containing 4 single-stranded DNA to form a four-way branched junction (also called a tile structure), opening the era of DNA nanotechnology.[16] In this concept, four individual ssDNA associate into a four-arm junction, with complementary portions in a specific pattern to maximize the number of correct base pairs. Since then, many periodic structures, such as 2D lattice arrays, have been assembled using the tile structure as repeating units.[17-19] In 1993, Tsu-Ju Fu and Nadrian Seeman developed the double-crossover DNA tile,[20] containing two parallel double helical domains with individual strands crossing between the domains at crossover points. It was the first mechanically strong DNA structure to form extended 3D nanostructures. Since then, numerous rigid tile structures have been fabricated, such as multi-helix bundles, cross shaped tiles or 3- and 5-point stars, and they have been assembled into 3D DNA nanostructures such as nanotubes,[21, 22] polyhedra,[23, 24] cubes,[25] crystals[11] and buckyballs.[26]

1.1.2 DNA origami

In 2006, Paul Rothemund developed the DNA origami method for the first time. The process involves the folding of a long ssDNA (also called as scaffold strand) aided by hundreds of short synthetic ssDNA (also called staple strands).[9] For example, M13mp18, a viral genomic ssDNA and the most widely used scaffold DNA, is mixed with hundreds of staple DNA through a particular design generated by computer programs.[27, 28] Each staple DNA is about 30-50

nucleotides long and specifically designed to complimentarily bind to multiple regions of the scaffold strand, folding the specific regions into desired adjacent positions. After mixing, heating and cooling, the various DNA staples hybridize to the desired locations, pulling the long scaffold DNA into a well-defined 2D structure on a scale of 100 nm. By using a larger scaffold strand, larger DNA nanostructure can be fabricated.[10, 29] In addition to the 2D structures, 3D nano-robot origami[30] and origami with curvatures[6] were also reported. Moreover, the staples DNA can be modified with multiple functional molecules or particles, such as fluorescent peptide markers,[31-33] metal nanoparticles[34-36] and carbon nanotubes,[37] making the DNA origami a perfect host for site-specific nano-patterning of desired material.

1.1.3 Self-assembly of DNA single stranded tiles (DNA bricks)

In 2012, Bryan Wei and Peng Yin demonstrated the use of DNA single stranded tiles as the building blocks for construction of complex DNA nanostructures for the first time.[38] In this concept, the DNA building blocks are similar to inter-locking bricks. Each brick is a single stranded DNA with 42 bases. The single stranded DNA is folded into a block-like structure containing 4 blocks, each of which consists of 10 – 11 DNA bases. Every block can connect to another one if the other block has a complementary sequence. In this way, the blocks can self-assemble to form a structure consisting of any number of DNA blocks. For example, 362 strands were self-assembled into the molecular canvas. Each block has a unique DNA sequence and each block has specific location within the 362 blocks structure, like a pixel. To design a specific structure, all that must be done is to remove the desired strands from the pool. After self-assembly, more than 100 shapes of DNA nanostructures were obtained, such as rectangular ring,

alphabetic letters and eagle head. The same concept was also reported by Divita Mathur and Eric Henderson in the same year.[39]

In addition to the 2D nanostructure, the self-assembly of DNA single stranded tiles also allows the building of 3 dimensional structures using DNA bricks, as reported by Yonggang Ke and Peng Yin.[40] In this case, each DNA brick is 32 DNA bases long, folding as Lego® bricks that have two pins and two holes. The pin of one brick is able to plug into the hole from another bricks, only if the DNA sequences of the two strands are complementary. The bricks connect at the right angles, which allow the structures to be built in 3 dimensions. Under certain conditions, the bricks were self-assembled to form a 3D block construction. Each brick within the block construction has a unique DNA sequence and fits only one location within the block. The block construction can be treated as a 3D canvas which contains over 1000 voxels. Each voxel consists of 8 base pairs of DNA and measures about 2.5 nm. To make a certain shape, bricks are withheld before self-assembly. More than 100 different shapes were built within the 1000 voxel canvas. Furthermore, the block structure can be extended to contain any number of DNA bricks, building micro-scale DNA crystals with prescribed depths.[41] This approach is simple and robust. It could enable the creation of new nanoscale devices with a wide range of applications.[42, 43]

1.1.4 Self-assembly using DNA nanostructures

The DNA nanostructures, constructed using the methods discussed above, can be modified with particular sticky ends, making them "monomers" for subsequent self-assembly to produce larger structures in micro-scale. In 2010, Masayuku Endo and Hiroshi Sugiyama first reported this method for assembling multiple DNA origami structures by using designed 2D DNA origami rectangles, so-called "DNA jigsaw pieces".[44] Each single DNA jigsaw piece contains concave

and convex connectors, which are designed to be shaped and sequence complementary as the sticky ends for selective connection. Three to five different DNA jigsaw pieces could be assembled into the desired nanostructure with the correct alignment. A similar concept was also demonstrated by Woo and Rothemund, to assemble the 2D DNA origami by controlling the geometric arrangement of blunt end stacking interactions.[45]

In addition to 2D nanostructure, large and stiff wireframe DNA polyhedral could be constructed by hierarchical assembly of certain number of three-arm-junction DNA origami tile motif (tripod).[46] Each tripod was assembled from scaffold and staple strands DNA to form precisely controlled inter-arm angles and arm lengths. At the end of each tripod, 30-base strands were designed for connection between two adjacent tripods, serving as sticky ends for inter-monomer connection. Without intermediate purification, the tripods can assemble into the polyhedron. This simple strategy provides a general approach for high yield construction of open wireframe polyhedra.

1.2 LIMITED STABILITY OF DNA NANOSTRUCTURES FOR NANOFABRICATION OF INORGANIC MATERIALS

In general, DNA nanostructures are constructed by the hybridization between complementary base sequences to form double stranded DNA (ds-DNA) at specific locations. Thus, the nature of this non-covalent interaction limits the chemical stability of DNA nanostructure, which could unwind and separate into single stranded DNA (ss-DNA) under certain conditions, or so-called DNA denaturation. Moreover, the DNA nanostructure is organic and can degrade under harsh conditions, such as high temperature and oxidative environment. Finally, the DNA is generally

considered as a soft material and there is even no report on the mechanical properties of 3D DNA structures in a dry state. Consequently, most fabrication methods, such as reactive ion etching and lithography, cannot utilize DNA nanostructures as a direct template because it wouldn't survive these procedures. In conclusion, DNA based nanofabrication of inorganic materials still faces significant challenges.

The following sections provide a review of DNA structural stabilities under various fabrication conditions.

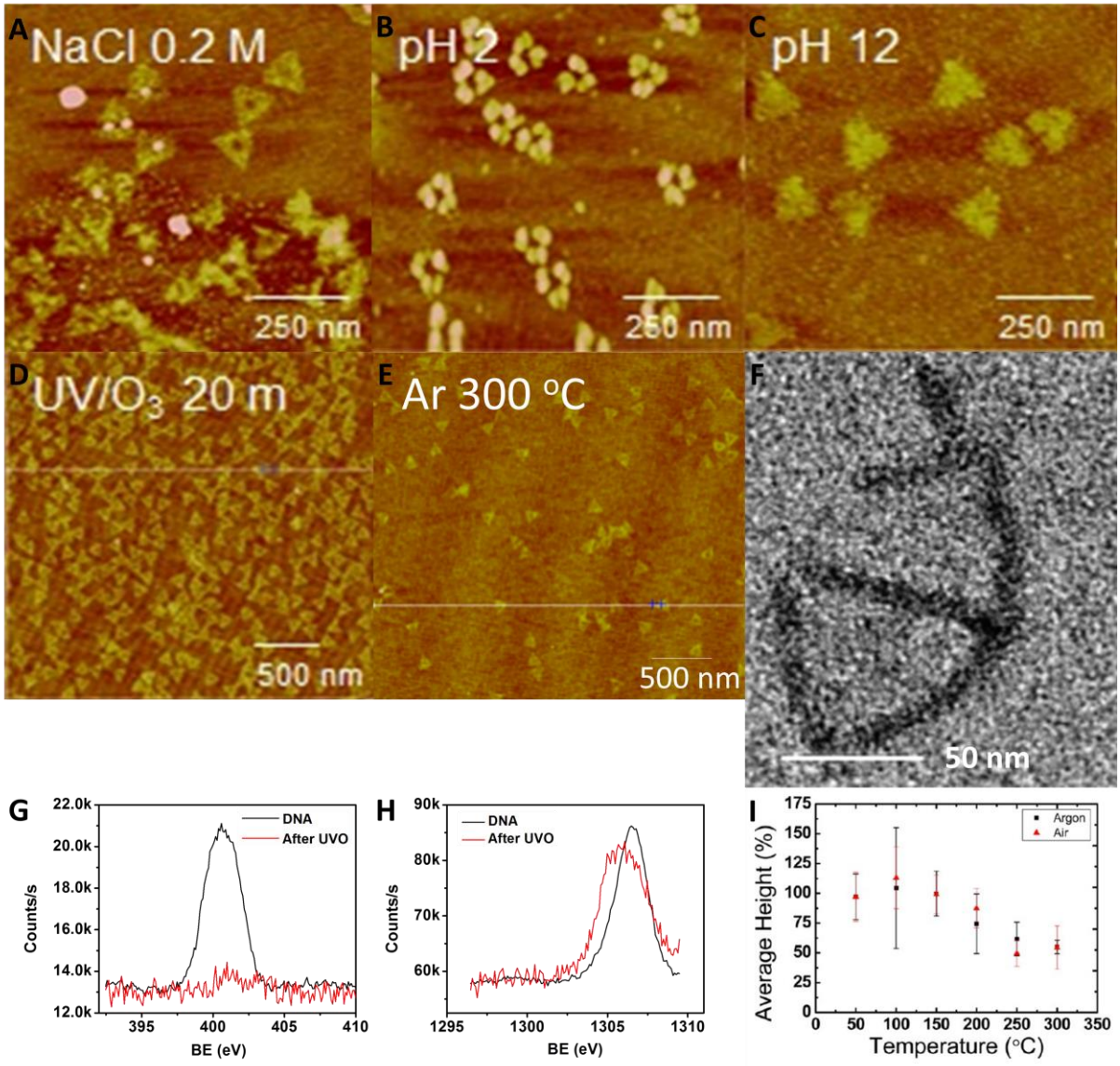

Figure 2. Limited stability of DNA nanostructures. Deformation of triangular DNA origami in 0.2 M NaCl solution (A), acidic (B) and basic (C) solution. Salt residue structures after UV/O_3 treatment (D) and annealing in Ar at 300 ^{o}C for 10 min (E). (F) Ruptured DNA tetrahedron on a TEM grid. The XPS peaks of N1s (G) and Mg2s (H) before and after UV/O_3 treatment proved that the nanostructure after UV/O_3 in D consisted only of salt, with no DNA left. (I) showed that the decomposition of DNA occurred gradually at elevated temperatures. Figures reprinted with permission from: ref. 49, © 2014 ACS (A-E and I); ref. 84 (F); ref. 52, © 2015 ACS (G and H).

1.2.1 Limited chemical stability of DNA nanostructure

Most DNA nanostructures are fabricated in aqueous solution at a neutral pH and the presence of a buffer. Other than the complementarity of the binding sequences, the ions in the buffer solution, such as Mg^{2+}, also play an important role to screen the DNA backbone repulsion, allowing the DNA to self-assemble, and to stabilize the branched junctions of the nanostructure.[47] It is also known that hydrolysis occurs under extreme pH, resulting in denaturation or degradation of ds-DNA.[48] After deposition onto a solid phase substrate, such as Si and mica, the DNA nanostructures are immobilized onto the surface by electrostatic interaction between the phosphate backbone of DNA, the substrate surface, and absorbed ions. The change in composition and pH of the solution can all affect the structural stability of DNA nanostructures.

A recent study showed that after immersing the as-deposited DNA triangles in deionized water, the density of the DNA nanostructures was significantly decreased and the structures were severely damaged due to the desorption of Mg^{2+}.[49] In another experiment, most of the DNA triangles deformed into three trapezoidal sides with an irregular height after immersion into a NaCl solution. The Na^{+} is believed to replace the absorbed Mg^{2+} and accumulate on the deformed DNA nanostructures.

In the case of pH, it is reported that the hydrolysis of glyosidic bonds in DNA mainly occurs in acidic pH range.[50, 51] Another report also showed that the as-deposited triangular DNA origami underwent a deformation in pH lower than 4 or higher than 12, limiting its usage in wet-etching processes.[49]

The DNA nanostructure is also structurally labile under oxidative conditions due to its nature as an organic molecule. The chemical integrity of a dried DNA triangle is devastated after

exposure under UV/O_3 environment for 15 min.[49, 52] DNA nanostructures will also be instantly destroyed under most O_2-mediated plasma processes, such as atomic layer deposition (ALD) and dry etching of Si.[53] In summary, the application window for DNA nanostructures is strictly limited by its labile chemical stability.

Tremendous efforts have been made to overcome the limited chemical stability of DNA nanostructures. Metallization is the most widely used approach to preserve DNA nanostructure during DNA-based nanofabrication.[2, 43, 54-63] The resulting metalized nanostructures have been further used as template masks for patterning the underlying substrate, such as shadow nanolithography of silicon by wet-etching,[62] and as nano-patterning of graphene by O_2 plasma.[43] However, the faithful pattern transfer process cannot be achieved due to the loss of structural information, such as resolution, of DNA nanostructures from the inevitably used metal absorption.

1.2.2 Thermal stability of DNA nanostructure

The construction of DNA nanostructures usually involves annealing and cooling for base sequences to be paired complementarily. At elevated temperature, the hybridization of nucleic acids in ds-DNA is weakened and the structural information of the DNA nanostructure cannot be maintained. In solution, the denaturation temperature of ds-DNA varies from 40 °C to 100 °C, depending on the base sequence and the buffer composition.[64] After deposition onto a substrate, such as mica and Si, the electrostatic interaction between the phosphate backbone and the substrate provides additional support for the DNA nanostructure, improving the structural stability. Thermogravimetric analysis (TGA) of a salmon DNA film under nitrogen, conducted by Aoi *et al.*, showed that the decomposition of bulk DNA started at 230 ^{o}C with a residual

weight of 53% after heating to 500 ^{o}C.[65] Another study showed that triangular DNA origami likely thermally decomposed on heating beyond 250 ^{o}C in argon, but the triangular features were preserved even after heating at 300 ^{o}C.[49] In addition, XPS data proved that the remaining triangular structures were inorganic residue (*e.g.*, Magnesium Phosphate),[52] confirming the decomposition of the DNA nanostructure. It is thus not surprising that almost all reported DNA-based nanofabrications are either based on solution chemistry or conducted at close to room temperature.[2, 42, 52, 54-56, 59, 61-63, 66-70] Challenges need to be addressed on the limited thermal stability of DNA nanostructures for nanofabrication at high temperature, such as ALD (> 150 ^{o}C) or carbonization (> 500 ^{o}C).[71-73]

1.2.3 Mechanical stability of DNA nanostructure

DNA nanostructures are soft materials and their applications have long been limited to aqueous environments. The persistence length and Young's modulus of ds-DNA is *ca.* 50 nm and 100 - 300 MPa, respectively.[46, 74-76] An individual double helix can be pulled apart with a force of about 10 to 15 pN or partially untwisted after stretching under 60 pN.[76] The DNA origami bundled with multiple double helixes is more rigid. For a bundle of 4 to 8 ds-DNA, the persistence length increased from 740 nm to 3.5 μm;[77, 78] however, the Young's modulus becomes smaller: 112 - 126 MPa for bending modulus[77, 78] and 75 – 180 MPa for radical modulus.[46] As for the 3D DNA nanostructure, such as the DNA polyhedral, nanopillar and hierarchical structures, they would deform irreversibly with a threshold force of tens to hundreds of pN in water.[24, 34, 77, 79] Further complications arise during drying the DNA nanostructures. Due to the strong surface tension of water, a 3D DNA structure cannot withstand the capillary forces or transverse sheer forces; upon drying, these structures inevitably collapse or rupture.[80] For this

reason, the characterization of 3D structures of DNA have been limited to specialized characterization methods, such as cyro-EM,[23, 26, 81-84] and super resolution fluorescence microscopy[46] that can probe the structure in aqueous solution. Due to these challenges, no studies on the mechanical properties of DNA nanostructure in a dry state have been reported.

In summary, it still remains a challenge to overcome the lack of stability while using DNA nanostructure as a general-purpose template for nanofabrication. This dissertation will highlight my research in addressing this challenge and developing DNA nanostructure-based nanofabrication.

1.3 VAPOR-PHASE HF ETCHING OF SIO_2 AND USE OF DNA NANOSTRUCTURE

Vapor-phase etching of SiO_2 using HF gas is the reaction between SiO_2 and HF to produce SiF_4 and H_2O:

$$SiO_2(s) + 4HF(g) \rightarrow SiF_4(g) + 2H_2O(g)$$

$$6\,HF + 3\,H_2O \rightarrow 3\,HF_2^- + 3\,H_3O^+ \text{ (deprotonating)}$$

$$3\,HF_2^- + 3\,H_3O^+ + SiO_2 \rightarrow 2\,HF + SiF_4 + 5\,H_2O \text{ (etching)}$$

Although there are several kinetic mechanisms,[85-87] it is generally accepted that this reaction occurs after an initiation step by condensation of HF and water on the SiO_2 surface. Theoretical calculations based on quadratic configuration interaction also showed that the barrier for a rate-limiting step of concerted HF/H_2O etching mechanism was 13 kcal/mol lower than that for etching by HF alone.[88] Since H_2O is produced and accumulated during the reaction, the overall reaction is autocatalytic. A higher vapor pressure of H_2O can usually achieve significant

etch rates during the reaction. Thus, the difference in the concentration of H_2O would make a big difference in the selectivity of the SiO_2 etching rate.

In view of this reaction, there are other parameters, such as the amount of HF and *iso*-propanol, the reaction temperature and etching time, that can affect the etching rate. Basically, lower temperature, longer time and higher pressure of HF would increase the overall etching rate. As for *iso*-propanol, it can form a monolayer on top of water layer which could result in a smoother surface.[89] However, its effect on the etching rate is complicated, in that it can increase the etching rate at the beginning and then decrease it during the increase of its partial pressure.

In terms of selectivity of HF etching SiO_2 in the presence of a DNA nanostructure, there are two major factors to be considered. Firstly, there is a difference in H_2O adsorption between DNA and SiO_2. On SiO_2, there is always a water monolayer even if the relative humidity of H_2O is close to zero. Besides, the amount of absorbed water only increases by 40% when the relative pressure increases from 0 to 0.85.[90] However DNA shows a much higher response to increases in relative humidity than SiO_2 does.[91] Secondly, since the DNA was anchored on SiO_2 based on electrostatic interaction mediated by Mg^{2+}, the HF ionization efficiency might be affected by the adsorbed ions,[92] which could change the etching rate of SiO_2.

All of the above information suggests that it would be a multi-dimensional optimization procedure to obtain the best pattern transfer condition with large contrast, smooth surface, and high fidelity. Herein, we describe how we optimize the etching condition to improve the contrast of the pattern and summarize the quantitative relationship between the parameters in the etching procedure. We expected that deep trenches and a smooth surface could be achieved at the optimized condition. Further application was also studied to obtain successful pattern transfer on a Si [110] substrate by using the patterned SiO_2 as a template.

1.4 POROUS CARBON MATERIAL AND DNA NANOSTRUCTURE

Porous carbon material plays an important role in a wide range of applications, such aerospace structure, thermal management, and energy storage because of its unique mechanical, thermal, and electrical properties.[93-100] The carbon structure has an essential effect on these properties. Therefore, to control the structure becomes the key point to put porous carbon material into application. Currently, uniform structured porous carbon materials are synthesized using inorganic templates.[101-104] The template can guide an organic precursor, usually a polymer, into the desired structure. The organic-inorganic composite then undergoes a carbonization process at high temperature (typically 500 – 1000 ^{o}C) during which the organic precursor is converted to carbon (amorphous or crystalline). The shape of the inorganic template is transferred to the porous carbon material during the carbonization process. The inorganic template controls the porous carbon material's structure. However, the inorganic templates can only offer simple structures, such as spheres and rods, limiting the performance of porous carbon materials.

Thanks to the programmability of DNA hybridization, arbitrarily-shaped 2D and 3D DNA nanostructures have been made with precise control of size and shape at high resolution.[3, 4, 9, 56, 105-113] These DNA nanostructures are ideal templates for making porous carbon materials to carry out design-based applications. It has been reported that DNA can be converted to graphitic structures through carbonization.[114, 115] However, investigation in terms of shape control during DNA carbonization has not been reported. A method to preserve the structural information of DNA nanostructure through carbonization, therefore, is needed.

1.5 HIGH-STRENGTH LOW-DENSITY METAMATERIAL AND DNA NANOSTRUCTURE

The history of architecture is the history of development of structures and materials to achieve high strength and high space efficiency. The Great Pyramids of Giza, built about 5000 years ago, is analogous to bulk material. It's the largest man-made stone monument, about 147 m in height and 5.75×10^6 tons in weight. In 1887, the Eiffel Tower was constructed from only *ca.* 10^4 tons of material, including 7300 tons of iron. Its height, 324 m, is twice as tall as the pyramid. The structural advantage of this high-strength and low-density building is the consequence of the development of both the iron alloy material and hierarchical hollow framework structure. For the past century, tremendous efforts have been made to create materials and structures that are of both low density and high mechanical strength. However, for bulk materials, strength is correlated with density; as a result, lowering the density can drastically impair the mechanical properties.[116-120] Various approaches have been made to address this challenge.[121-132] Among them, one promising solution is to design micro- or nano-scale hierarchical structures, such as mechanical metamaterials,[121] metallic microlattices,[122, 123] ceramic composite trusses,[124] ceramic nanolattices,[126] carbon fiber-reinforced polymer lattices,[128] and TiN nanotrusses.[130, 131] Advances in micro- and nano-fabrication procedures, such as polymer wave-guides, micro-stereolithography and direct laser writing two photon lithography techniques, have made it possible to precisely control the 3D lattice geometry. For example, polymer- and metal-based hierarchical structures have been fabricated by dual-beam photo-lithography; these materials showed very high strength (modulus ~200 MPa) at low density (< 100 kg/m^3).[126] However, with the exception of surface coating,[124] the critical features of these hierarchical structures are

currently limited at micro-scales. The mechanical property of nanoscale hierarchical structures is largely unexplored.

DNA nanotechnology is capable of producing a wide range of nanostructures with programmable structure, size, molecular weight and sub-5 nm resolution.[4, 9, 11, 24, 25, 34, 38, 40, 41, 46, 81, 130, 133-136] Among those nanostructures, wireframe DNA polyhedral are of particularly interest, due to their high-resolution features with low density and promising applications as hierarchical lattice cell for nano-architecture. Due to these unique features, DNA nanostructures could serve as an ideal model system to understand the structure-property relationship of low-density materials. However, DNA nanostructures are soft materials and their applications have long been limited to aqueous environments. Further complications arise when drying the DNA nanostructures due to the strong surface tension of water. These challenges limited the application of DNA nanostructures in the field of mechanical applications.

2.0 MECHANISTIC STUDY OF THE NANOSCALE NEGATIVE-TONE PATTERN TRANSFER FROM DNA NANOSTRUCTURES TO SiO_2

2.1 CHAPTER PREFACE

Materials contained in this chapter were published as a research article in *Chemistry of Materials*; figures used in this chapter have been reprinted with permission from: *Chemistry of Materials*, **2015**, *27 (5)*, 1692-1698 (listed as reference 53 in bibliography section).

List of Authors: Feng Zhou, Brian Michael, Sumedh P. Surwade, Karen B. Ricardo, Shichao Zhao, and Haitao Liu

Author Contributions: F.Z. and H.L. designed and directed the experiments. F.Z., B.M., and K.B.R. conducted the experiments. All authors discussed the results. F.Z. and H.L. wrote the manuscript with input from all authors.

2.2 INTRODUCTION

In recent years, research in DNA nanostructures has developed to a stage where arbitrary-shaped and mechanically-robust nanostructure can be constructed[1-7, 137] with a theoretical precision of less than 5 nm at a cost as low as $6 per square meter.[138] The deposition of DNA nanostructures on the substrates has been demonstrated with precise control over their location and orientation, making them ideal templates for high resolution, low cost nanofabrication.[13-15] However, the pattern transfer from DNA nanostructures to inorganic substrates remains a bottleneck of this area of research. Tremendous efforts were dedicated to overcome the lack of chemical stability of DNA and the inadequate adhesion interaction between DNA and the substrate.[139]

Metallization is the most widely used approach to DNA-based nanofabrication. Solution phase metallization of λ-DNA was first demonstrated by Sivan and coworkers.[54] Recently, the metallization of different metals, such as Ag, Cu, Ni and Au on DNA strands and DNA nanostructures has been demonstrated.[2, 55-57] In addition to metal deposition onto the whole nanostructure, site-specific metallization was also made possible by modifying DNA nanostructure with binding sites that accept DNA-modified Au or Ag nanoparticles.[58-60] In addition to these solution phases approaches, vapor phase deposition of metals onto DNA has also been reported by Mao and Woolley groups. They used DNA to pattern vapor-phase deposited metal and the resulting metal film can be used as a hard mask for patterning the underlying substrate.[61-63]

Our group recently showed that DNA nanostructures can modulate certain surface reactions to result in a faithful pattern transfer from the DNA nanostructures to an inorganic substrate.[42, 140] In one of the studies, DNA was shown to have a local effect on the vapor phase HF etching to result in a direct negative-tone and positive-tone pattern transfers from DNA to

SiO_2.[140] The fact that DNA can be used to directly pattern SiO_2 carries significant technological significance because SiO_2 is one of the most important hard mask materials for semiconductor nanofabrication.[141]

Although our early study established the vapor phase HF etching as a promising approach to pattern transfer to SiO_2, several important scientific and technical questions were left unanswered. Specifically, the mechanism of the modulation effect of DNA has not been firmly established although it was hypothesized that adsorption of water vapor on the surface plays an important role.[140] In addition, the kinetic behavior of the reaction has not been extensively explored and as a result, the reaction conditions for pattern transfer have not been optimized for high resolution and contrast. As a result, the pattern transfer typically produced trenches (ridges) that are only 2 – 3 nm in depth (height).[140] For practical applications, a much higher vertical contrast is needed. In a similar vein, the lateral resolution of the pattern transfer was limited to *ca.* 17 nm. Although this is an impressive resolution, it is on par or worse than that of the state-of-the-art photolithography and electron-beam lithography.

The present work aims to address these challenges by characterizing the detailed kinetic behavior of the DNA-mediated HF etching reaction. In addition to probing the mechanism of the DNA-mediated HF etching, the kinetics studies also produce a set of design rules that can be used to guide the optimization of reaction conditions for high resolution, high contrast pattern transfer. Our result shows that DNA promotes the vapor phase HF etching of SiO_2 by enhancing the adsorption of water near itself; the organic moieties of DNA make the major contribution to the enhancement effect. Based on these results, we identified optimized pattern transfer conditions that produce high resolution (*ca.* 10 nm), high contrast (> 10 nm) pattern transfer to SiO_2. The SiO_2 patterns generated by DNA can be used as a hard mask for plasma etching of Si

to produce high contrast, high resolution features that are comparable to those produced by electron-beam lithography.

.

2.3 EXPERIMENTAL SECTION

2.3.1 Materials

2.3.1.1 Chemicals

Silicon [110] and Silicon [100] wafers with 300 nm of oxide layer were purchased from University Wafers. Staple and scaffold M13mp18 DNA for preparing the origami[9] were purchased from IDT and New England Biolabs, respectively. The silicon substrate was cleaned with hot piranha solution (7:3 concentrated H_2SO_4: 35% H_2O_2). *Warning: Piranha solution presents an explosion danger and should be handled with extreme care; it is a strong oxidant and reacts violently with organic materials. All work should be performed in a fume hood. Wear proper protective equipment.* Hydrofluoric acid (HF, 48%) was purchased from Mallinckrodt, NJ, USA. *Warning: HF acid is highly corrosive, poisonous and can penetrate through tissues into bones. Symptoms of exposure to HF may not be evident immediately and so it must be handled with extreme care. All work should be performed in a fume hood. Wear proper protective equipment.*

Triangular DNA origami contains three trapezoidal domains and the 2D plate is formed by nine cross-linked double helixes (Figure 3). The nominal height of origami is about the same as the diameter of the DNA helix (2 nm). The width at origami edge was estimated to range from

26 nm to 30 nm, depending on the size of the inter-helix gap.[9] The height and width of DNA origami measured from our AFM images are 1.59 ± 0.18 nm and 28.6 ± 5.2 nm, respectively.

The secondary structure analysis was conducted using the NUPACK software, available at www.NUPACK.org.[142] The temperature was set as 20 ^{o}C. Two single-strand DNA with the same concentration were introduced:

Strand 1(staple DNA, "t-1s30e, G5"[9]):

CGAGAAAGGAAGGGAAGCGTACTATGGTTGCT

Strand 2 (97 unpaired DNA bases and two adjacent 16 bases paired by strand 1):

AGCAACCATAGTACGCGCCCTGTAGCGGCGCATTAAGCGCGGCGGGTGTGGTGGTT

ACGCGCAGCGTGACCGCTACACTTGCCAGCGCCCTAGCGCCCGCTCCTTTCGCTTTC

TTCCCTTCCTTTCTCG

The calculation shows that the 97-base loop forms a secondary structure that is mostly linear (Figure 3).

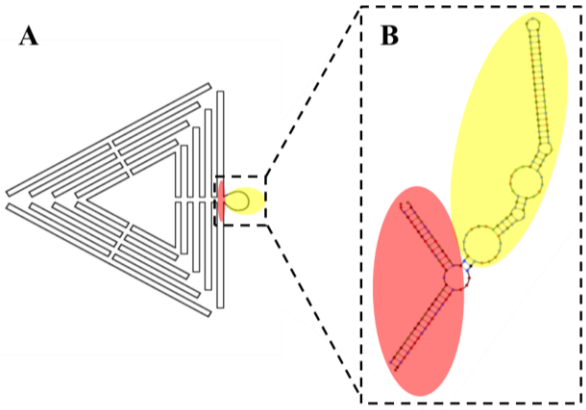

Figure 3. (A) A sketch of triangular DNA origami with a loop on one side and (B) secondary structure analysis of this 97-base loop of the DNA nanostructure. The loop was marked in yellow; the two adjacent 16 bases and the complementary staple DNA were marked in red. Figure A is reprinted from ref. 9 with permission from Nature Publishing Group.

2.3.1.2 Instrumentations

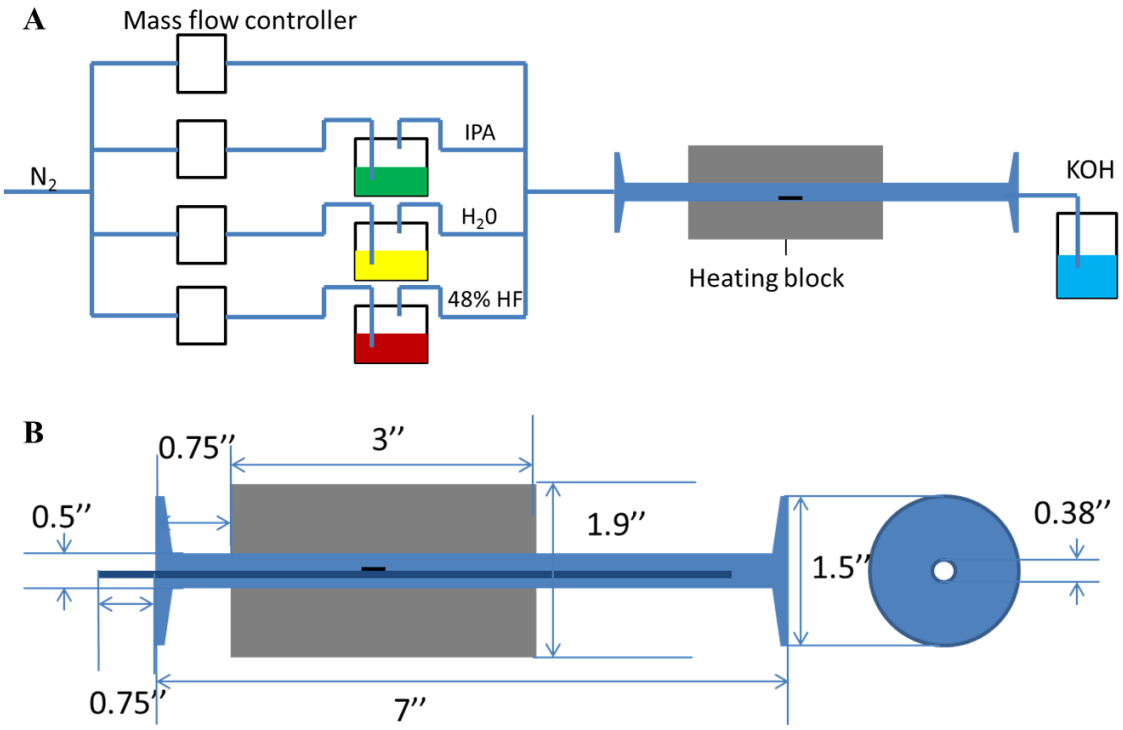

Figure 4. Schematics of (A) The etching setup and (B) details of the etching chamber.

The flow reactor used in this study was homemade (Figure 3) and consists of 3 plastic containers each containing H_2O, *iso*-propanol, and HF (48%), 4 mass flow controllers, and an etching chamber. The mass flow controllers are: FMA-3704 (for HF carrier gas, range 0 - 100 standard cubic centimeter per minute, (sccm)), FMA-5510 (for H_2O and *iso*-propanol carrier gas, range 0 - 200 sccm), FMA 5512 (for dry N_2, range 0 - 500 sccm). The N_2 streams were then combined before it was passed through the etching chamber. The exhaust was scrubbed in a solution of KOH and vented to the ambient. The etching chamber consists of a stainless steel tube, a stainless steel sample holder, an aluminum block, a heating tape (KH-203/5-P, Omega) and a

temperature controller (CNi3222-C24, Omega). The dimension of the reactor was shown in Figure 4. The temperature sensor was located inside the aluminum block to obtain precise control of the temperature of the tube. The fluctuation of the temperature was less than 1℃ within 20 min which was also the typical etching time. On the sample holder, 6 sites were marked with marker pen to ensure consistent placement of the sample.

UV-ozone treatment was carried out in a Novascan® PSD Pro Series UV-Ozone cleaner. Tapping mode atomic force microscopy (AFM) was carried out on a Veeco Dimension 3100 in air. NSC15/AIBS AFM probe (325 kHz, 46 N/m) was purchased from μmasch®. Multiple tips were utilized during the AFM scanning on the same sample to insure accurate measurement of the topography of the sample surface. About 10 to 20 measurements were used to calculate the average value and standard deviation of FWHM and depth of trench. Thickness of SiO_2 were measured using an alpha-SE® Ellipsometer. Plasma etching was conducted using a Trion Technology Orion III Reactive Ion Etching system. X-ray Photoelectron Spectroscopy (XPS) was conducted in the Escalab 250XI XPS microprobe.

2.3.2 Methods

2.3.2.1 DNA/SiO_2 sample preparation.

Two types of SiO_2 substrates were used in this work: Si [100] wafer with a 300 nm thick of thermally-grown SiO_2 layer and Si [100] wafer with a thermally grown SiO_2 layer, typically 15 nm. Here, the 300 nm SiO_2/Si [110] wafer was chosen to conduct the kinetic study because of its uniformity in oxide thickness; the 15 nm SiO_2/Si [110] substrate was used in experiment to obtain further etching on the Si [110] layer.

DNA solution was made from TAE/Mg buffer solution (12.5 mM $Mg(OAc)_2$, 40 mM Tris, 20 mM acetic acid and 2 mM EDTA).[143] DNA origami was assembled on the substrate by dripping 2 μL of DNA solution on the substrate and waiting for 40 min before blow away the solution. The substrate was immersed in a 9/1 (v/v) ethanol/water solution to remove the salt from the buffer solution. Right after the deposition of DNA, the substrate was placed in the mass flow etching chamber.

2.3.2.2 Vapor-phase etching procedure.

The etching reaction was carried out inside the custom-built mass flow etching setup shown in Figure 4. Nitrogen gas was flown through concentrated hydrogen fluoride (48%), *iso*-propanol, and water (~ 20 mL each) in three separate bubblers to carry the reagent into the etching chamber and the temperature was controlled by a heating tape outside the chamber. The HF solution was regularly changed after 40 hours of operation to maintain the output partial pressure of HF. We estimate that the concentration of HF solution changes by less than 2% (48% to 46%) under these conditions. The concentration of *iso*-propanol, H_2O and HF was controlled by adjusting the flow rate of N_2 carrier gas and by introducing dry N_2 into the reaction chamber. The silicon wafer containing the DNA triangles was placed at a fixed location on the metal slab inside the chamber. The reaction conditions were systematically varied to study the dependence of reaction kinetics on each parameter. Only 1 wafer was etched at one time. After the reaction, the wafer was washed by acetone and water and heated in an oven at 400℃ to remove DNA and salt residue before AFM and ellipsometry measurements.

2.3.2.3 UV-Ozone Treatment

UV/O_3 treatment was conducted with a Novascan® PSD Pro Series UV-Ozone cleaner. The UV/O_3 chamber was flushed with oxygen for 5 min before UV irradiation.

2.3.2.4 Plasma etching of Si using a SiO_2 hardmask.

Etching of Si was conducted using a Trion Technology Orion III reactive ion etching system. The substrate used in this study was a Si [110] wafer with a thermally-grown 15 nm of oxide layer. After the deposition of DNA template, HF vapor phase etching (p^{HF} = 333 Pa, p^{H2O} = 946 Pa, T = 35 ^{o}C, t = 20 min) and removal of DNA residue, the substrate was subjected to a SF_6/O_2 plasma etch at 25 mTorr of pressure and 100 W RF power with SF_6 (20 sccm) and O_2 (8 sccm) for 5 s. Leftover SiO_2 was removed by immersing the sample in a 5% HF solution for 30 min to expose the underlying Si surface. The substrate was then imaged with AFM.

2.3.2.5 Calculation of partial pressure of each reagent after mixing in the etching chamber.

The reservoir for each chemical was stored at room temperature. The total pressure inside the system was approximately 1 atm. The saturated vapor pressure at 20 ^{o}C of H_2O, *iso*-propanol is 2300 Pa[144] and 4400 Pa[145], respectively. The equilibrium vapor pressure of 48% HF solution is 2666 Pa of HF and 666 Pa of H_2O.[146, 147] We assume that the N_2 gas was in equilibrium with the liquid phase after passing through the bubblers; in the case of water, this assumption was verified to be true by measuring the relative humidity of the etching chamber in the absence of HF and *iso*-propanol vapors by using a Traceable® hygrometer (Control Company, Friendswood, TX). .

The partial pressure of each chemical inside the chamber was proportional to the flow rate of N_2 through its reservoir. As an example, for the following condition: H_2O (30 sccm), N_2

(40 sccm), HF (10 sccm), *iso*-propanol (10 sccm), total flow rate (90 sccm), the partial pressure of each chemical was calculated as:

H_2O: p^{H2O} = 30/90×2300 + 10/90×666 = 841 Pa

HF: p^{HF} = 10/90×2666 = 296 Pa

iso-propanol: p^{IPA} = 10/90×4400 = 489 Pa

Table 1: List of etching condition for the experiments as shown in the figures.

Figure name	Etching condition in flow rate*	Etching condition in partial pressure
6A, 7	H70F10*T*30, *t* = 10 ~ 30 min	p^{HF} = 333 Pa, p^{H2O} =2096 Pa, *T* = 30 ^{o}C, *t* = 10 ~ 30 min
6F (30 ^{o}C), 8	H70F10C10N60*T*30, *t* = 5 ~ 30 min	p^{HF} = 178 Pa, p^{H2O} =1118 Pa, p^{IPA} = 293 Pa, *T* = 30 ^{o}C, *t* = 5 ~ 30 min
6F (35 ^{o}C), 9	H70F10C10N60*T*35, *t* = 5 ~ 25 min	p^{HF} = 178 Pa, p^{H2O} =1118 Pa, p^{IPA} = 293 Pa, *T* = 35 ^{o}C, *t* = 5 ~ 25 min
6B, 6G, 10	H70F10*t*15min, *T* = 30 ~ 45 ^{o}C	p^{HF} = 333 Pa, p^{H2O} =2096 Pa, *t* = 15 min, *T* = 30 ~ 45 ^{o}C
6C, 6H, 11	F10*T*35*t*20min, H = 10 ~70 sccm, H+N = 70 sccm	p^{HF} = 333 Pa, *T* = 35 ^{o}C, *t* = 20 min, p^{H2O} = 83 ~ 2096 Pa
6D, 6I, 12, 13	H70F10*T*30*t*15min, C = 0 ~40 sccm	H70F10*T*30*t*15min, p^{IPA} = 0 ~ 1467 Pa
6E, 6J,	H30N40*T*35, F = 1.4 ~ 20	p^{H2O} =946 Pa, *T* = 35 ^{o}C, p^{HF} =

14	sccm	30 ~ 592 Pa
17A	H35N35F10*T*35*t*20min	p^{HF} = 333 Pa, *T* = 35 °C, *t* = 20 min, p^{H2O} = 1090 Pa
17B	H20N50F10*T*35*t*20min	p^{HF} = 333 Pa, *T* = 35 °C, *t* = 20 min, p^{H2O} = 658 Pa
18C	H35N35F10*T*35*t*20min	p^{HF} = 333 Pa, *T* = 35 °C, *t* = 20 min, p^{H2O} = 1090 Pa
20	H20N50F10*T*35*t*20min	p^{HF} = 333 Pa, *T* = 35 °C, *t* = 20 min, p^{H2O} = 658 Pa
22A	H30N40F10*T*35*t*20min	p^{HF} = 333 Pa, *T* = 35 °C, *t* = 20 min, p^{H2O} = 946 Pa

* The etching condition in flow rate uses abbreviation by the letters representing the reagent or reaction parameter (H for water, N for nitrogen, F for HF, *T* for temperature and *t* for etching duration) and the corresponding experimental values used. For example, H30N40F10*T*35*t*20min represents an etching experiment conducted using 30 sccm of N_2 flowing through the H_2O reservoir, 40 sccm of N_2 flowing directly to the etching chamber, 10 sccm of N_2 flowing through HF, temperature at 35℃ and etching duration of 20 min.

2.4 RESULTS AND DISCUSSION

The overall reaction of the vapor-phase HF etching of SiO_2 is shown as:

$$SiO_2(s) + 4HF(g) \rightarrow SiF_4(g) + 2H_2O(g)$$

Several mechanisms have been proposed for this reaction.[85, 86, 148] It is generally accepted that this reaction is initiated by condensation of HF and water vapors on the SiO_2 surface. Water is both a catalyst and a reaction product which makes the overall reaction autocatalytic.[88] Therefore, the reaction rate will depend on the concentrations of adsorbed water and HF on the surface, both of which are ultimately determined by the vapor pressure of water (p^{H2O}), vapor pressure of HF (p^{HF}), reaction time (t), and the temperature (T) of the sample. In addition to these 4 parameters, we are also interested in the effect of vapor pressure of *iso*-propanol (p^{IPA}). Alcohol additive is known to decrease the surface roughness of SiO_2 in a HF vapor etching reaction and has been extensively used in such reactions; however, its impact on the etching kinetics and quality of pattern transfer has not been studied.[89] Finally, DNA nanostructures are anchored onto SiO_2 via electrostatic interaction mediated by surface adsorbed Mg^{2+}. The presence of Mg^{2+} ion and other ionic species near the DNA may also affect the etching rate either by directly promoting the ionization of HF or indirectly through changing water adsorption.[92]

In this study, we chose the triangular-shaped DNA nanostructure as a model to study the effect of the aforementioned parameters on the pattern transfer. The triangular-shaped DNA nanostructure was used because it does not aggregate and offers several structural features (*e.g.*, linear sides, central void, sharp tips, and presence of a double-strand tail) that are useful in assessing the quality of the pattern transfer.[9]

In a typical experiment, the triangular-shaped DNA nanostructures were deposited onto a silicon wafer that has a 300 nm thick of thermally-grown SiO_2 layer. The silicon wafer with deposited DNA was then etched using a home-built etching setup. In this setup, vapors of HF, H_2O, and *iso*-propanol were supplied by passing N_2 through the respective bubblers. The N_2

streams were then combined and the flow rate of the N_2 carrier gas determines the partial pressure of each reagent. Detailed description of the setup can be found in Figure 4.

In this study, we will focus on reaction conditions that produce the negative-tone pattern transfer, *i.e.*, cases where DNA increases the etching rate. During the vapor phase etching process, the entire SiO_2 surface, regardless of the presence of the DNA nanostructures, was etched (Figure 5). The DNA nanostructure, however, increases the etching rate of SiO_2 near its immediate vicinity. It was hypothesized that the enhancement effect is due to its ability to promote water adsorption near itself.[140] However, direct measurement of a monolayer amount of water on SiO_2 surface with sub-10 nm resolution is extremely challenging, if not impossible. To overcome this challenge, we extract the magnitude and the spatial extent of the enhancement effect of DNA from the vertical contrast and lateral resolution of the resulting pattern, respectively. The width of the trench was typically measured at the center of the sides. The depth measurement, however, could be limited by the narrow width and may not reflect of the true topography (see below). For this reason, we perform depth measurement at the apexes of the triangle instead.

Two sets of data are especially relevant to understanding the kinetic behavior of the etching reaction. As shown in Figure 5, the first is the thickness (d_{pristine}) of SiO_2 removed in the absence of DNA and the corresponding average etching rate ($v_{prstine}$). The second is the thickness of SiO_2 removed and the corresponding average etching rate in the presence of DNA (d_{DNA} and v_{DNA}). We note that the etching rate of SiO_2 is likely to be time dependent due to the autocatalytic nature of the reaction. In our experiments, we used ellipsometry and atomic force microscope (AFM) to measure the average thickness of SiO_2 and the depth of the trench, respectively. The surface coverage of the trenches is usually < 8% and therefore the change of

the SiO_2 thickness reported by ellipsometry should reflect $d_{pristine}$. The depth of the trench reflects the difference between $d_{pristine}$ and d_{DNA}.

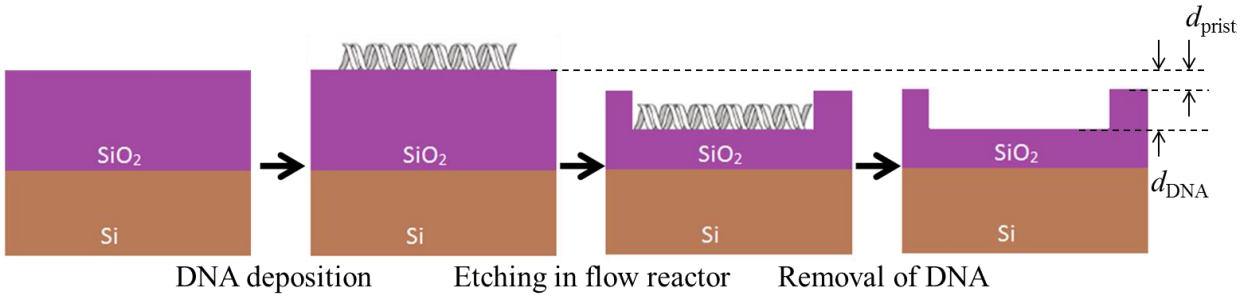

Figure 5. Geometry change during the DNA-mediated HF etching of SiO_2.

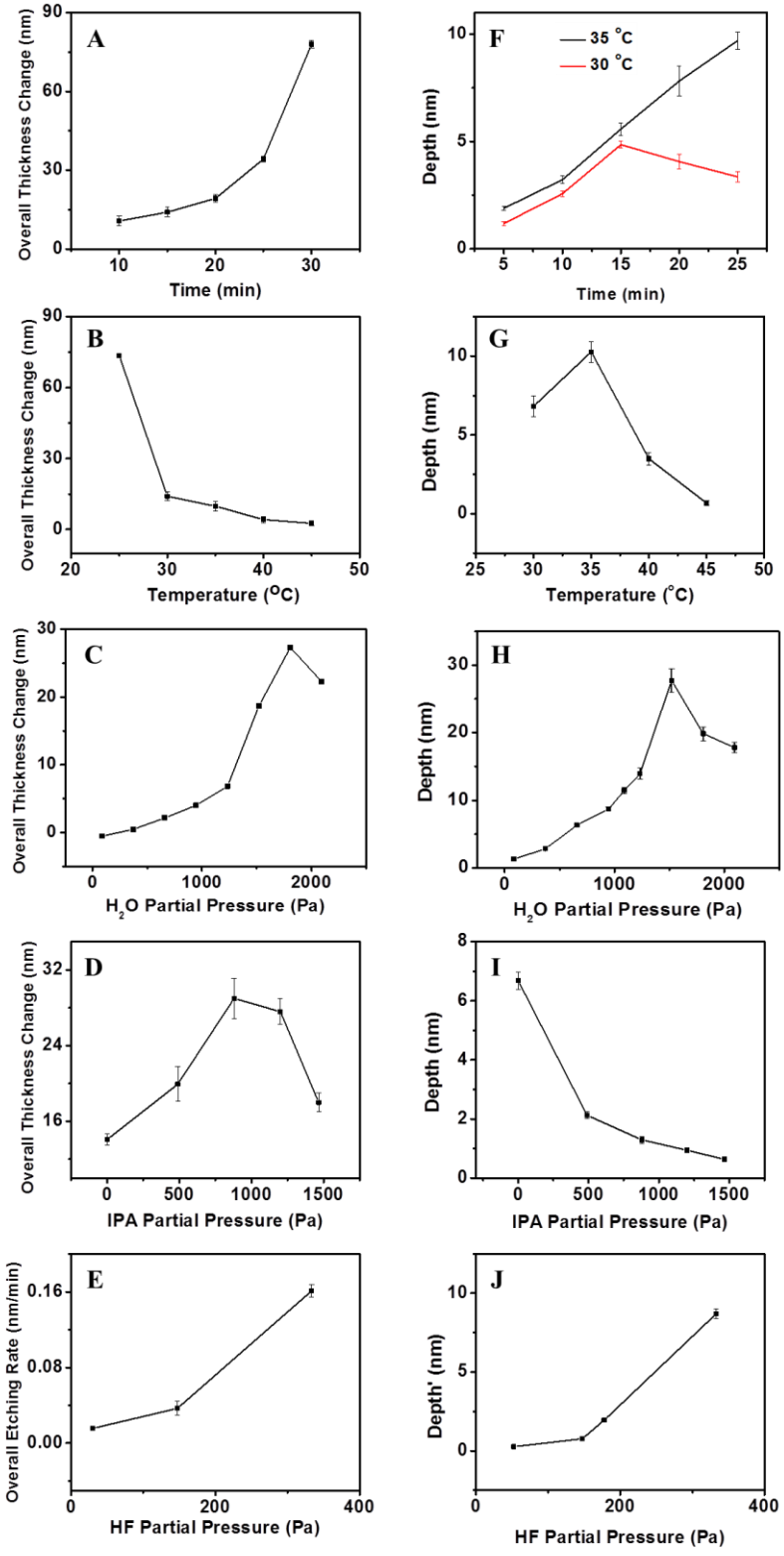

Figure 6. Kinetics of vapor phase HF etching of SiO_2. (A) p^{HF} = 333 Pa, p^{H2O} =2096 Pa, T = 30 °C, t varied from 10 to 30 min; (B) and (G) p^{HF} = 333 Pa, p^{H2O} =2096 Pa, t = 15 min, T varied from 25 to 45 ℃; (C) and (H) p^{HF} = 333 Pa, T = 35 °C, t = 20 min, p^{H2O} varied from 83 to 2096 Pa, (D) and (I) p^{IPA} varied from 0 to 1467 Pa, see SI for details; (E) and (J) p^{H2O} = 946 Pa, T = 35 °C, p^{HF} varied from 30 to 333 Pa. The etching time was adjusted to obtain comparable contrast in AFM image. The depth shown here is the expected value for the same etching duration (20 min), assuming the etching rate is time independent. See SI for details; (F) p^{HF} = 178 Pa, p^{H2O} =1118 Pa, p^{IPA} = 293 Pa, t varied from 5 to 25 min.

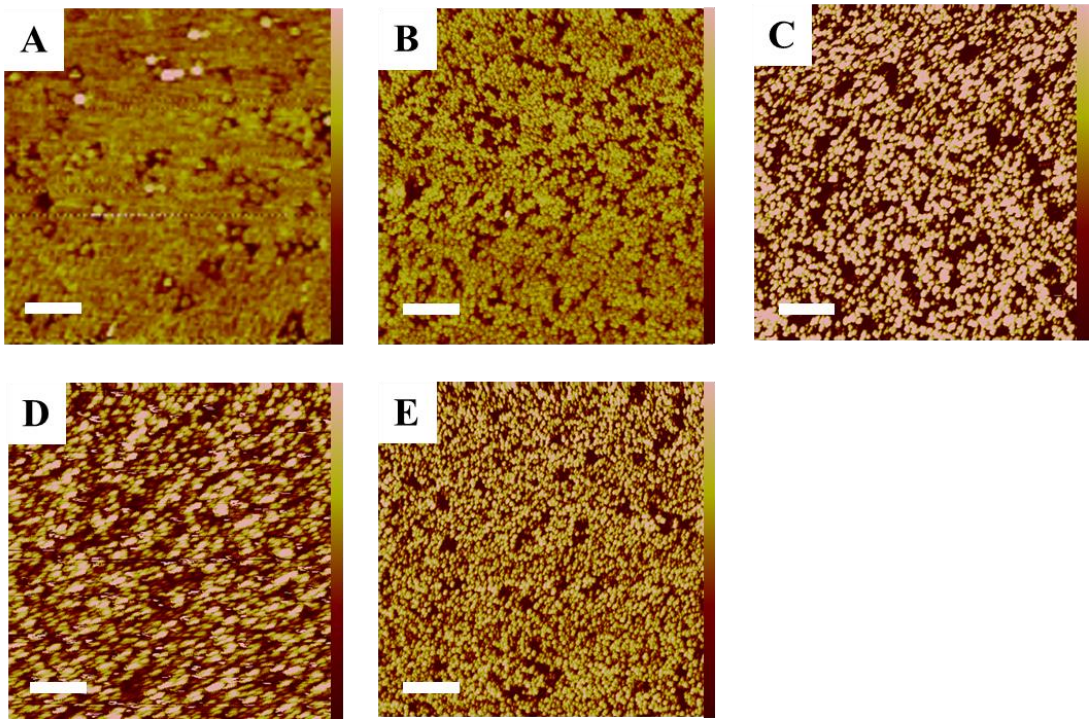

Figure 7. Effect of reaction time on the pattern transfer. p^{HF} = 333 Pa, p^{H2O} =2096 Pa, T = 30 ^{o}C; from A to E, t was 10, 15, 20, 25, and 30 min respectively. Color scale bar represents 5 nm in A - C and 10 nm in D and E. Scale bar represents 250 nm in A and 500 nm in B-E.

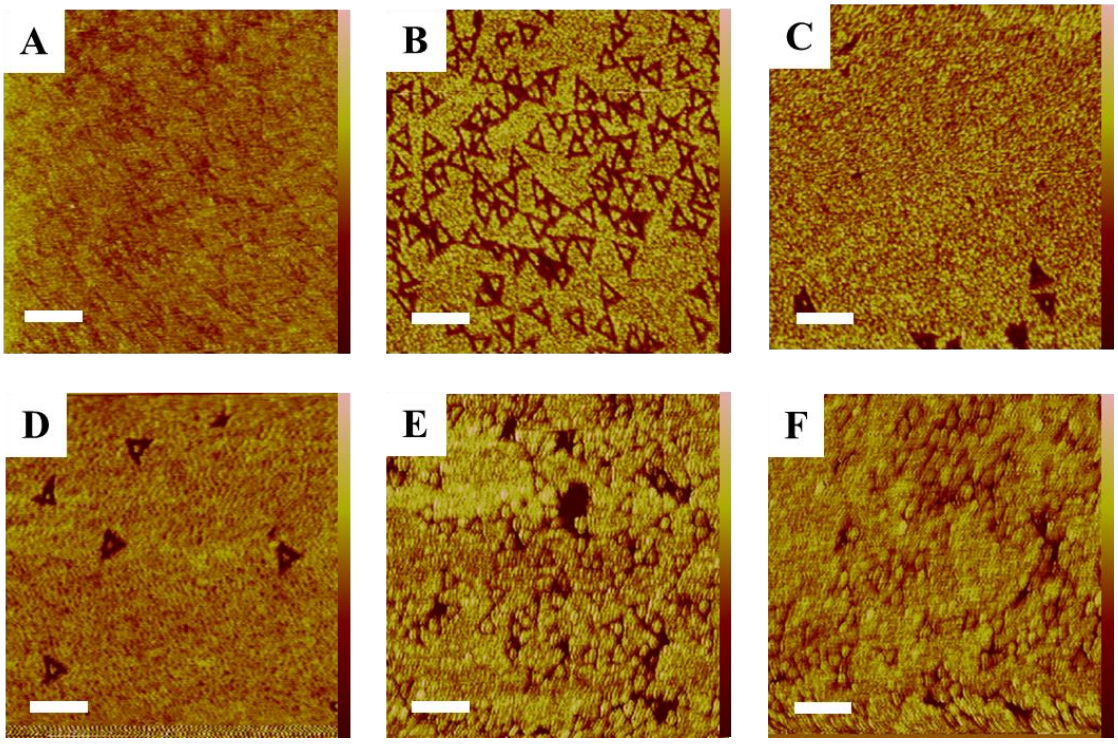

Figure 8. Effect of reaction time on the pattern transfer. p^{HF} = 178 Pa, p^{H2O} =1118 Pa, p^{IPA} =293 Pa, T = 30 ^{o}C; from A to F, t was 5, 10, 15, 20, 25, and 30 min respectively. Color scale bar represents 5 nm. Scale bar represents 250 nm.

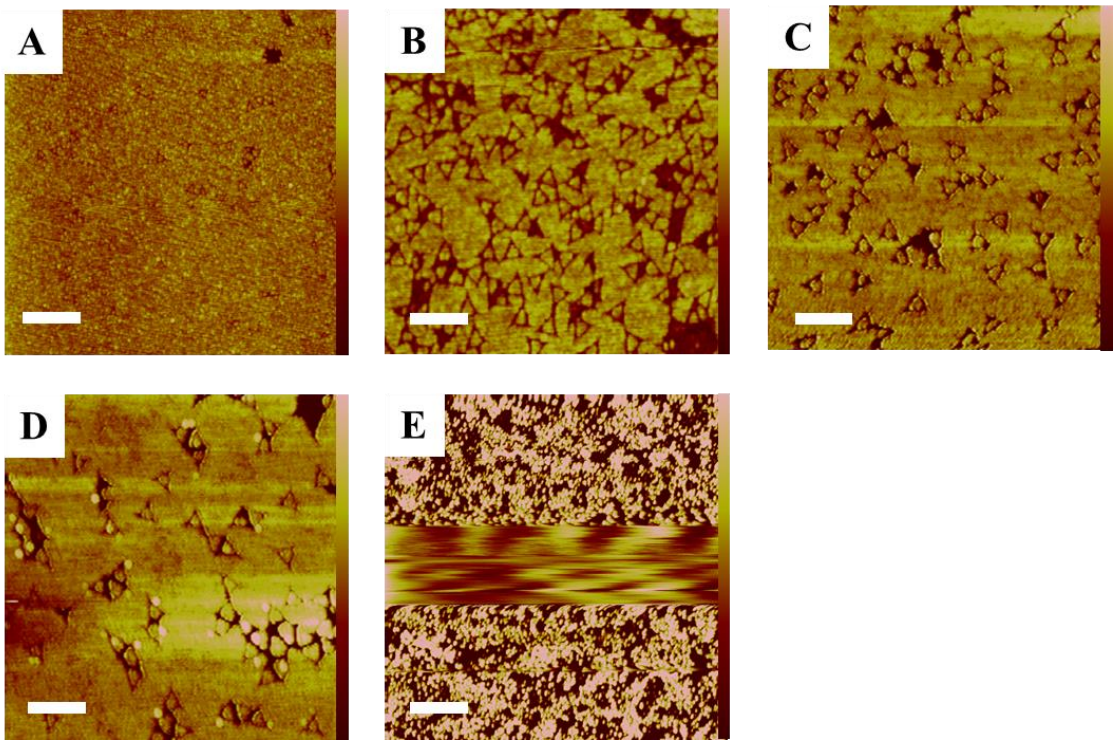

Figure 9. Effect of reaction time on the pattern transfer. p^{HF} = 178 Pa, p^{H2O} =1118 Pa, p^{IPA} =293 Pa, T = 35 ^{o}C; from A to E, t was 5, 10, 15, 20, 25 min respectively. Color scale bar represents 5 nm in A and B, 10 nm in C, D and E. Scale bar represents 500 nm in A and E and 250 nm in B - D.

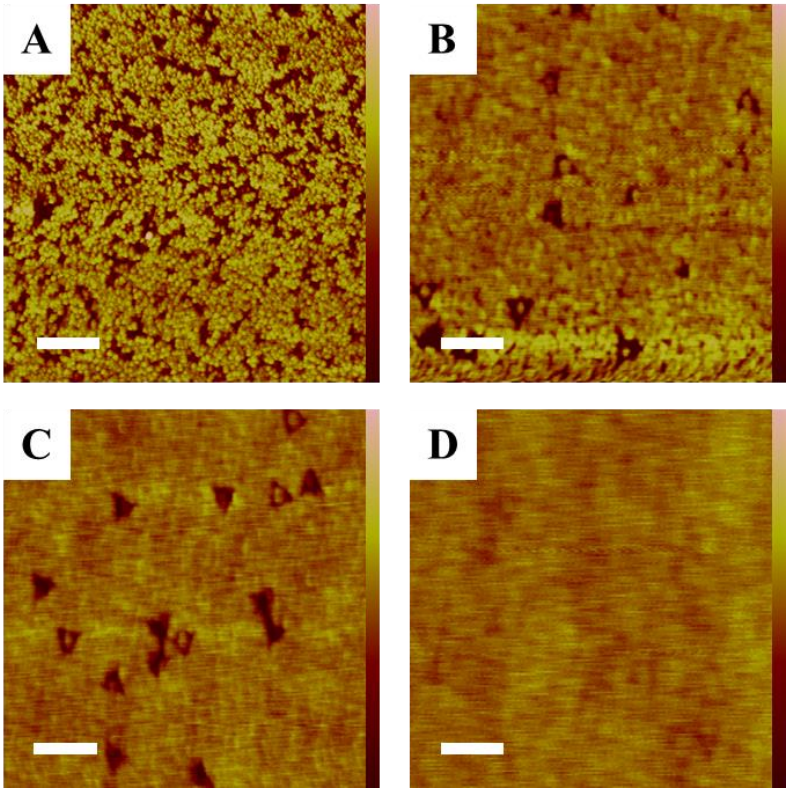

Figure 10. Effect of reaction temperature on the pattern transfer. p^{HF} = 333 Pa, p^{H2O} =2096 Pa, *t* = 15 min; from A to D, *T* was 30, 35, 40 and 45 ^{o}C respectively. Height scale bar represents 10 nm in A and B; 5 nm in C and D. Scale bar represents 500 nm in A; 250 nm in B - D.

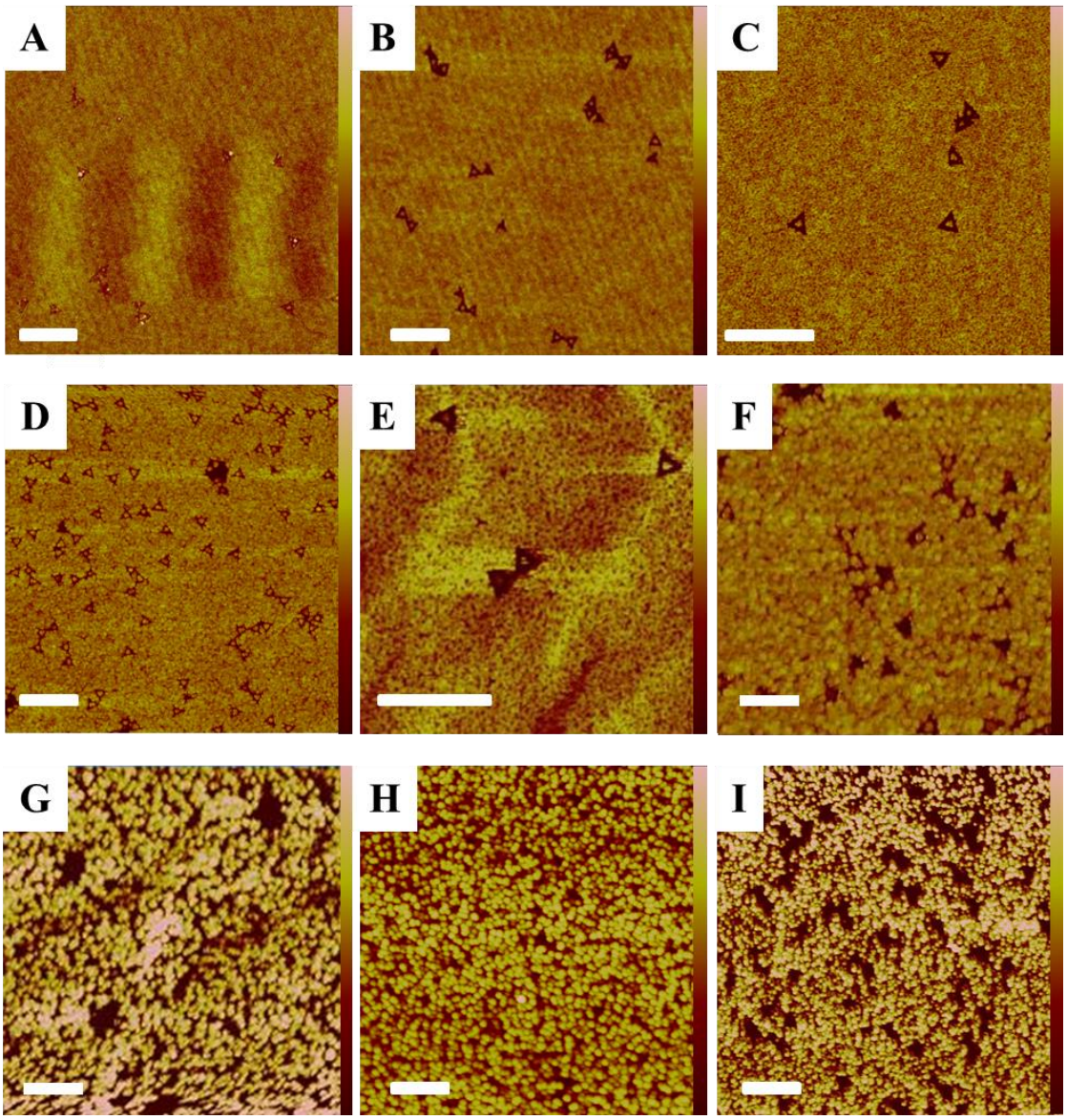

Figure 11. Effect of partial pressure of water on the pattern transfer. p^{HF} = 333 Pa, T = 35 ^{o}C, t = 20 min; from A to I, the partial pressure of water was 83, 371, 658, 946, 1090, 1233, 1521, 1808, 2096 Pa respectively. The scale bars in all the images represent 500 nm. The height scale bar represents 5 nm in figure A, B, C, E and G; 10 nm in figure D, F and I; 20 nm in figure H.

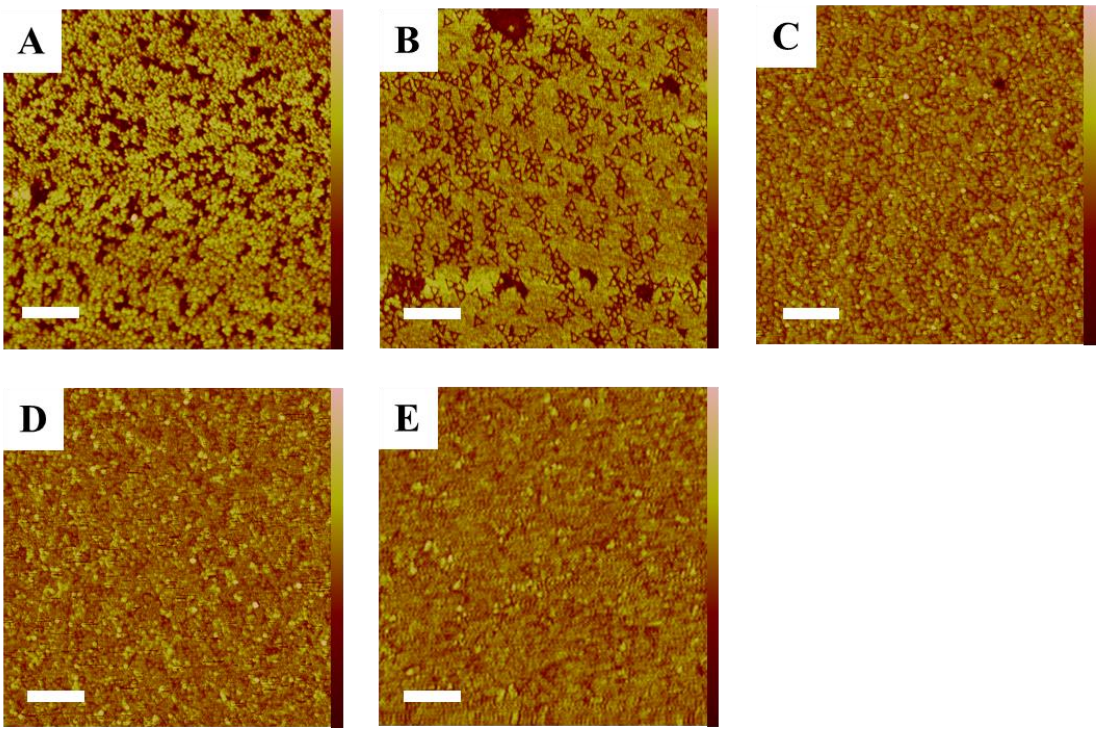

Figure 12. Effect of vapor pressure of *iso*-propanol on the pattern transfer. Under condition: H70F10T30t15min; from A to E, the partial pressure of *iso*-propanol was 0, 489, 880, 1200 and 1467 Pa respectively. The scale bars in all the images represent 500 nm. The height scale bar represents 10 nm in A and 5 nm in figure B - D.

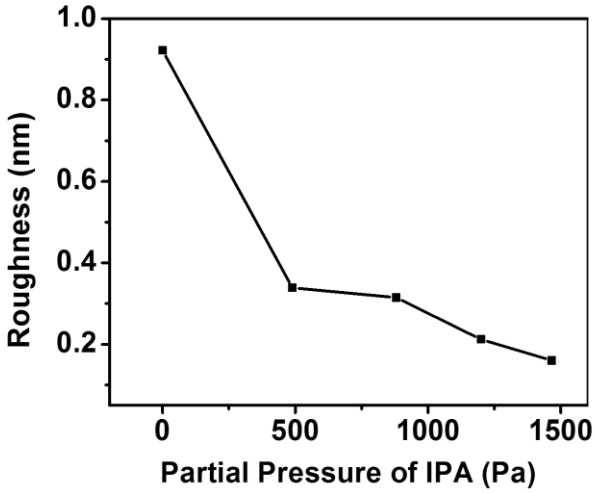

Figure 13. Surface roughness in control experiments under condition H70F10T30t15min; from A to E, the partial pressure of *iso*-propanol was 0, 489, 880, 1200 and 1467 Pa respectively.

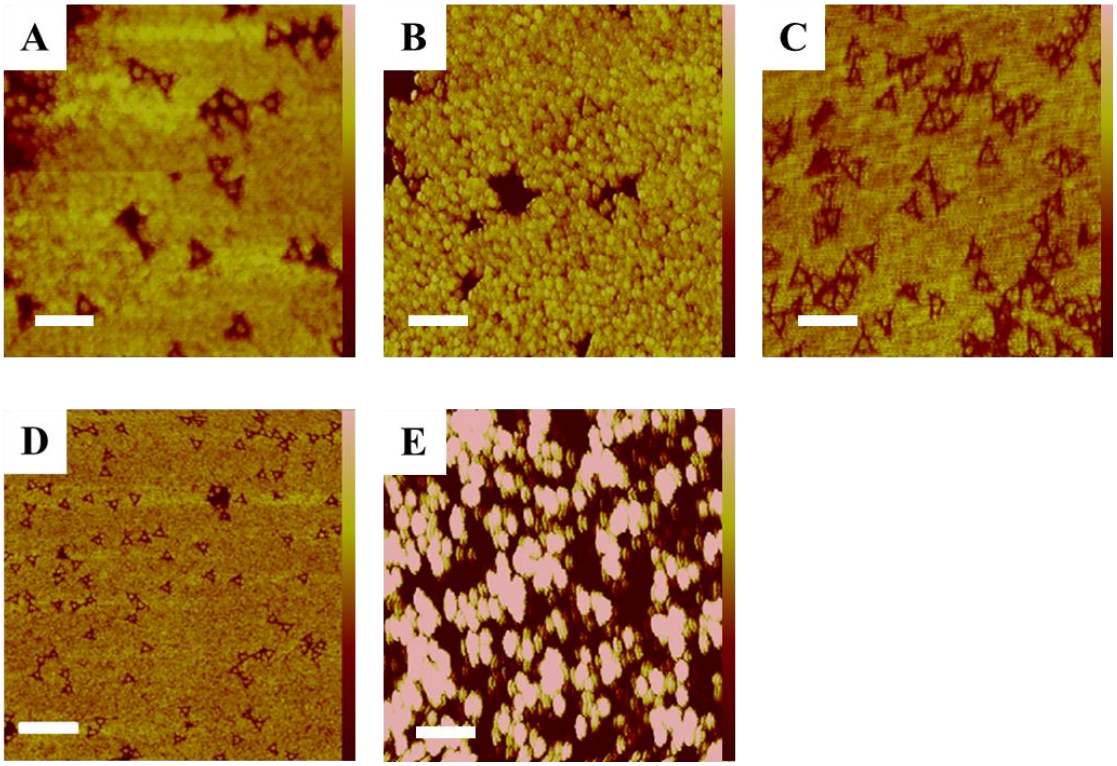

Figure 14. Effect of vapor pressure of HF on the pattern transfer under p^{H2O} = 946 Pa, T = 35 ^{o}C, t = 20 min; from A to I, the partial pressure of HF was 52 Pa (8 hours etching), 147 Pa (200 min etching), 178 Pa (20 min etching), 333 Pa (20 min etching) and 592 Pa (15 min etching) respectively. The scale bar represents 250 nm (A – C and E) or 500 nm (D). The color scale bar represents 10 nm in A, B, and D and 5 nm in C and E.

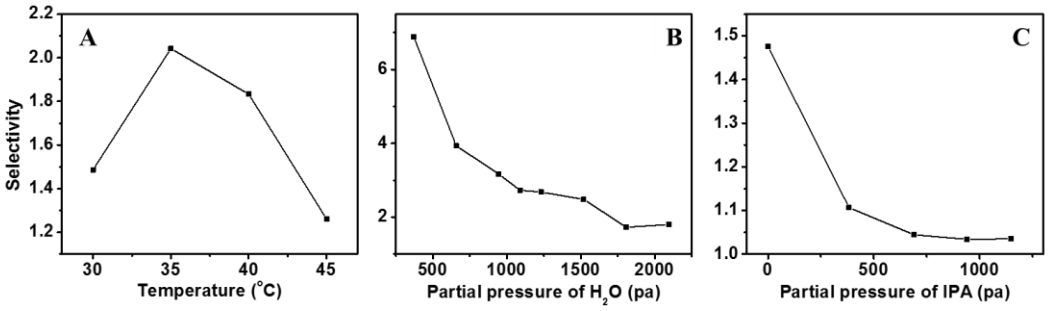

Figure 15. HF etching selectivity in control experiments: (A) p^{HF} = 333 Pa, p^{H2O} =2096 Pa, t = 15 min, T varied from 30 to 45 ℃; (B) p^{HF} = 333 Pa, T = 35 °C, t = 20 min, p^{H2O} varied from 371 to 2096 Pa, (C) p^{IPA} varied from 0 to 1467 Pa.

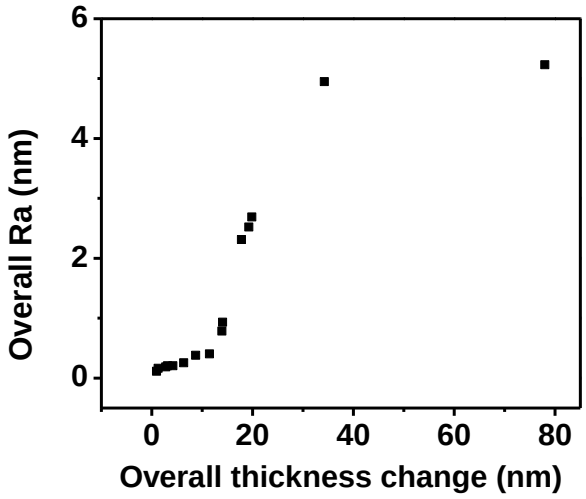

Figure 16. Correlation between surface roughness (Ra) and overall thickness change of SiO_2. Data was based on the Figure 7 - 11.

2.4.1 Kinetics Behavior of the DNA-mediated HF Etching of SiO_2.

2.4.1.1 Effect of reaction time.

Figure 6A shows the overall thickness change of SiO_2 layer (*i.e.*, d_{pristine}) as a function of reaction time while keeping all other parameters fixed (p^{HF} = 333 Pa, p^{H2O} = 2096 Pa, T = 30 ^{o}C). The related AFM images are shown in Figure 7. The thickness change shows a super-linear increase over time. This is consistent with the hypothesis that the etching reaction is autocatalytic: as the reaction progresses, more water is produced and the reaction rate will increase until the formation and desorption of water reaches equilibrium. At long reaction times, we also noticed an increase of surface roughness (Figure 7) and a significant deterioration of the quality of the transferred pattern.

The trench depth showed a more complex time dependence. Figure 6F showed the time evolution of the trench depth for two reactions conducted at T = 35 °C and 30 °C, respectively; in both series, all other reaction conditions were fixed (p^{HF} = 178 Pa, p^{H2O} = 1118 Pa, p^{IPA} = 293 Pa). The corresponding AFM images are shown in Figure 8, 9. Although the difference in the reaction temperature was only 5°C, the two reactions showed very different behavior: at 35 °C, we observed a continuous, almost linear increase in the trench depth, indicating that the difference in the two etching rates (*i.e.*, $v_{prstine}$ and v_{DNA}) is a constant during this reaction. In contrast, the reaction conducted at 30 ^{o}C showed an initial increase in the trench depth that peaked at 15 min, followed by an eventual decrease.

These results can be explained if we assume that enough water was produced at t = 15 min at T = 30 °C to saturate the entire surface. At even longer etching time, the etching becomes non-selective as DNA cannot further enhance water adsorption. At 35°C, it takes longer to saturated the surface with water due to the faster desorption of water; as a result, the etching

remains selective and the trench depth showed a more persistent increase. However, even at 35°C, the surface roughness still increased significantly after 20 min of reaction and the quality of the pattern transfer deteriorated as a result. The optimal etching time is 15 or 20 min under these conditions.

2.4.1.2 Effect of reaction temperature.

To study the effect of temperature on the pattern transfer, we conducted the etching experiment between 25°C to 45°C while kept all other parameters fixed (p^{HF} = 333 Pa, p^{H2O} = 2096 Pa, t = 15 min). Figure 6B shows the change of SiO_2 thickness measured by ellipsometry (*i.e.*, $\Delta d_{\text{pristine}}$) as a function of substrate temperature. It can be seen that $v_{prestine}$ decreased drastically as the temperature was increased. This observation is consistent with the idea that the adsorption of water and/or HF is inhibited at high temperature and therefore the etching rate decreases as temperature increases.

Interestingly, the depth of the trench showed a very different response to temperature change. As shown in Figure 6G and 10, when the reaction temperature was increased from 30°C to 45°C, the trench depth initially increased and then decreased. To understand this observation, we again note that water is a reaction product and if not removed by desorption, will eventually saturate the surface. If the temperature is too low, the water produced by the etching reaction will quickly saturate the entire surface, regardless of the presence of DNA. As a result, the DNA will not selectively increase the etching rate. The opposite situation will occur if the temperature is too high, in which case, water desorbs from the entire surface, regardless of the presence of DNA. The effect of DNA to modulate water adsorption will be most pronounced in the intermediate temperature range.

2.4.1.3 Effect of partial pressure of water.

The effect of p^{H2O} was studied by adjusting the flow rate of wet and dry N_2 while keeping the overall flow rate constant. We assumed that the N_2 is fully saturated with water after passing through the water bubbler and also took into account of the water vapor from the HF/H_2O reservoir to calculate p^{H2O} in the etching chamber.

Figure 6C shows the change of SiO_2 thickness when p^{H2O} was varied from 83 to 2096 Pa while keeping all other parameters fixed (p^{HF} = 333 Pa, T = 35 ^{o}C, t = 20 min). It is clear that increasing p^{H2O} resulted in an increase of $v_{prstine}$, presumably due to an increase of the adsorption of H_2O. There is slight decrease in the etching rate at very high p^{H2O} that we attributed to the dilution of adsorbed HF on the surface. Figure 6H shows that the trench depth increased drastically as p^{H2O} increased, indicating that at higher humidity, the H_2O absorption is favored near the DNA. The small decrease at very high p^{H2O} may be due to water saturation on the entire surface, as we discussed previously. Overall, data in Figure 6H is consistent with the fact that water adsorption on DNA is much more sensitive to the increase of relative humidity than that on SiO_2: the amount of absorbed water on SiO_2 increases only by 40% when the relative humidity increases from 0 to 85%.[90] In contrast, DNA shows an increase of 2800% in water adsorption when the relative humidity increases from 0 to 98%.[91]

AFM imaging showed that the quality of the transferred patterns was high (*e.g.*, narrow outlines with preserved central island feature) when p^{H2O} was below 1090 Pa (Figure 11 A to E). However, at higher p^{H2O}, the central island features were not preserved and instead became triangular shaped holes (Figure 11 F to I). These observations suggest that as water saturates the DNA, the etching reaction lost its spatial selectivity. In addition, the surface roughness also worsened at high p^{H2O}, due to the high overall etching rate (also see below). For these reasons, a

low p^{H2O} (*ca.* 946 Pa) provides the best balance between the contrast and the quality of the pattern transfer.

2.4.1.4 Effect of partial pressure of *iso*-propanol.

A smooth surface is essential to obtain high quality and faithful pattern transfer. For this reason, we previously introduced alcohol vapor to the etching reaction because it is known to reduce the surface roughness of the HF vapor phase etching.[140] However, its effect on the kinetics and selectivity of the DNA-mediated etching has not been reported. Here we investigate the effect of *iso*-propanol on the surface roughness and etching kinetics.

In this set of experiments, we fixed the flow rates of HF and H_2O carrier gases and adjusted the flow rate of *iso*-propanol carrier gas to change p^{IPA}. With increasing p^{IPA}, the overall SiO_2 thickness change initially increased and then decreased (Figure 6D). It was proposed by Novak and coworkers that at low p^{IPA}, an *iso*-propanol monolayer was formed on SiO_2; this monolayer could trap water and lead to an increase of the etching rate at low p^{IPA}.[149] It is not clear what caused the decrease of etching rate at high p^{IPA}. One possibility is that *iso*-propanol and water could form a low boiling point azeotrope mixture (*b.p.* 80.79 ^{o}C) on the surface, facilitating the desorption of water.[150] We also note that this behavior is similar to that observed under high p^{H2O}, suggesting the dilution of adsorbed HF may be another contributing factor.

Figure 6I shows the depth of trench for the same set of experiment. We find that the introduction of *iso*-propanol reduced depth of trench, indicating that it reduces the selectivity of the SiO_2 etching between pristine and DNA-covered SiO_2 (Figure 12). Although the roughness indeed decreased at high p^{IPA} (Figure 13), this benefit does not justify its use in our reaction.

2.4.1.5 Effect of partial pressure of HF.

Figure 6E shows the average etching rate of SiO_2 in the absence of DNA as a function of p^{HF}. A monotonic increase in the etching rate was observed. This behavior is expected since increasing the partial pressure HF (p^{HF}) should increases the adsorption of HF and thereby increasing the SiO_2 etch rate. When all other conditions were fixed (p^{H2O} = 946 Pa, T = 35 ^{o}C), increasing p^{HF} (Figure 6J, 14) resulted in an increase of the trench depth, which indicates that the etching selectivity ($v_{DNA}/v_{prstine}$) also increased with increasing p^{HF}. However, very high p^{HF} is not desirable because the surface roughness increases significantly under these conditions (Figure 14 and also see below).

2.4.1.6 Effect of temperature, partial pressure of water and *iso*-propanol on the etching selectivity

Effect of temperature, partial pressure of water and *iso*-propanol on the etching selectivity, which is defined as $v_{DNA}/ v_{pristine}$, was investigated to study the tendency of water absorption to different parts of the substance, as well as to understand the etching mechanism. Figure 15A and 15C show the change of etching selectivity as a function of temperature and p^{IPA}, respectively. In both cases, the change in selectivity resembles that of the trench depth as we discussed in the main text (Figure 6G, 6I). This observation is consistent with our hypothesis that adsorbed water modulates the local HF etching rate. Interestingly, when p^{H2O} was increased from 371 to 2096 Pa, the selectivity continuously decreased (Figure 15B) whereas the trench depth reached a peak value at 1521 Pa (Figure 6H). The decrease of selectivity is expected because at high humidity level, one expects the entire surface to be saturated by water and therefore non-selective etching. Please note that the trench depth and etching selectivity are not expected to follow the same trend

because the former is the difference between v_{DNA} and $v_{pristine}$ and the latter is the ratio of the two rates.

2.4.1.7 Correlation between overall etching thickness and roughness.

In Figure 16, we plot the surface roughness as a function of the overall thickness change ($d_{pristine}$) for the experiments shown in Figure 7 – 11. Although these experiments were done under very different conditions, a consistent trend is that larger thickness change is correlated with larger surface roughness. Since the quality of transferred pattern will be negatively impacted by large surface roughness, optimized condition should produce a small $d_{pristine}$.

2.4.2 Optimized Pattern Transfer Conditions.

Our kinetics studies suggest the following design rules for achieving high quality pattern transfers: (1) intermediate reaction time is preferred. At short reaction time, the contrast is not fully developed; however, long reaction time may lead to non-selective etching due to the saturation of water on the entire surface; (2) intermediate reaction temperature is preferred. Very low reaction temperature results in fast etching even in the absence of DNA; too high a temperature is detrimental because water adsorption is inhibited regardless of the presence of DNA; (3) intermediate water and HF partial pressures are preferred. Increase partial pressure of water and HF results in an increase of the overall etching rate and contrast of the transferred pattern. However, surface roughness also increases at high etching rate and the pattern transfer deteriorates as a result; and (4) *iso*-propanol is not desirable, as its presence will generally decrease etching selectivity.

Based on these results, we identified two conditions for high resolution, high contrast pattern transfer: condition A: p^{HF} = 333 Pa, p^{H2O} =1090 Pa, T = 35 ^{o}C, t = 20 min, and condition B: p^{HF} = 333 Pa, p^{H2O} =658 Pa, T = 35 ^{o}C, t = 20 min. Under condition A, the triangular trenches obtained on SiO_2 were 11.8 ± 0.3 nm in depth (measured at the apexes of the triangle) and the full width at half maximum (FWHM) of the edges was 14 ± 1 nm (Figure 17A). Compared to our previous work, the present study improved the trench depth by almost 5 times. The surface roughness was 0.404 nm, which is only 3.5% of the depth of the trench. The overall thickness change of the SiO_2 layer was 6.82 ± 0.32 nm, which translates to an etching selectivity (v_{DNA}/ $v_{prstine}$) of 2.73. These results could be reproduced on both 300 nm SiO_2 grown on Si [100] wafer and 15 nm SiO_2 grown Si [110] wafer in a period of 2 months. Under condition B, even higher resolution can be obtained at the expense of reduced contrast. The FWHM of the trenches was reduced to 11 ± 1 nm while the depth was 6.0 ± 1.5 nm (both measured on the sides of the triangle). Figure 17B inset shows a pattern that is 7.8 nm in width (FWHM), which is smaller than that of the DNA template (28.6 nm). Although we do not know the detailed reason behind this observation, we speculate that the center of the origami arm is more effective in catalyzing the etching reaction, likely because water is least likely to desorb from these locations. However, we also note that the tip deconvolution effect will make the trenches appears narrower and additional work is needed to quantify this contribution.

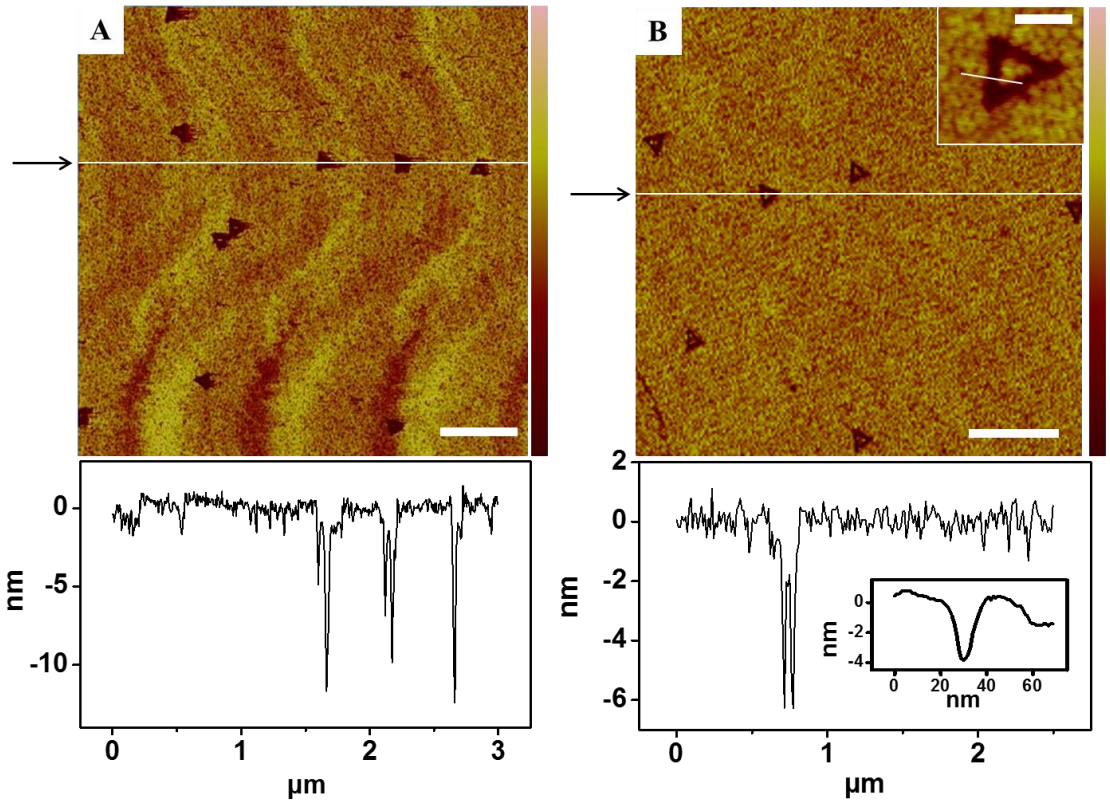

Figure 17. AFM images and cross sections the deepest (A) and narrowest (B) trenches of the triangular patterns produced by the optimized pattern transfer conditions A and B respectively. The white line in the upper inset of B indicates the location of cross section shown in the bottom inset. The wavy lines with *ca.* 1 μm periodicity in A were artifacts. The color scale bars represent 10 nm in both images. The white scale bars represent 500 nm, and the scale bar in the inset represents 100 nm.

2.4.3 Mechanistic studies and lithography enabled by the optimized pattern transfer condition.

Compared to our previous results,[140] the new pattern transfer condition offers up to 5 fold increase in the depth and 50% reduction in the width of the trench. These improvements make it

possible to answer additional mechanistic questions and also enable further patterning approaches, as detailed below.

2.4.3.1 Role of salt residue in the etching reaction.

DNA has both organic (*i.e.,* bases, sugar) and inorganic components (*i.e.*, phosphate backbone and counter ions) and each may play a different role in the pattern transfer. To decompose their effect, we have investigated the effect of inorganic salt on the HF etching reaction. In addition to the phosphate backbone and counter ion, a deposited DNA nanostructure may also accumulate salt from the buffer solution, either through selective adsorption or as a result of the solvent evaporation. For example, it is known that Mg^{2+} ions adsorb on the SiO_2 surface and play a critical role in anchoring the DNA nanostructure onto the surface.[15] The salt residues could impact the etching rate either by directly promoting the ionization of HF or indirectly through changing the thermodynamics of water adsorption.

To remove all organic components from the DNA, we performed UV/Ozone treatment on DNA samples deposited on SiO_2. UV/Ozone treatment is a well-established method to oxidatively remove organic species on a surface.[151] The SiO_2 surface was characterized by AFM before and after the treatment and the data is shown in Figure 18. Surprisingly, we found that the triangular patterns persisted even after 3 hr of UV/Ozone treatment, although their height did show a significant decrease from 1.59 ± 0.19 nm to 0.93 ± 0.26 nm. X-ray photoelectron spectroscopy (XPS) confirmed the elimination of nitrogen in DNA and the preservation of Mg^{2+} on the surface (Figure 19). The absence of nitrogen suggests that the organic components were completely removed and therefore, we attribute the triangular pattern to the inorganic salt residues associated with DNA nanostructures (Figure 18B).

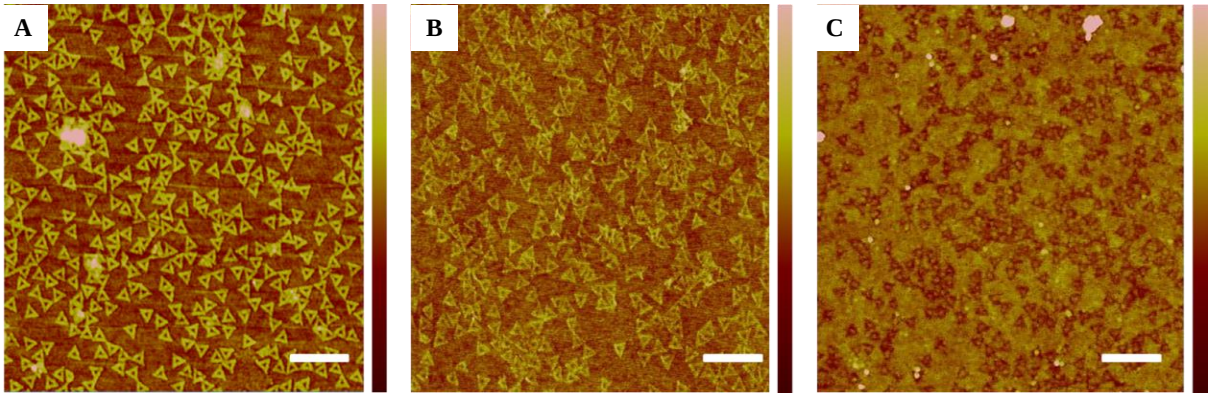

Figure 18. AFM images of (A) DNA nanostructures on the SiO_2 substrate; (B) salt residue on surface after 3 hr UV/Ozone treatment; and (C) triangular trench produced by HF vapor etching (p^{HF} = 333 Pa, p^{H2O} =1090 Pa, T = 35 ^{o}C, t = 20 min). Height bars represent 5 nm. Scale bars represent 500 nm.

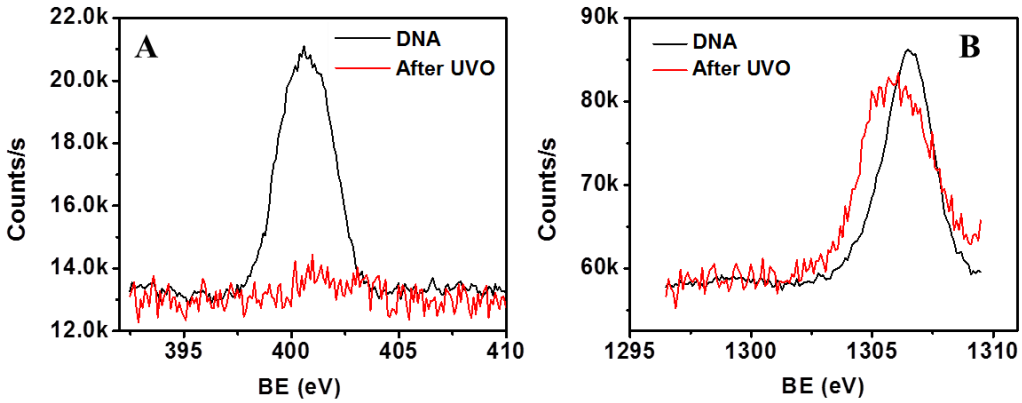

Figure 19. XPS spectra of fresh and the UV/Ozone (UVO) treated DNA samples at (A) N1s peak, ~399 eV and (B) Mg1s peak, ~1307 eV. The peak intensity was referenced to the Si peak from the underneath SiO_2 substrate.

We found that the inorganic residue can produce shallow trenches (0.94 ± 0.29 nm, measured at the apexes of the triangle) when subject to the HF vapor phase etching (p^{HF} = 333 Pa, p^{H2O} =1090 Pa, T = 35 ^{o}C, t = 20 min, Figure 18C). Although we do not know the mechanistic details, it is clear that the salt could enhance the HF-vapor etching of SiO_2. However, the depth of the trench is significantly smaller than the ones obtained under the same condition using the DNA nanostructure template (11.8 ± 0.3 nm, measured at the apexes of the triangle), suggesting that the organic component of DNA plays a major role in the enhanced etching.

2.4.3.2 Pattern transfer from individual DNA strands.

One intriguing question of the DNA-mediate HF etching is its resolution limit and in particular, whether the pattern transfer can be achieved with a single DNA strand. We previously showed that λ-DNA, when stretched and deposited on to a SiO_2, can enhance the HF etching rate to produce trenches.[140] However, the presence of DNA bundles makes it difficult to definitively conclude if the resulting patterns were from an individual double-stranded DNA.

In this study, we observed that many triangular-shaped trenches were accompanied by a

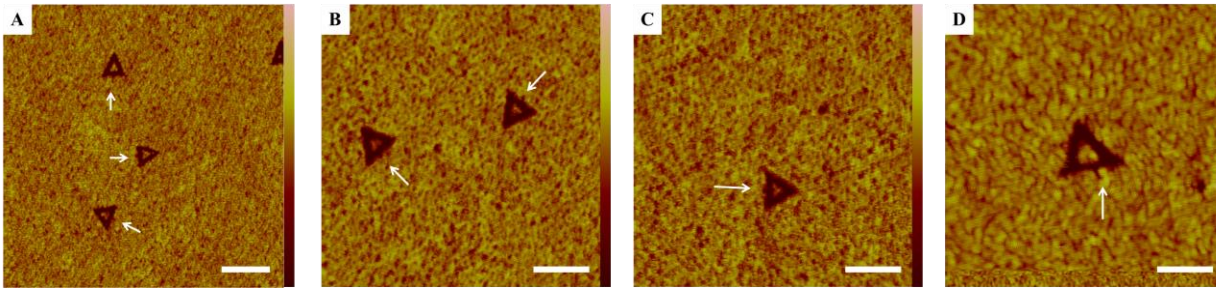

Figure 20. High magnification AFM images of etching results to show the presence of a tail, as indicated by the arrow. The height bar represents 5 nm in A – D. The scale bar represents 250 nm in A - C and 100 nm in D.

small tail (2.0 ± 0.4 nm in depth and 7 ± 1 nm in width), located in the middle of one of the sides (Figure 20). We believe that this tail is produced by the 97-base loop of the DNA nanostructure (Figure 3A); secondary structure analysis suggests that this loop likely exists in a linear structure (Figure 3B).[93] This result clearly indicates that even a single double-stranded DNA is capable of enhancing the local etching rate of SiO_2.

2.4.3.3 Pattern transfer on Si surface using plasma etching.

The newly developed pattern transfer conditions offer much higher contrast, and therefore the possibility to etch-through a thin (*c.a.*, 10 nm) SiO_2 film. The SiO_2 pattern thus produced could then be used as a hard mask for patterning the underneath substrate, such as Si. To demonstrate this possibility, we used a silicon wafer with 15 nm of thermal oxide to carry out the DNA-mediated HF etching. After the vapor-HF etching and removal of DNA templates using UV/O_3, AFM imaging showed that the trenches have a depth (measured at the apexes of the triangle) of 6.8 ± 0.5 nm, and a width (measured at the sides of the triangle) of 12 ± 2 nm (Figure 21A and 22). The wafer was then subjected to a SF_6/O_2 plasma that preferential etches Si (etching selectivity Si : SiO_2 = 50 : 1).[152] After the plasma etching, the depth of the trench (measured at the apexes of the triangle) increased from 6.8 ± 0.5 nm to 10.3 ± 2.1 nm (Figure 21B and 22); the surface roughness also increased by almost 4 times from 0.20 ± 0.01 nm to 0.76 ± 0.05 nm. We then selectively removed the top SiO_2 layer by etching with a solution of 5% HF and observed triangular trenches on the underlying Si substrate. As shown in Figure 21C and 22, the depth of the trenches increased to 18.4 ± 2.7 nm (measured at the apexes of the triangle), while the FWHM is 19 ± 4 nm (measured at the sides of the triangle). The surface roughness was 0.27 ± 0.01 nm. It is interesting to note that the depth of the trench increases after removing the top SiO_2 layer. Noting that the width of the trench also increased after removing SiO_2, we believe that the

depth measurement before removing SiO_2 was limited by the narrow trench (*i.e.*, the AFM tip is unable to probe the bottom of the trench) and did not reflect the true geometry of the trench.

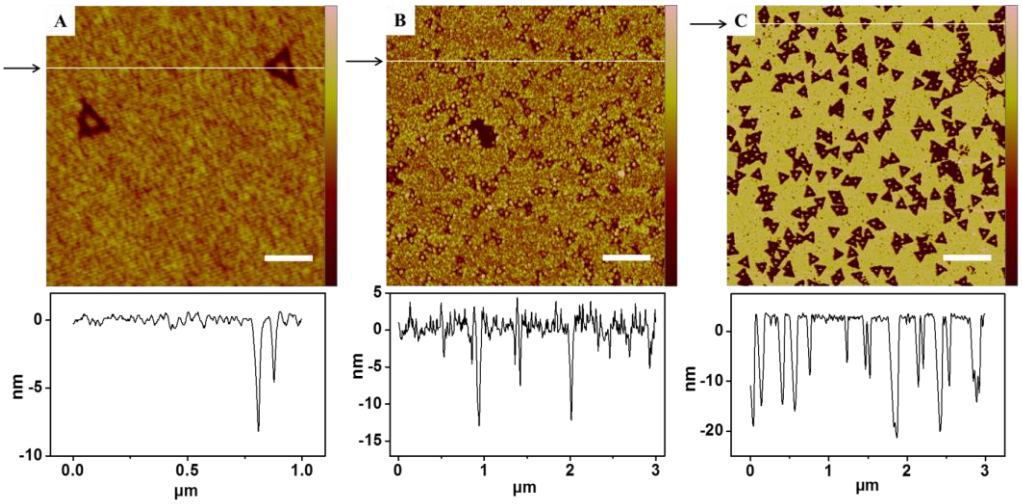

Figure 21. AFM images and cross sections of (A) triangular trenches produced by HF etching (p^{HF} = 333 Pa, p^{H2O} =946 Pa, T = 35 ^{o}C, t = 20 min); (B) the same sample after subjected to SF_6/O_2 plasma etching for 5 s; and (C) triangular patterns on the same sample after removal of top SiO_2 film by emersion in 5% HF solution for 30 min. Arrows indicate lines of cross section. The color scale bar represents 5 nm in A and 10 nm in B and C. Scale bar represents 200 nm in A and 500 nm in B and C.

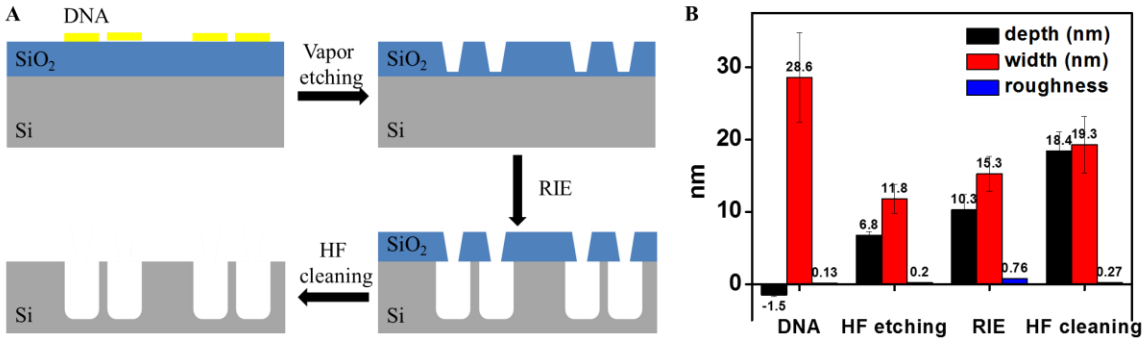

Figure 22. Cartoon sketch (A) and topography (B) of samples during the SF_6/O_2 plasma etching process.

2.5 CONCLUSION

In conclusion, we have studied the kinetic behavior of the DNA-mediated HF etching of SiO_2. Our result is consistent with the idea that DNA promotes the HF etching of SiO_2 by enhancing the adsorption of water near its vicinity. We identified two optimized pattern transfer conditions that can reproducibly produce 11 nm resolution patterns with high contrast. The as-patterned SiO_2 layer was used as a hard mask for plasma etching to produce sub-20 nm features in the Si substrate. These results highlight the potential of DNA nanostructure as a template for general-purpose nanofabrication.

3.0 PROGRAMMABLE-SHAPED CARBON NANOSTRUCTURE FROM SHAPE-CONSERVING CARBONIZATION OF DNA

3.1 CHAPTER PREFACE

Materials contained in this chapter were submitted as a research article to *ACS Nano*.

List of Authors: Feng Zhou, Wei Sun, Karen B. Ricardo, Jie Shen, Peng Yin and Haitao Liu.

Author Contributions: H.L. designed and directed the experiments. F.Z., W.S., K.B.R. and J.S. conducted the experiments. All authors discussed the results. F.Z. and H.L. wrote the manuscript with input from all authors.

3.2 INTRODUCTION

Recent advances in DNA nanotechnology make it possible to fabricate arbitrarily-shaped 2D and 3D DNA nanostructures through controlled folding and/or hierarchical assembly of up to several thousands of unique sequenced DNA strands.[3, 4, 9, 29, 106, 108, 109, 112, 113, 153-156] Both individual DNA nanostructures and their assembly can be made with almost arbitrarily-shaped patterns at a theoretical resolution down to 2 nm.[9] Furthermore, the deposition of DNA nanostructures on a substrate can be made with precise control of their location and orientation, making them ideal templates for bottom-up nanofabrications.[13-15]

As a template, a major limitation of pure DNA nanostructure lies in its limited chemical stability. Hence, almost all reported DNA-based nanofabrications were either based on solution chemistry or conducted at close to room temperature.[2, 42, 52, 54-56, 59, 61-63, 66-70] For example, solution phase metallization on DNA has been demonstrated using various metals (*e.g.*, Ag, Cu, Ni and Au) and can be made site-specific through modification of DNA nanostructure with binding sites that accept DNA-modified Au or Ag nanoparticles.[2, 54, 55, 59, 70] As another example, Mao and Woolley groups demonstrated vapor phase deposition of metals onto DNA, in which DNA was used to pattern vapor-phase deposited metal.[61-63] We recently also showed that DNA nanostructure can direct the etching and deposition of SiO_2 at room temperature.[42] In all these cases, high quality pattern transfer was achieved; however, due to the low reaction temperature, the obtained inorganic nanostructures are often of low crystallinity.[42]

High temperature (>500 °C) is often needed for the synthesis and crystallization of most inorganic materials, such as porous carbon. The possibility of using DNA nanostructure to direct chemical synthesis at this extreme temperature range will open up new opportunities in materials design and fabrication. However, DNA decomposes when heated to >250 ^{o}C,[49] making it seemingly impossible to achieve pattern transfer from DNA nanostructures under these conditions.

Herein, we demonstrate the fabrication of carbon nanostructures through high temperature (*ca.* 800 °C) shape-conserving carbonization of DNA nanostructures. With a thin Al_2O_3 film coating, a DNA nanostructure can be converted to carbon nanomaterial while preserving its nanoscale topography. Porous carbon material plays an important role in a wide range of applications, such aerospace structure, thermal management, fluorescent marker and energy storage.[11, 93-98, 100, 114] The nanoscale structure of porous carbon material is essential to its mechanical, thermal, and electrical properties. For example, nanoscale hierarchical porous structures can be fabricated to show very high strength (modulus ~200 MPa) at low density (<100 kg/m^3).[126, 128] Currently, the porous carbon materials are produced by carbonization of organic/polymer precursors in the presence of an inorganic template.[157] The morphology of existing porous carbon materials is limited to simple periodic lattices.[102-104] We also note that fabrication of 3D, irregular shaped carbon nanostructures is extremely challenging using existing approaches. Because DNA nanostructures (1D, 2D, and 3D) can be made into almost arbitrary shapes, our method has the potential to produce arbitrarily-shaped 1D, 2D, and 3D carbon nanostructures.

.

3.3 EXPERIMENTAL SECTION

3.3.1 Materials and Methods:

3.3.1.1 Preparation of DNA nanostructure on Si substrate

Preparation of DNA nanostructure: Synthetic and M13mp18 DNA for preparing the DNA triangle origami were purchased from IDT and New England Biolabs, respectively. The 2D DNA triangles was formed by heating the DNA solution to 95℃ followed by a slow cooling to 25℃ in 24 hrs. The resulting solution was purified by centrifuging 6 times to remove the extra short strands. DNA solution was made from TAE/Mg buffer solution (12.5 mM $Mg(OAc)_2$, 40 mM Tris, 20 mM acetic acid and 2 mM EDTA). 1D-DNA crystals and 2D DNA crystals were prepared using the DNA brick approach.[41] The buffer solution contains 40 mM Mg^{2+}.

Deposition of DNA nanostructure on Si wafer: Silicon wafers were purchased from University Wafers. It was cleaned with hot piranha solution (7 : 3 (v/v) of concentrated H_2SO_4 : 35% H_2O_2). *Warning: piranha solution presents an explosion danger and should be handled with extreme care; it is a strong oxidant and reacts violently with organic materials. All work should be performed in a fume hood. Wear proper protective equipment.* Triangular DNA origami was assembled on the substrate by dripping 2 µL of DNA solution on the substrate and waiting for 40 min before blow away the solution. The substrate was immersed in a 9/1 (v/v) ethanol/water solution to remove the salt from the buffer solution. 1D-DNA was assembled by dripping 2 µL of DNA solution for 4 min and then washing with 400 µL deionized water. After the deposition of DNA, the substrate was preceded to the deposition step within one day.

3.3.1.2 Deposition of protective inorganic film

Atomic layer deposition (ALD) of Al_2O_3 on DNA/Si substrate: The ALD was conducted by Dr. Kline and Dr. Bowman in ECE department at Carnegie Mellon University. We used trimethylaluminum as precursor. The chamber and substrate heaters were set to 200 ^oC and the Throttle valve position was set to give 200 mtorr at 260 sccm total Ar flow. The deposition looped 200 times of 0.006 s TMA pulse, 10 s interval, 0.06 s H_2O pulse and 10 s interval. The pre-set deposition thickness of both oxide films was 20 nm and the experimental thickness of the film was measured by ellipsometry. The surface of the sample was imaged using tapping mode AFM.

3.3.1.3 Annealing experiment

Typically, the prepared sandwich-like substrate was placed at the center of quartz plate in a 1-inch-diameter fused quartz tube. The furnace tube was evacuated and H_2 gas flowed at speed of 2.0 standard cubic centimeters per minute (sccm) with a pressure of 70 mTorr for 5 min. Then the furnace was heated to 800 ^oC under a 2.0 sccm of H_2. Time was recorded when the temperature reach the setting value. Then the substrate was cooled to room temperature under H_2 gas flow and taken out from the tube furnace.

3.3.1.4 Etching experiment

The Al_2O_3 film was etched in the 4.56 M H_3PO_4 solution for 1 hour, followed by rinsing with 1 M H_3PO_4 and H_2O. As shown in Figure 23, the etching procedure was studied on the annealed Al_2O_3/SiO_2 wafer and the etching rate is about 0.3 nm/sec.

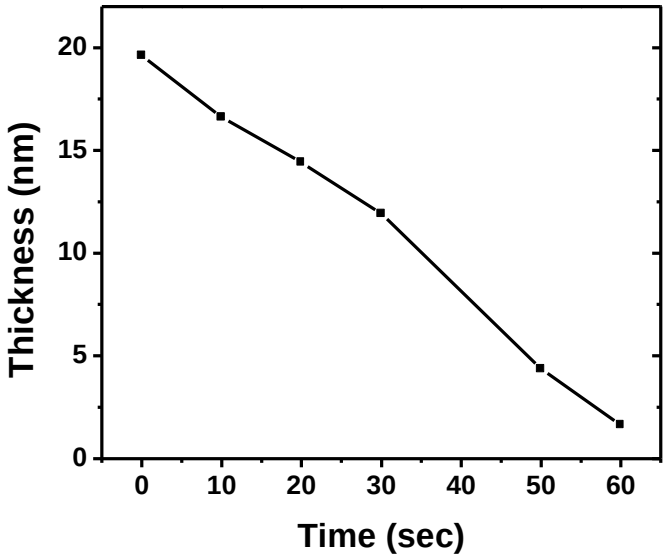

Figure 23. Etching rate of Al_2O_3 in H_3PO_4.

3.3.1.5 UV-ozone experiment

The substrate was subjected in the Novascan® PSD Pro Series UV-Ozone cleaner for UVO treatment. The UV/O3 chamber was flushed with oxygen for 5 min before UV irradiation. The typical duration for the treatment was 60 min.

3.3.2 Characterization Methods

Raman spectroscopy: Typically, the Raman spectra were measured using an ANDOR iDus® Raman microscope equipped with solid state 532 nm laser (2.33 eV) with a spot size of ~1μm (through a 40x lens). Each Raman trace was taken with 20 to 600 seconds integration time under a low incident laser power of 1.2 - 1.4 mW, thus the heating effects can be neglected.

Confocal Raman mapping: The confocal Raman mapping was performed using Renishaw inVia Raman microscope, with 633 nm laser excitation. The spatial step was 0.5 μm, and the integration time for each spot was 10 sec. The laser power was 1.7 mW and the grating was 1800l/mm.

Atomic force microscopy: Surface morphology of the carbon materials after removal of the protective film was measured by tapping mode atomic force microscopy (AFM) on a Veeco® Dimension 3100 equipped with μmasch® NSC15 tip in air.

Ellipsometry: Thickness measurements of the oxide film were carried out on an alpha-SE® Ellipsometer. The literature refractive index value of SiO_2, Al_2O_3 was 1.450 and 1.921 respectively. The refractive index was also measured by using Cauchy self-fitting model.

X-ray Photoelectron Spectroscopy (XPS): XPS was conducted in the Escalab 250XI XPS microscope. Deconvolution of the C1s peak was calculated using XPSPEAK 4.1. We note that

the carbon XPS data should be interpreted with caution because airborne hydrocarbon could contaminate the surface. This contamination is known to occur on SiO_2 surface; we recently also reported that the contamination occurs on graphitic surface as well.[158]

3.4 RESULTS AND DISCUSSION

3.4.1 RESULTS

As illustrated in Figure 24A, the carbonization procedure includes four main steps. First, DNA nanostructure was deposited onto a Si wafer substrate. Then, *ca.* 20 nm of Al_2O_3 was conformally coated onto the DNA nanostructure and the Si substrate by atomic layer deposition (ALD). The Al_2O_3-coated DNA nanostructure was then annealed in a low pressure H_2 atmosphere at high temperature, typically 800-1000 ^oC for 3 - 5 min. This step converts the DNA to carbon nanostructures. Finally, the Al_2O_3 coating was removed by a H_3PO_4 etch to expose the carbon material for further characterizations. Below we discuss two examples in more detail.

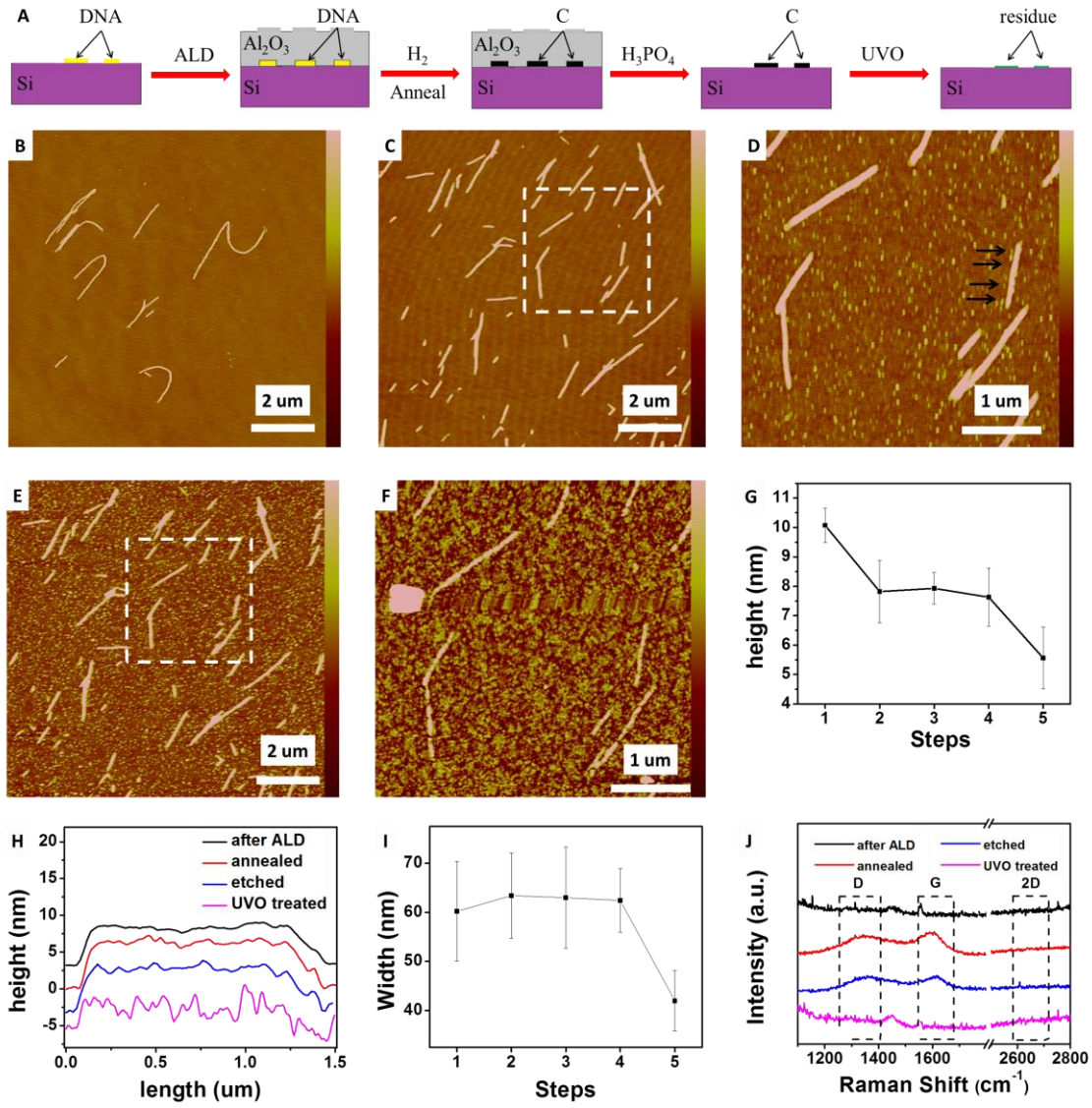

Figure 24. (A) Schematic of shape conserving carbonization of 1D DNA structure and the corresponding AFM topographic images of 1D DNA structure (B) after deposition on top of Si substrate, (C) after ALD of Al_2O_3 film, (D) after annealing at 800 ^oC for 5 min, (E) after removal of Al_2O_3 film and (F) after UV/Ozone (UVO) treatment. (G) Average height of 1-D DNA at each step. (H) Height profile of the same 1D-DNA structure, marked by arrows in Figure D. The traces were shifted in the vertical axis for clarity. (I) Average width of 1-D DNA at each step. (J) Raman spectra of 1D-DNA. The AFM height scale bars for 1D DNA (A-E) are 10 nm. Note: C-F were AFM images taken on the same location; in G and I, the horizontal axis represents the 5 steps of the fabrication process: (1) after deposition on top of Si substrate, (2) after ALD of Al_2O_3 film, (3) after annealing, (4) after removal of Al_2O_3 film and (5) after UV/Ozone treatment.

3.4.1.1 Shape conserving carbonization of 1D-DNA nanostructure: 1D DNA crystal

The 1D DNA brick crystal was constructed using the DNA brick approach.[44] An AFM image of the DNA nanostructure is shown in Figure 24B. The structures are several micrometers in length, 10.1 ± 0.6 nm in height and about 60 ± 10 nm in width (measured from 10 different samples). After coating the sample with a *ca.* 20 nm of Al_2O_3 by ALD, the AFM image of the Al_2O_3 surface still showed the characteristic shape of the DNA nanostructure. This observation is expected because ALD is a conformal coating process; therefore, the topography of the DNA is propagated to the Al_2O_3 surface. We then thermally annealed the Al_2O_3-coated sample at 800 ^oC for 5 min. The highlighted portion of Figure 24C and Figure 24D show the same area of the sample before and after the thermal annealing, respectively. Comparing these two images, it is clear that there was not change in the shape and relative position of the nanostructures. This observation is again not surprising given the high melting point of Al_2O_3 (2072 ^oC). We then proceeded to remove the Al_2O_3 coating by a wet etching of H_3PO_4 to reveal the underlying carbon nanostructures[159]; we note that this etching is specific to Al_2O_3 and does not attack carbon or SiO_2. In a separate experiment, we also confirmed the removal of Al_2O_3 by X-ray photoelectron spectroscopy (XPS) (Figure 25A and 25B). After the etching, the sample was again imaged by AFM at the same location and the image is shown in Figure 24E. It can be seen that the overall shape of the nanostructure is identical to that of the DNA template (Figure 24C). Additional experiments demonstrated that these nanostructures are indeed made of carbon (see below).

To quantify the degree of shape conservations, we measured the average height (Figure 24G) of the nanostructures at each stage of the fabrication. A minor decrease of the height was observed after ALD coating (step 1 to step 2), due to the shrinkage of DNA lattice interspace

under Al_2O_3 film. Cross sections were measured on a piece of linear DNA crystal, as marked by arrows in Figure 24D, after each processing step. The cross sections showed a high degree of similarity (Figure 24H) showing that the shape of DNA nanostructure is conserved from step 2 to step 4 (*i.e.*, ALD coating, thermal annealing, and removal of Al_2O_3). Finally, Figure 24I shows that there was no change in the width of the nanostructures after carbonization and removal of Al_2O_3.

Micro-Raman spectroscopy was used to characterize the carbon nanomaterial produced by the carbonization procedure. The DNA nanostructure do not produce detectable Raman signal due to its small Raman cross section and low surface coverage. As shown in Figure 24J, the sample became Raman active after thermal annealing. Both D band (1339 cm^{-1}) and G band (1611 cm^{-1}) were observed; both peaks are characteristic of carbon nanomaterials.[160] The Raman signals persisted after the removal of Al_2O_3 layer, indicating that the Raman active material was derived from DNA nanostructures underneath the Al_2O_3 film. The presence of G band confirms the formation of sp^2 hybridization of carbon materials (*i.e.*, graphitic carbon); the absence of 2D band at *ca.* 2700 cm^{-1} indicates the lack of large scale of conjugated sp^2 carbon structure. The strong D band indicates the presence of defects in the DNA-derived carbon material; the D band could originate from several sources: presence of edges; formation of sp^3 carbon structure during annealing; and potentially doping by the heteroatoms in DNA (*e.g.*, N atoms, see Figure 25C)). The sp^2 domain size could be estimated according to the Tuinstra-Koenig relation:[161-163]

$C(\lambda) = 2.4\times10^{-10} \times \lambda^4$ (for peak-area intensities) = 19.2 nm (for λ = 532 nm)

For 1D DNA crystals, the peak area intensity was 10149 for G peak and 23912 for D peak. The sp^2 domain size L_a = 8.1 nm

We notice that the sp^2 domain size estimated from the Raman data coincides with the height of the carbon nanostructure.

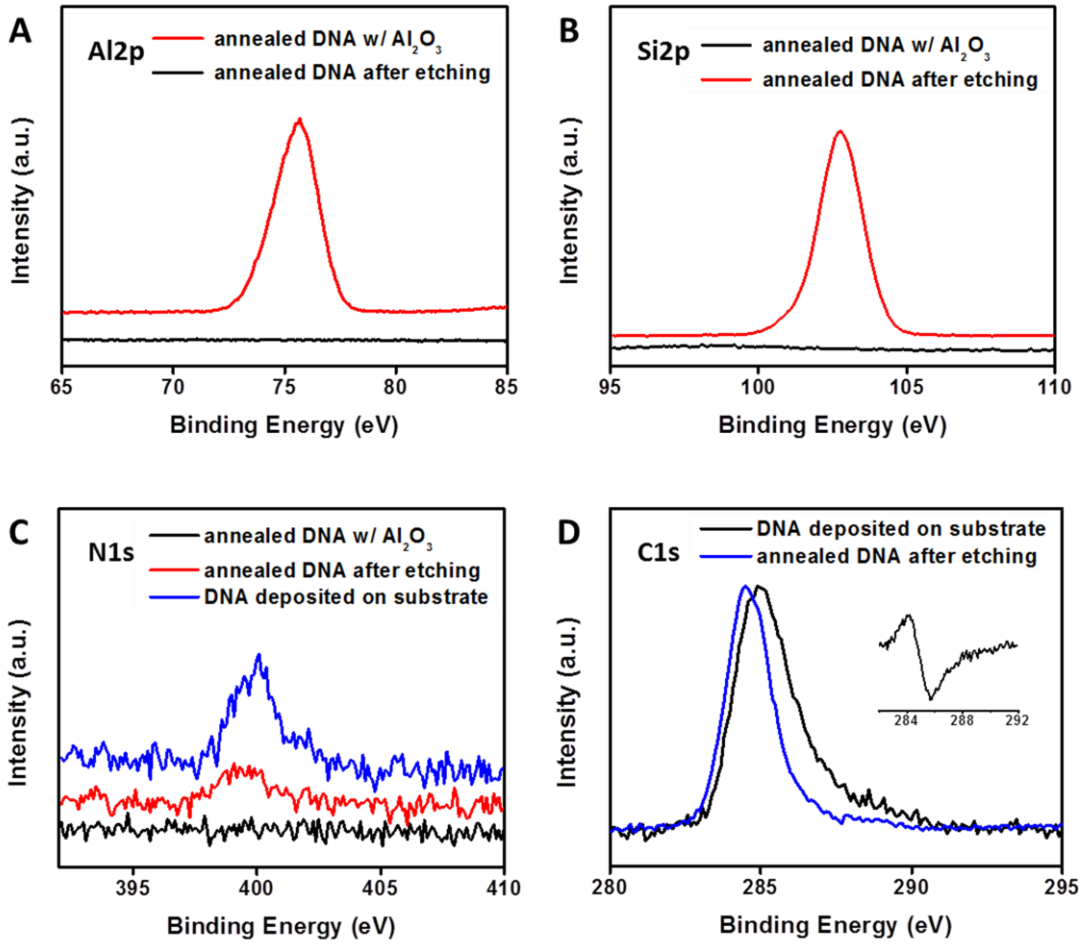

Figure 25. XPS analysis of DNA triangles after deposited on substrate, after annealing with Al_2O_3 in the presence and after removal of Al_2O_3 film. Inset in Figure D: difference between DNA before and after annealing

XPS was also used to further confirm the graphitic nature of the nanostructure product. After carbonization and removal of Al_2O_3, the C1s peak of the exposed carbon nanostructures

Table 2. Relative areas in percent of the deconvoluted components in the C1s peaks (Figure 25D) and the binding energies (eV) of the fitted peaks

	C=C	C-C	C-H	C-O-C	O=C-O
BE (eV)	284.4	284.8	285.2	286.4	288.9
DNA	22.2	1.7	48.3	24.7	3.1
Annealed DNA	69.8	2.0	25.0	3.0	0

shifted to lower binding energy from that of the as-deposited DNA (Figure 25D and inset). Deconvolution of the C1s peak identified that the largest contribution in as-deposited DNA sample came from the C-H components (Table 2). After annealing, we observed a significant decrease in nitrogen content and the sp^2 C=C species increased from 22% to 70%, confirming that the shape-conserving carbonization produced graphitize carbon nanostructures.

To further confirm the formation of carbon nanostructures, we subjected the annealed sample to an UV/Ozone treatment after the removal of Al_2O_3. Both D and G bands disappeared (Figure 24J) after the UV/Ozone treatment; this observation is consistent with the expected oxidation of carbon material by UV/Ozone. Interestingly, the nanostructures were still visible by AFM and there was no change in their shape and relative position (Figure 24F), although their average height and width decreased dramatically (Figure 24G and 24I). The height profile along an individual DNA crystal structure also showed significant increase of roughness (Figure 24H). These results suggest that while the carbon materials were removed by UV/Ozone treatment, certain oxidation-resistant materials were left on the surface. We speculate that these residues are inorganic salt from the buffer or thermal decomposition of DNA.[49, 52]

Finally, to confirm that the Raman activity was due to the annealed DNA nanostructure, we carried out confocal Raman mapping of the annealed 1D DNA crystal sample over a 10 × 10 μm area. Figure 26A shows the map of integrated intensity of the G peak region (1531 to 1661 cm^{-1}), where linear features of several micrometers in length were clearly observed. Figure 26B shows two representative Raman spectra, one taken from the linear feature and another from a spot nearby that was Raman-inactive. Only the spectrum from the linear structure showed Raman features characteristic of carbon. Those linear structures are consistent with the dimension of the DNA nanostructures measured by AFM (Fig. 24A-E), providing direct evidence that the DNA-to-carbon nanostructure transformation is shape-conserving.

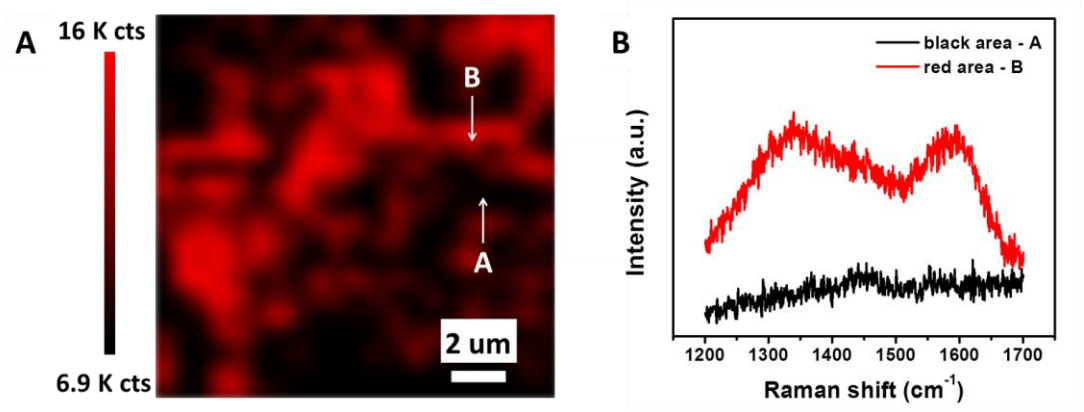

Figure 26. (A) Confocal Raman mapping of annealed 1D DNA structure at 1611 cm^{-1}, and (B) Raman spectra of two spots indicated by the arrows in (A).

3.4.1.2 Shape conserving carbonization of 2D-DNA nanostructure

Following the successful shape conserving carbonization of the simple linear DNA crystal, efforts were made to extend the methodology to more complex DNA structures. Triangle-shaped

DNA nanostructure, with height of 1.6 ± 0.2 nm and width of 28.6 ± 5.2 nm on the edge, was selected for its unique structural features (*e.g.*, linear sides, central void and sharp tips) as well as its resistance to aggregation.[9] Unlike the 1D DNA crystal, which consists of 6 overlapping layers of double stranded DNA,[41] the DNA triangle is made of just one layer of ds-DNA. Considering the carbonization yield of sugars at 800 ^{o}C is only *ca.* 30%,[164] we are curious if a continuous carbon nanostructure can be derived from only one layer of ds-DNA.

Similar to the case of 1D DNA crystals, DNA triangles retained their shape after a series of harsh treatments, including ALD, annealing at 800 ^{o}C for 5 min and removal of Al_2O_3 by H_3PO_4 etching (Figure 27A – 27D). The average width of the triangle edges changed less than 4% (Figure 27G), indicating that the DNA nanostructure was well confined during the carbonization procedure. It is interesting to notice that the average height decreased slightly after ALD (from 1.6 ± 0.2 nm to 1.3 ± 0.2 nm) and annealing (to 1.1 ± 0.2 nm), but increased (to 1.9 ± 0.2 nm) unexpectedly after the removal of Al_2O_3 (Figure 27F). It is known that the apparent height measured by AFM is sensitive to the tip-substrate interaction and may deviate from the actual height by as much as 1 nm, especially in cases where the sample and the substrate are chemically different (*e.g.*, carbon *vs* SiO_2).[165] High resolution AFM image was taken after the removal of Al_2O_3 film; the image presented a continuous, intact triangular nanostructure with a central void (Figure 27D, inset).

Micro-Raman spectroscopy was conducted to detect the presence of carbon materials at each step. Similar to the case of 1D DNA crystal, the DNA triangles sample became Raman active after annealing at high temperature, showing clear D and G bands; such Raman features were still observed after the removal of Al_2O_3 coating (Figure 27H), indicating successful carbonization of DNA material. After exposure to UV/Ozone, the triangle-shaped nanostructure

(Figure 27E) disappeared along with the D and G bands in the Raman spectra (Figure 27H), proving that the triangular nanostructures in Figure 27D were indeed made of carbon. In a control experiment, we also treated the samples with UV/Ozone before removing the Al_2O_3 coating. In this case, we observed no change in the Raman activity and AFM topography of the sample (Figure 28). This control experiment showed that the carbon material was underneath the Al_2O_3 film and that the Al_2O_3 coating protects the carbon material from oxidation by O_3.

This shape conserving carbonization approach is compatible with other DNA templates as well. As another example, we show that a large 2D DNA crystal, prepared using the DNA brick approach,[41] maintained its shape after the carbonization. Figure 29A and 29B are AFM image of the 2D DNA crystal before and after thermal annealing; the height profiles present similar surface features, with the same height of 1.82 ± 0.15 nm. The Raman spectra show that D and G bands appeared after annealing (Figure 29C). In addition, Raman mapping showed that the Raman activities originate from micron-sized objects whose dimensions are similar to that of the 2D DNA structures (Figure 29D); this data again shows that the carbonization of DNA nanostructure is a shape-conserving process.

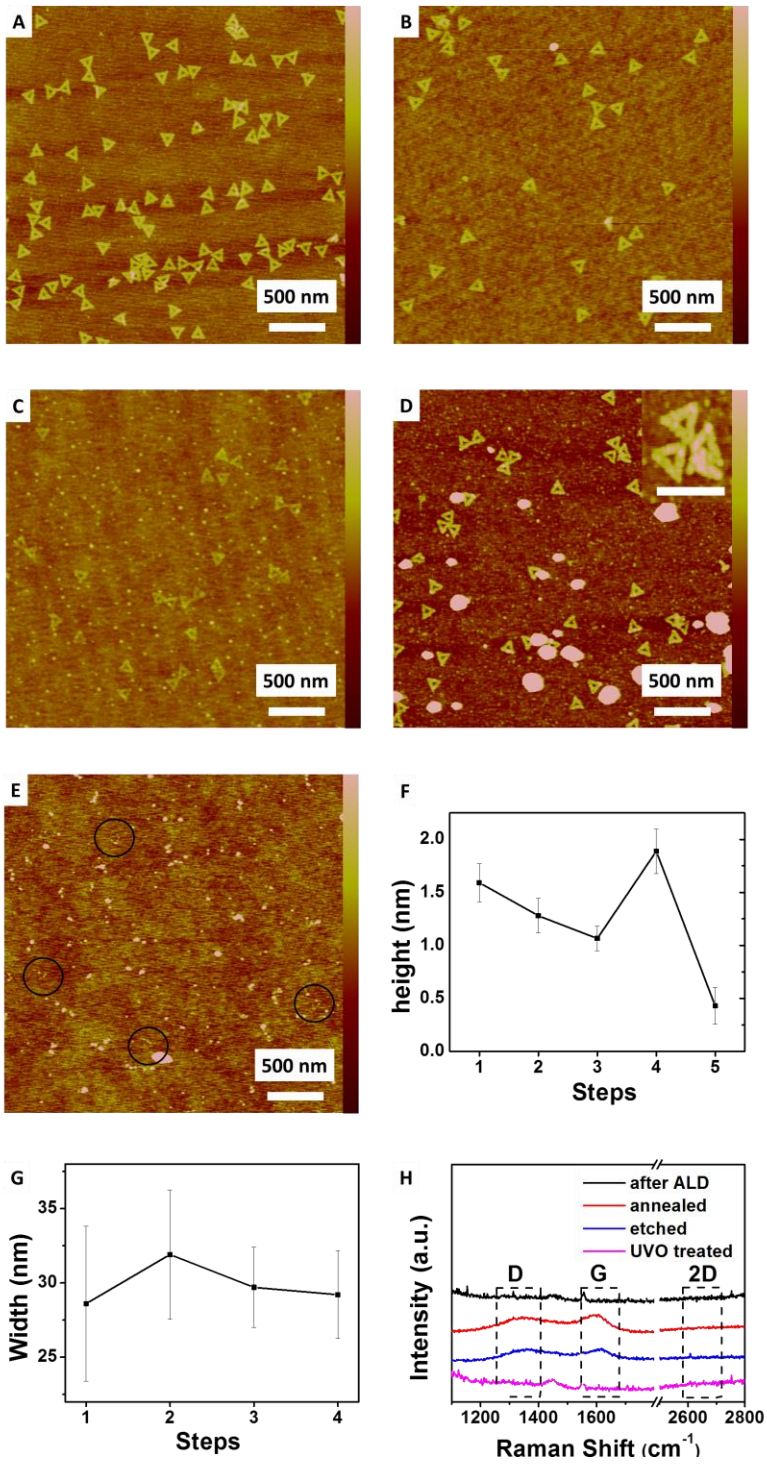

Figure 27. AFM topographic images of DNA triangle (A) after deposition on top of Si substrate, (B) after ALD of Al_2O_3 film, (C) after annealing at 800 ^oC, (D) after removal of Al_2O_3 film and (E) after UVO treatment. (F) Average height and (G) width of DNA triangles at each step. (H) Raman spectra of DNA triangle at each step. The AFM height scale bars for DNA triangle (A-D) are 5 nm respectively. In E, the height bar is 2 nm and the circles highlight several non-carbon residues.

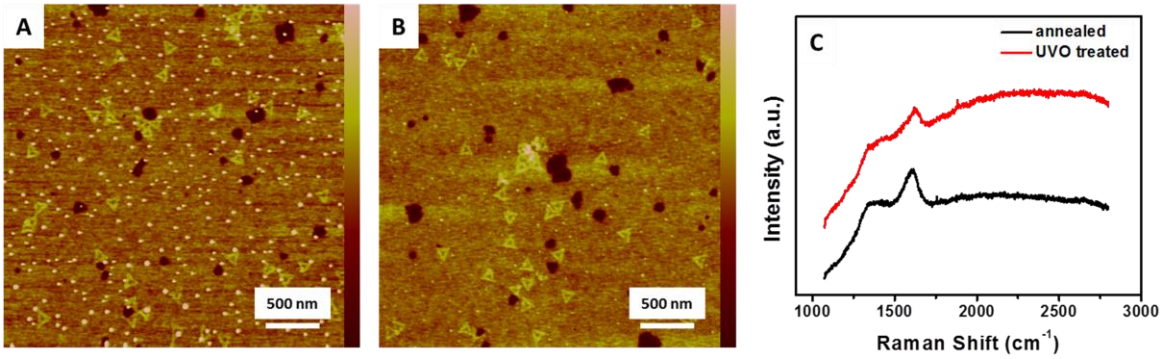

Figure 28. AFM images of (A) the annealed Si/DNA and (B) the same wafer after 2 hour UV/Ozone treatment; (C) Raman spectra of both samples. The height bar for A and B is 5 nm. Note that the Al_2O_3 coating was not removed in this case.

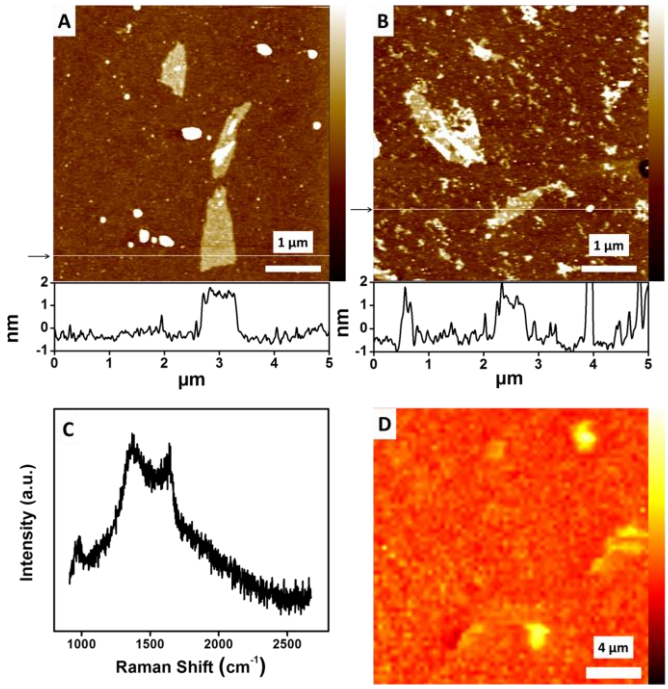

Figure 29. AFM topographic images of 2D DNA crystals (A) after deposition on top of a Si substrate and ALD of Al_2O_3 film; and (B) after annealing at 800 ^oC. (C) Raman spectra of annealed 2D DNA crystals by subtraction against the Raman spectra of annealed Al_2O_3/Si (soaked in buffer and rinsed with ethanol water mixture before ALD) using Si overtone peak for intensity calibration; (D) confocal Raman mapping of annealed 2D DNA crystals at 1611 cm^{-1}. Height bars represent 5 nm in (A) and (B), and 372 a.u. in (D).

3.4.2 DISCUSSION

Almost any organic materials can be carbonized, including sugar, synthetic polymers, and cellulose.[157] Among them, the best substrates for carbonization are those with aromatic rings. DNA is composed of three major components: the phosphate backbone, the sugar, and the four bases. Among the three, sugar is known to carbonize to produce amorphous carbon.[164] The four bases are aromatic and structurally similar to a large number of compounds (*e.g.*, polyimide) that carbonize.[166, 167] However, bulk DNA decomposes to produce gaseous products when heated to >250 ^{o}C,[49] making it a challenge to achieve pattern transfer from DNA nanostructure at typical carbonization temperatures (>500 ^{o}C). We note that Cu^{2+}-impregnated DNA filaments have been used to catalyze the growth of graphene nanoribbons; however, the degree of shape conservation was not reported in that work.[115] Our work is the first to demonstrate precise shape conservation between the DNA templates and the resulting carbon nanostructures.

3.4.2.1 Systematic study of carbonization condition

We found that the 20 nm Al_2O_3 film is a key component in the success of our experiments. In a control experiment, we annealed a DNA triangle sample without the Al_2O_3 film. Although triangular shaped structures were still observed after annealing (Figure 30A), they are significantly lower (0.58 ± 0.14 nm) in height, and there was no D and G band observed (Figure 30B, red). We believe that this Raman-inactive structure is the salt residue following decomposition of DNA.[49, 52] In contrast, in the presence of Al_2O_3 film even a single layer of ds-DNA is capable of producing carbon material (Figure 30B, green) and preserving its nanoscale morphology. Our control experiments also showed that a *ca.* 20 nm of Al_2O_3 coating is impermeable to gas at room temperature (Figure 28). We speculate that in addition to preserving

the shape of the nanostructure, Al_2O_3 coating also prevents or slows down the decomposition products of DNA from escaping and as a result increases the carbonization yield.

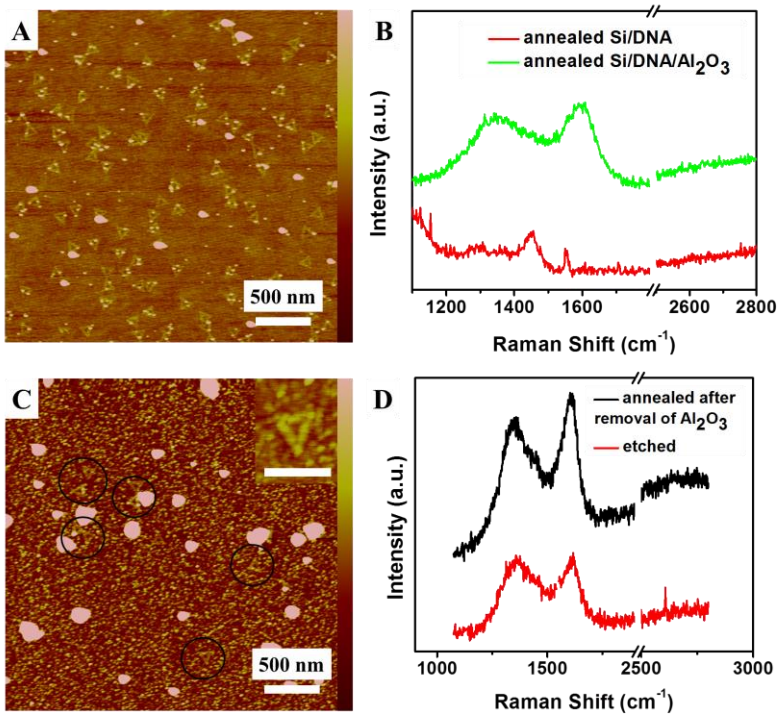

Figure 30. AFM images of (A) the annealed Si/DNA and (C) annealed Si/carbon material; Raman spectra of (B) annealed Si/DNA with and without Al_2O_3 film and (D) comparison of the exposed carbon material before and after the second annealing. The height bar for A and C is 5 nm; the scale bar for the inset of C is 200 nm. The circles in C indicate location of carbon nanostructures.

With the Al_2O_3 coating removed, the carbon nanostructure broke down to small particles after heating at 800 °C for 5 min (Figure 30C), indicating poor stability of graphitic structures at high temperature, likely due to the enhanced diffusion. However, storing an annealed sample (with Al_2O_3 removed) at room temperature did not lead to degradation of the nanostructure, as indicated by the AFM images (Figure 31A and 31B) and Raman spectra (Figure 31C) taken on the same sample. Finally, additional experiments showed that the carbon nanostructures are stable upon repeated AFM imaging and is not affected by laser induced heating in the time scale of our Raman measurement.

To determine the mechanic stability of the nanostructure, tapping mode AFM was utilized on the same area for 5 times to test whether physical damage during scanning can be introduced. The DNA-derived nanostructure resisted the tip friction in the manner of both surface morphology (Figure 31D) and the average height (from 2.1 ± 0.2 to 2.1 ± 0.3 nm), indicating the good mechanic stability.

Since the laser spot in Raman experiments could heat up the sample up to several hundred degrees, it is important to understand the thermal stability of the graphitic nanostructure in air. Figure 31E shows that there was no change in Raman spectrum after 1 hour of Raman laser illumination. However, the signal disappeared after the sample was illuminated by laser overnight, indicating that oxidation occurred. The typical Raman integration time used in our study was 30-600 seconds and therefore our Raman data is not affected by laser-induced thermal heating effect.

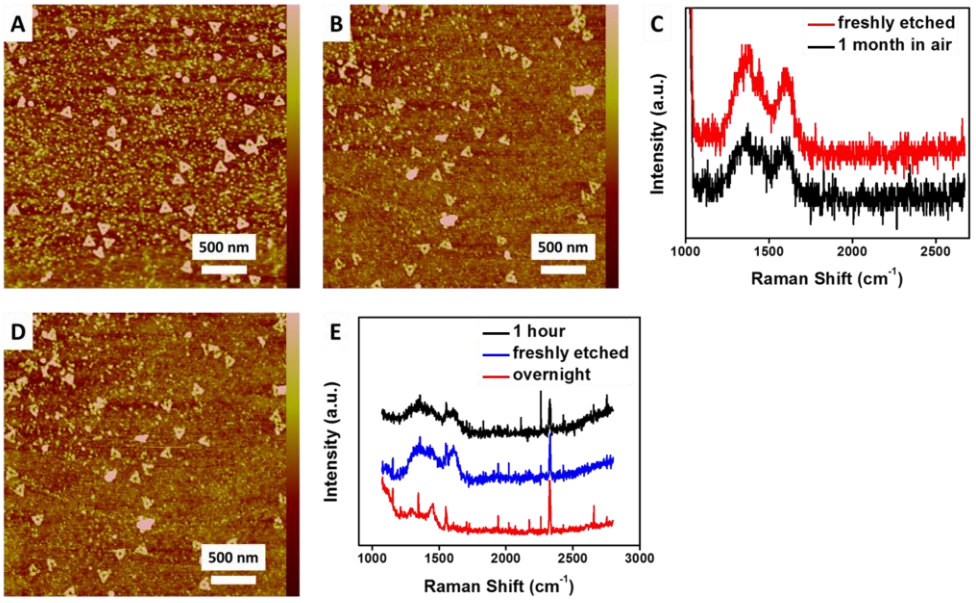

Figure 31. AFM images of carbonized DNA (A) right after etching to remove Al_2O_3, (B) after stored in lab for 1 month and (D) after 5 times same location tapping mode AFM scanning. (D) Raman spectra of freshly etched carbonized DNA and that after 1 month storage in lab. The height scale bars represent 5 nm in all AFM images.

The annealing conditions were systematically varied to study the effect of temperature, duration and gas environment on the carbonization. To understand the effect of temperature, we carbonized the triangle DNA nanostructure at 780 ^{o}C, 800 ^{o}C and 1000 ^{o}C; in all three cases, the Raman spectra showed clear D and G bands (Figure 32A), indicating that the carbonization occurred over a wide temperature range. We note that DNA contains sugar and aromatic rings and previous studies have showed that similar structured materials undergo carbonization at this temperature range.[165] To evaluate the effect of annealing time, two Al_2O_3-coated DNA triangle samples were annealed at 800 ^{o}C for 5 min and 20 min, respectively. Raman spectra (Figure 32B) and AFM images (Figure 27C and 32C) showed that in both cases, the shape conserving carbonization occurred. Additionally, the same 1D DNA crystal sample was annealed at 800 ^{o}C for 5 min and then subjected to 1000 ^{o}C annealing for another 3 min. AFM topography images

(Figure 24D and Figure 32D) and height profiles (Figure 32E) indicate remarkable preservation of nanostructure and Raman spectra (Figure 32F) show D and G peaks after both annealing. These results show that the carbonization was completed within 5 minutes and the carbon structure can be preserved at high temperature during extended heat treatment, owing to the high melting point of Al_2O_3 film. The effect of gas environment was studied by heating the Al_2O_3/DNA/Si samples in H_2, Ar and air at 800 ^oC for 5 min. In the case of H_2 and Ar, the Raman spectra show apparent D and G peaks, while no graphitic signal was observed from the samples annealed in air (Figure 32G). Furthermore, for the sample annealed in H_2, we subject it to a second annealing in air at 800 ^oC for another 5 min, and the D and G peaks vanished (Figure 32H). Compared with the previous demonstration of additional annealing in H_2 atmosphere, the results indicate that the carbonization procedure required inert atmosphere since the Al_2O_3 film was not impermeable to O_2 at high temperature although it does provide protection against UV/O_3 oxidation (Figure 28).

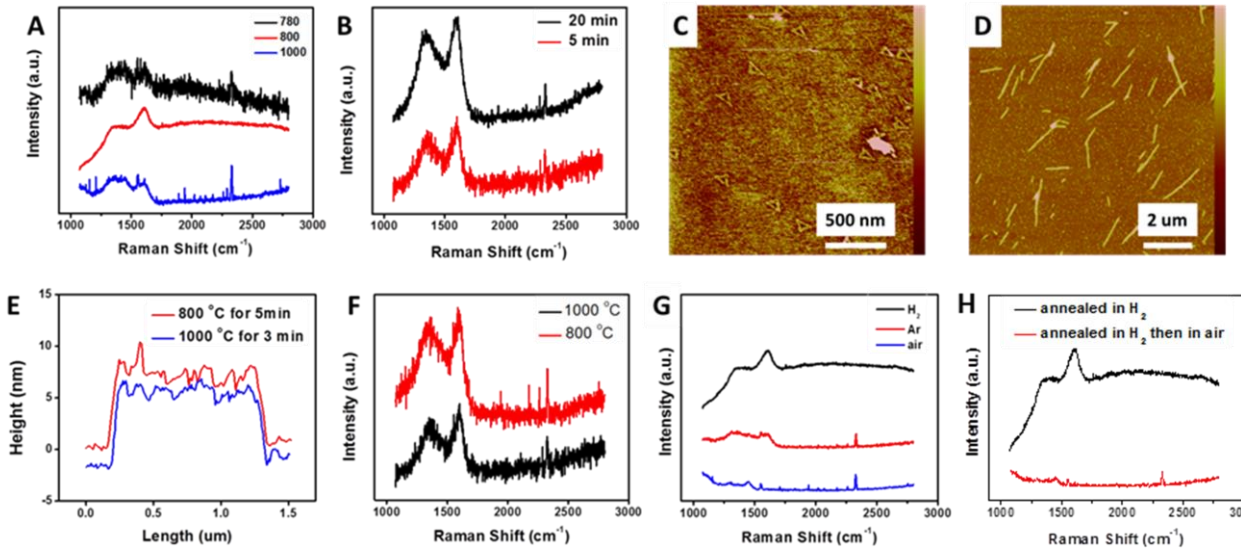

Figure 32. Raman spectra of annealing experiments (A) at various temperature, (B) in different duration and (G) environment. (C) AFM image of DNA triangles annealed for 20 min. (D) AFM image of 1D DNA crystal annealed at 1000 ^{o}C for another 3 min. (E) Height profile and (F) Raman spectra of 1D DNA crystal after annealing at 800 ^{o}C for 5 min and at 1000 ^{o}C for another 3 min. (H) Raman spectra of DNA triangles after annealing in H_2 for 5 min and in air for another 5 min. The height scale represents 2 nm in C and 20 nm in D, respectively.

3.4.2.2 Origin of carbon

Carbon source other than DNA nanostructure could be introduced during the carbonization process. Possible non-DNA carbon source include the airborne carbon contamination,[158] the byproduct of ALD,[168] and the buffer solution used for DNA deposition. Control experiments were conducted to determine the possible contribution from all these sources, as detailed below.

As shown in Figure 33A, the Raman spectrum taken from annealed Al_2O_3/Si, which was prepared from direct deposition of Al_2O_3 on the blank Si surface (without DNA), showed no D or G peak, indicating the ALD product residue and airborne carbon contaminations do not

produce carbon material. Similarly, we found that the buffer solution did not introduce significantly amount of carbon precursor. During the deposition of the 1D DNA crystals, the Si wafer was rinsed with water after the DNA deposition. A control sample was prepared by soaking a Si wafer in a DNA-free buffer solution, followed by rinsing the wafer with water. This sample was then coated with Al_2O_3 and no carbon material was detected by Raman spectroscopy after thermal annealing (Figure 33A). The preparation for DNA triangle and 2D DNA crystal samples involve rinsing with an ethanol-water mixture. In this case, the control sample (Si wafer soaked in DNA-buffer, then rinsed with ethanol-water mixture) showed weak D and G peaks in the Raman spectrum after ALD coating and annealing (Figure 33A). However, the Raman signal intensity is 22% - 27% of that from samples having deposited 1D and 2D DNA crystals.

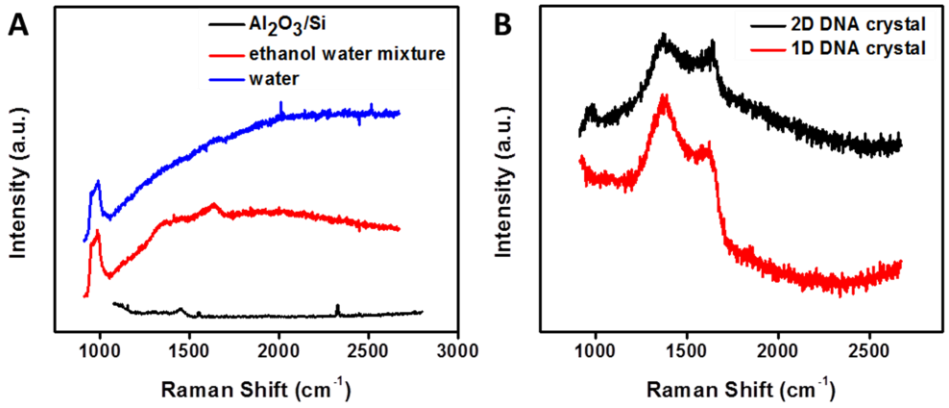

Figure 33. (A) Raman spectra of annealed Al_2O_3/Si, Al2O3/Si (Si soaked in buffer and rinsed with ethanol water mixture before ALD) and Al_2O_3/Si (Si soaked in buffer and rinsed with water before ALD). (B) Raman spectra of 1D DNA crystal and 2D DNA crystal after subtraction against the Raman spectra of annealed Al_2O_3/Si (soaked in buffer and rinsed with ethanol water mixture before ALD) using Si overtone peak for intensity calibration.

3.5 CONCLUSION

We have demonstrated that DNA nanostructures can be converted to carbon nanostructures of the same shape by high temperature annealing. A thin Al_2O_3 coating was found to be essential to preserving the shape of the carbon nanostructures. Although the application of DNA nanostructures have long been limited to room temperature, aqueous environments, our work showed that they are also useful as material templates for high temperature solid state chemistries. We hope that this case study may catalyze further use of DNA nanostructure in the fabrication of inorganic nanostructures.

4.0 LOW-DENSITY HIGH-STRENGTH DNA TETRAHEDRON

4.1 CHAPTER PREFACE

Materials contained in this chapter were in preparation for publication as a research article.

List of Authors: Feng Zhou, Wei Sun, Peng Yin and Haitao Liu.

Author Contributions: F.Z. and H.L. designed and directed the experiments. F.Z. and W.S. conducted the experiments. All authors discussed the results. F.Z. and H.L. wrote the manuscript with input from all authors.

4.2 INTRODUCTION

Structural DNA nanotechnology is able to produce a wide range of 3D nanostructures with programmable structure, size, molecular weight and high resolution.[4, 9, 11, 24, 25, 34, 38, 40, 41, 46, 81, 130, 133-136] DNA nanostructures are soft materials, however, and their applications have long been limited to aqueous environments. Further complications arise when drying the 3D DNA nanostructures. Upon drying, these structures inevitably collapse or rupture under the capillary force.[169] For this reason, studies on the mechanical properties of DNA nanostructure in a dry state have not been reported.

Here we report a simple but robust method to obtain a free-standing 3D DNA nanostructure on a solid substrate, such as SiN and mica. We show that by adsorbing uranyl acetate onto a DNA frame followed by lyophilization, it is possible to obtain a free-standing 3D DNA nanostructure in air. The free-standing 3D DNA nanostructure was characterized by tapping mode atomic force microscopy (AFM) in air as well as transmission electron microscopy (TEM). The mechanical properties of the 3D DNA nanostructure were studied by AFM indentation. We found that the DNA nanostructures show surprisingly high mechanical strength. The collapsing force (42 ± 22 nN) was two orders of magnitude higher than the corresponding values of double-helix DNA tetrahedra or DNA nanopillars[24, 77] or the simulated force response[34] for DNA nanostructure molds. The effective hardness (9.1 ± 5.1 MPa) and Young's modulus (77 ± 48 MPa) of our low-density ($70.7 kg/m^3$) DNA structure were comparable to the reported

ceramic nanolattices,[126] nanotubular bulk materials,[132] and foams.[170] This is the first report on the mechanical properties of free-standing 3D DNA nanostructure.

4.3 EXPERIMENTAL SECTION

4.3.1 Materials and Methods:

4.3.1.1 Preparation of free-standing DNA tetrahedron on mica

DNA tetrahedron was synthesized following the DNA tripods assembly method.[46] It was assembled on a 0.5 × 0.5 cm^2 freshly-cleaved mica surface by dripping 5 µL of DNA solution on the substrate and waiting for 5 min. Then, uranyl acetate (2 µL, 1%) was added on the wet sample for 45 sec. The sample was then rinsed with ethanol-water mixture (v/v: 9/1) to remove the extra salt. The wet sample was immersed into liquid N_2 to freeze the surface, and subjected to lyophilization at around 100 mTorr overnight.

4.3.2 Characterization Methods

Atomic force microscopy: Surface morphology of the DNA tetrahedral structures after drying and mechanical properties of the free-standing DNA tetrahedral structures were measured by tapping mode atomic force microscopy (AFM) and contact mode force AFM on an Asylum MFP-3D AFM equipped with µmasch® NSC15 tip in air.

In a single indentation experiment, the force distance was set as 200 nm, the trigger force point was set as 100 nN and the scan rate was set as 0.99 Hz. In a force mapping experiment, the

force distance was set as 200 nm, the trigger force point was set as 300 nN, the scan rate was set as 0.99 Hz and the point distance was set as 67 nm.

Transmission electron microscopy: A SiO_2 window TEM grid (SO100-A20Q33, SiMPore Inc.) was pre-treated with UV/ozone for 2 hour to generate hydrophilic surface. TEM samples were prepared following the same procedure for free-standing DNA tetrahedral structures. TEM was conducted on a JEOL 200CX instrument operated at 200 kV and equipped with a Gatan CCD image system.

4.4 RESULTS AND DISCUSSION

4.4.1 Free-standing DNA tetrahedron in air

A DNA tetrahedron, with a dimension of 100 nm in length and 12 nm in thickness for each arm, was synthesized by self-assembly of DNA tripods. The free-standing DNA tetrahedral structures were prepared by uranyl acetate absorption and freeze drying. The DNA tetrahedra were first incubated on the mica substrate for 5 min, followed by staining with 1% uranyl acetate for 45 sec. The sample was then rinsed with ethanol-water mixture (v/v: 9/1) to remove the extra salt. The wet sample was immersed into liquid N_2 to freeze the surface, and subjected to lyophilization at around 100 mTorr overnight. Tetrahedral structures, with length of 158 ± 5 nm and height of 93 ± 2 nm (20 samples were measured), were found in the tapping AFM images (Figure 34A, 34B). The dimension of these structures matches that of the free-standing DNA tetrahedron (expected length: 100 nm and height: 82 nm. Note that the length measured by AFM will be larger than the theoretical value due to tip-convolution effect), indicating that the DNA

tetrahedrons did not collapse. We note that this is the first characterization of a 3D DNA hollow structure using tapping mode AFM in air, suggesting a significant improvement of mechanical stability of the stained structure. Additionally, the bright-field TEM images showed that only the wire-frame of the DNA nanostructures has been stained by UO_2^{2+}; the center of the DNA nanostructure is free of inorganic residue. The edge of the DNA tetrahedron measured by TEM is 100 ± 6 nm with a thickness of 11.5 ± 2.2 nm (Figure 34C). These dimensions are comparable to the expected values of the pristine DNA nanostructure, indicating that the UO_2^{2+} stain did not compromise the DNA nanostructure.

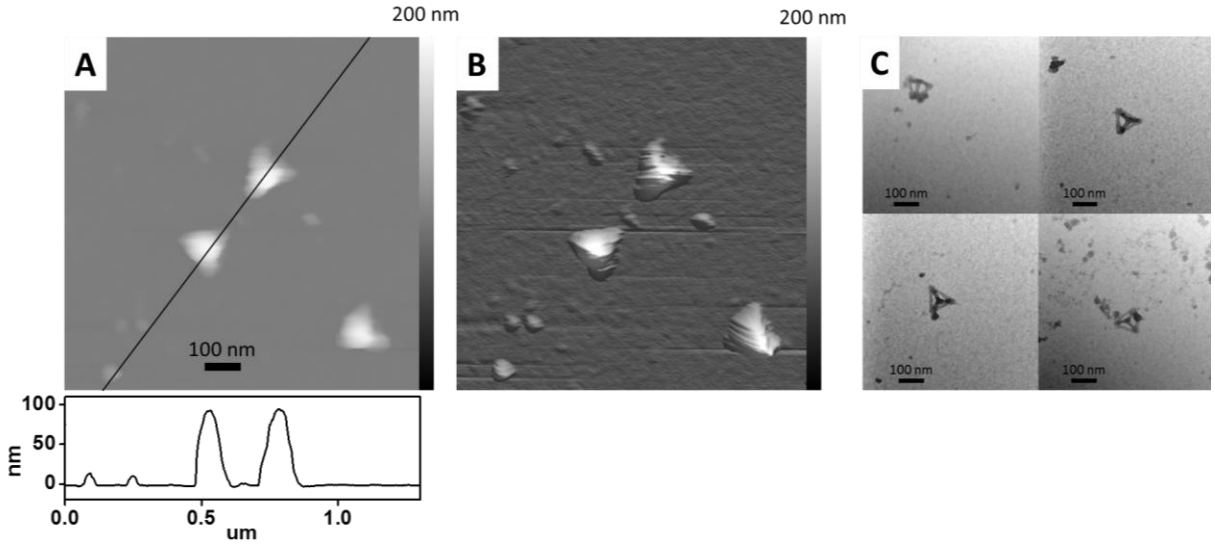

Figure 34. Structural analysis of free-standing DNA tetrahedrons. (A) AFM image (top) and cross-sectional analysis (bottom) of the DNA tetrahedral deposited on mica in air. (B) 3D surface plots of the DNA tetrahedral on the same location as in (A). (C) TEM bright-field images of free-standing DNA tetrahedrons deposited on a SiO_2 grid.

4.4.2 Systematic study on drying conditions for free-standing DNA tetrahedron in dry state

Both the adsorption of UO_2^{2+} and the freeze-drying played a key role in obtaining the free-standing structure. In a control experiment, we freeze-dried the DNA nanostructure without UO^{2+} staining and found the structures collapsed (Figure 35A). During the staining step, one uranyl ion (UO_2^{2+}) binds to each phosphate group in DNA.[171] We suspect that this absorbed UO_2^{2+} thin film on the DNA provides additional stability and strength to sustain the 3D nanostructure in the dry state. In another control experiment, we dried the stained DNA sample using a N_2 gas flow. AFM imaging showed that the DNA nanostructures were collapsed, as

evidenced by the much reduced height of 24 ± 5 nm (Figure 35B). Furthermore, the thickness of each rod in the free-standing DNA nanostructure (11.5 ± 2.2 nm) was almost the same as that of the regular stained DNA tetrahedrons (11.4 ± 1.2 nm[46]), indicating that lyophilization did not compromise the resolution of the DNA nanostructure .

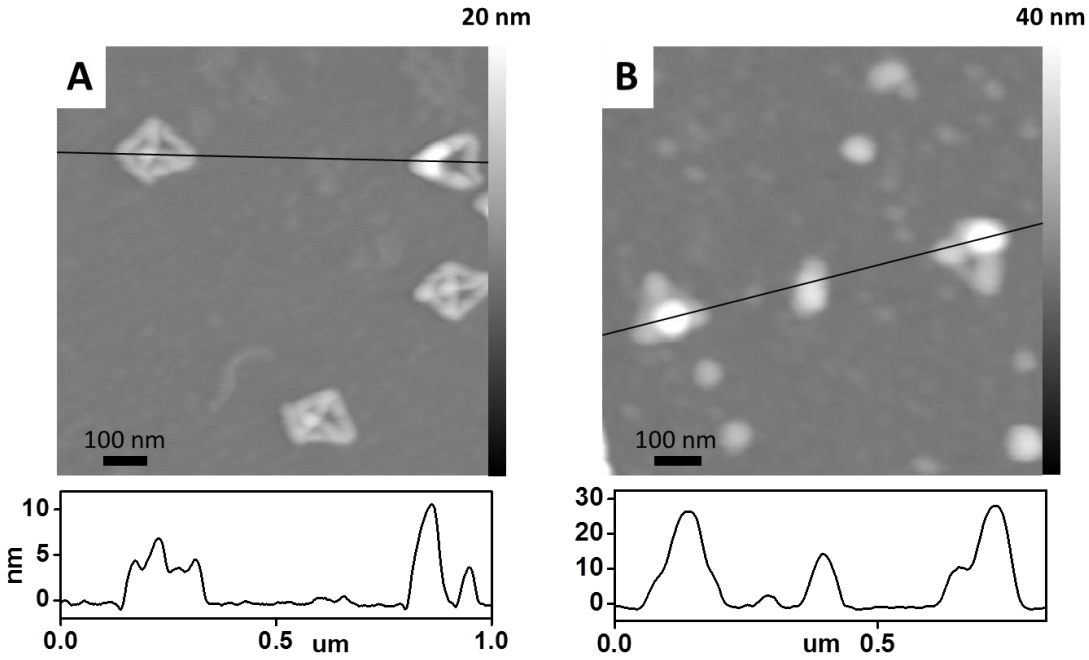

Figure 35. (A) Freeze-dried DNA tetrahedral structures without staining. (B) Stained DNA tetrahedral structures without freeze drying.

We attribute the collapse of the DNA nanostructure to the capillary force at the liquid-gas-DNA interface. During the solvent evaporation, the DNA nanostructure pins the solid-liquid-gas interface and the capillary force exerts a downward pressure onto the nanostructure. Using the surface tension of water/ethanol mixture and the dimension of the DNA nanostructure, we estimate that the capillary force experienced by the DNA nanostructure is on the order of 3.8 nN. Given the simplicity of the model, this value should be regarded as a rough estimate of the force that an individual DNA nanostructure can sustain. Thus, the stabilization of a hollow 3D DNA nanostructure requires efforts on both enhancing the mechanical properties of the DNA structure and avoiding the capillary force during drying

4.4.3 Mechanical properties from single indentation using AFM

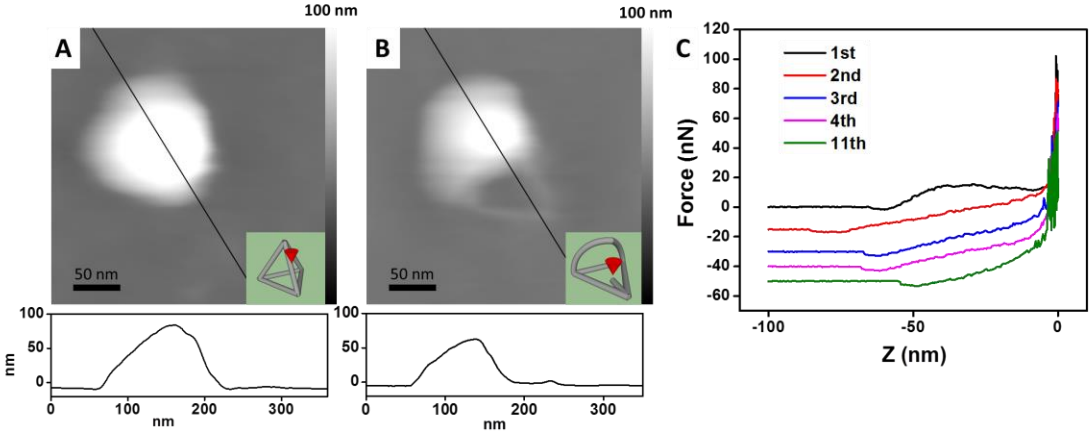

Figure 36. Single indentation experiments on individual DNA tetrahedral structure. AFM image and cross-sectional analysis of free-standing DNA tetrahedral (A) before and (B) after indentation experiments. (C) Multicycle force curves of DNA tetrahedral on the same spot. The cartoon insets in A and B represent the relative location between the AFM tip and free-standing tetrahedron.

AFM was used to characterize the mechanical properties of the free-standing DNA nanostructure. In a typical experiment, a tapping mode scan was first conducted to locate the DNA nanostructures. The AFM tip was then suspended over a DNA nanostructure and force-distance curve was measured (Figure 36C). The force response showed an approximate linear response at the beginning. This linear region is typically followed by a sudden decrease in the force at *ca.* 20 nN, which we attributed to the collapse of the DNA nanostructure. After an additional 50 nm displacement, the force response showed another steep increase, indicating that the DNA nanostructure is completely collapsed and the AFM tip has reached the supporting substrate. The collapsing feature was not observed upon repeated indentation on the same location, suggesting that the indentation-induced deformation was irreversible (Figure 36C). We also used tapping-mode AFM to characterize the DNA nanostructure before and after indentation. In this case, we found that the height of the tetrahedron decreased from 89 nm to 62 nm and a triangular base was clearly visible. From the post-indentation AFM images, we conclude that a partial collapse occurred during the indentation and that the collapsing feature in the force curve was indeed the sign of the deformation of the free-standing DNA nanostructure.

4.4.4 Mechanical properties from force mapping using AFM

Force mapping was carried out to obtain the statistics of the mechanical properties of the free-standing DNA tetrahedrons. In this experiment, an area full of standing tetrahedrons was selected by tapping mode AFM imaging and then, the same AFM tip scanned the surface to collect force-distance curves; single indentation was performed in multiple spots in this area and the distance between adjacent indentation spots was 67 nm in both dimensions to insure the coverage of the 3D nanostructure; the AFM tip was suspended while moving between adjacent spots to prevent

damage other than indentation on the surface. The force threshold to withdraw the tip was set as 300 nN, which was supposed to collapse the DNA tetrahedrons. After force mapping, another topping mode AFM image was collected. We found that the height of many DNA nanostructures in the mapping region decreased to *ca.* 20 nm (Figure 37A and 37B), consistent with structure collapse. To eliminate the possible damage caused by the tapping mode scanning, the force mapping was then conducted on a fresh surface on the same sample, without imaging beforehand. We selected and studied 84 force curves with the following features that are consistent with structural collapsing (Figure 37C): (i) compression with a linear force response; (ii) collapse and relaxation; (iii) compression of the collapsed structure; (iv) unloading of the AFM tip. In some circumstances, multiple collapses occurred during the indentation, showing as multiple peaks in the force curve (Figure 37D). This could be caused by the partial collapse and stepwise deformation of the rigid tetrahedron structure. Since the diameter of the stained DNA rod was 11.5 nm, the displacement of the force curve larger than the thickness of two overlapping DNA rods, which is 23 nm, would indicate the collapse of the hollow nanostructure. Considering this criteria, 50 indentation results from the force mapping meeting the requirement were studied for the compression behavior on the free-standing 3D nanostructures.

The average collapsing force was 42 ± 22 nN, which was two orders of magnitude larger than the reported value on the collapsed double-helix DNA tetrahedron and three orders of magnitude larger than the DNA nano-pillar.[77] The average compressing distance before collapse (distance between the initial contact and the collapsing point) was 9.1 ± 4.3 nm. The force response below the collapsing force was 5.2 ± 3.1 nN/nm, which was two orders of magnitude larger than the simulated value of the DNA origami box structure.[34] The large variation of the collapsing force can be explained by the randomness of the placement of the AFM tip on the

DNA nanostructure and the apex to the center of the rod, or the void of the side facet. We measured the indentation depth before the sample collapsed as the compressive distance. There was no obvious correlation found between the collapsing force and the compressing distance.

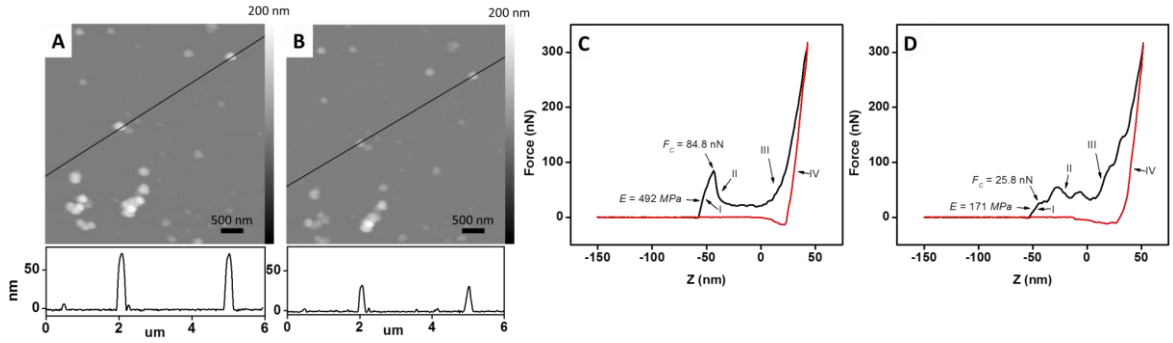

Figure 37. Compression experiments of free-standing DNA tetrahedral via force mapping. AFM image and cross-sectional analysis of free-standing DNA tetrahedral before (A) and after (B) force mapping. (C and D) Force curves of DNA tetrahedral during force mapping.

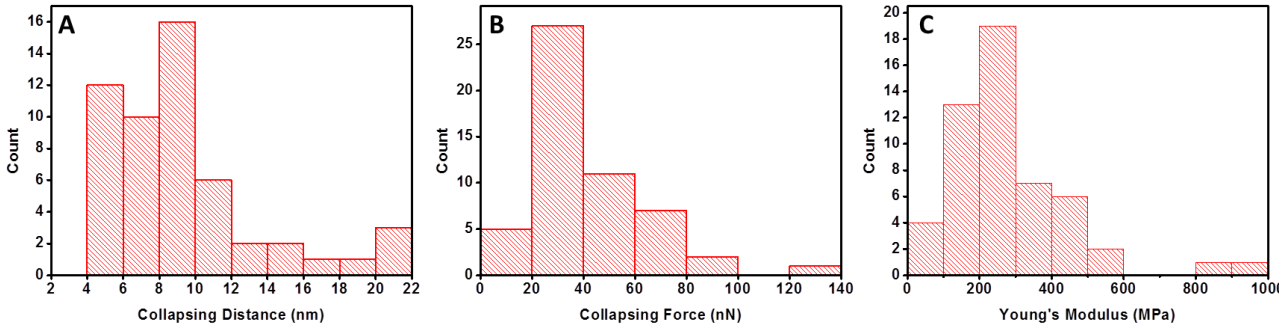

Figure 38. Statistics of (A) collapsing distance, (B) collapsing force and (C) Young's Modulus of free-standing DNA tetrahedral during the compression experiments via force mapping.

The effective hardness was calculated to be 9.1 ± 5.7 MPa and the effective Young's modulus as 77 ± 48 MPa (Figure 38). The density of the stained nanostructure was estimated as 70.7 kg/m^3. The stained nanostructure is a low-density, high-strength material, comparable to the brittle nanolattice.[126]

To get a better understanding of the mechanical enhancement of the staining on the DNA structures, the Young's modulus of the individual rod in the DNA tetrahedron needs to be calculated from the force mapping data. To simplify the situation, we assume the individual DNA rod which bears the compression pressure as a buckling column.

The collapsing force (F_C) applied on the top apex of DNA tetrahedron from the AFM tip is 32.7 ± 8.1 nN, based on 4 force curve data with a total indentation displacement (the distance between the initial contact and the final point) close to the height of DNA tetrahedron 93 nm (within 5 nm deviation). The calculated Young's modulus is then 15.2 ± 3.8 GPa. Compared to the reported Young's modulus of dsDNA (100 – 300 MPa[74-76, 172]) or DNA origami (75 – 180 MPa[172] or 112 - 126 MPa for bending modulus[77, 78]), the individual stained DNA rod in the free-standing DNA tetrahedron is two orders of magnitude stronger.

4.5 CALCULATION DETAILS

4.5.1 Estimation of the capillary force on the DNA tetrahedron when drying from 9/1 (*v/v*) ethanol/water mixture

Two models are discussed estimate the capillary force experienced by the DNA tetrahedron during the drying process. .

1. During drying, the 9/1 (*v/v*) ethanol/water solution evaporates and exposes the apex of the DNA tetrahedron above the water meniscus (Figure 39A). In this case, the capillary force is generated by the surface tension at the liquid-gas-DNA interface, along the DNA rod, and is pointing towards the center of the tetrahedron (Figure 39A inset). The downward capillary force experienced by the DNA tetrahedron is calculated as:

$$F = 3\sqrt{2/3}\pi d\sigma cos\,\theta$$

where F is the downward fraction of capillary force on the DNA tetrahedron,

d is the diameter of the DNA rod, *i.e.* 11.5 nm from the TEM results,

σ is the surface tension of the 9/1 (*v/v*) ethanol/water solution, *i.e.* 23.23mN/m at 20 ^{o}C

θ is the contact angle of DNA in 9/1 (v/v) ethanol/water solution. Here, we assume it to be 0 for estimation.

Thus, the equation gives the downward fraction of capillary force on the DNA tetrahedron as 2.1 nN.

2. During drying, water outside of the DNA tetrahedral evaporates and leaves the DNA tetrahedral frame filled with the 9/1 (v/v) ethanol/water solution (Figure 39B). In this case, the capillary force is generated by the surface tension at the liquid-gas-DNA interface, on the DNA rod, and is pointing towards the center of the tetrahedron. The capillary force on each DNA rod is calculated as:

$$F = 2\sqrt{2/3}a\sigma cos\,\theta$$

where F is the capillary force on the DNA rod,

a is the length of the DNA rod, *i.e.* 100 nm,

σ is the surface tension of the 9/1 (*v/v*) ethanol/water solution, *i.e.* 23.23mN/m at 20 ^{o}C

θ is the contact angle of DNA in 9/1 (v/v) ethanol/water solution. Here, we assume it to be 0 for estimation.

Thus, the equation gives the capillary force as 3.8 nN on each rod, pointing to the tetrahedral center.

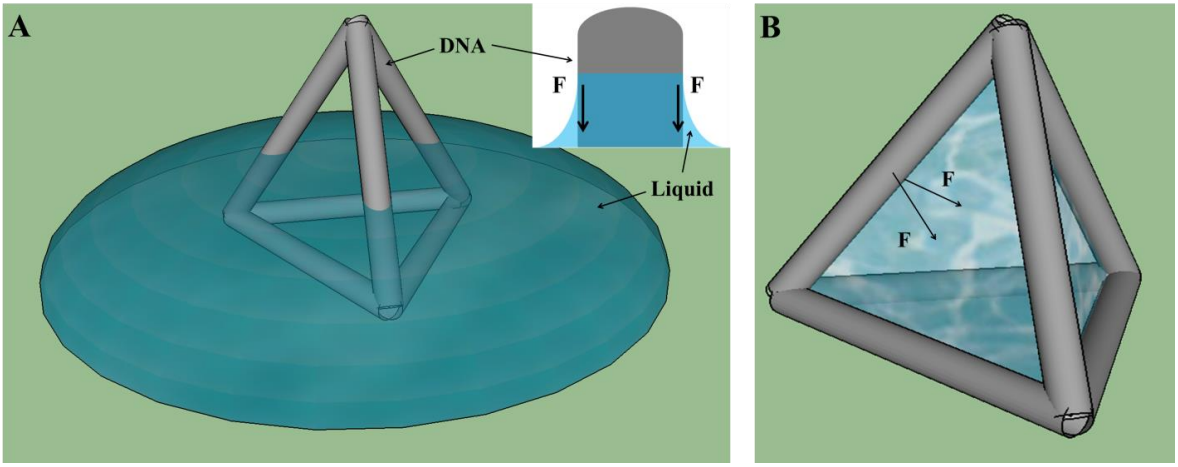

Figure 39. Two models of DNA tetrahedron during the evaporation of water. (A) Water evaporates and exposes the apex of the DNA tetrahedral above the water meniscus. (B) Water outside of the DNA tetrahedral evaporates and leaves the DNA tetrahedral frame filled with water.

4.5.2 Estimation of the density of uranyl strengthened DNA tetrahedron

The average molecular weight of the deoxyribonucleic acid base is 324.5 and the DNA tetrahedron is 20 MD. The number of phosphate groups in a DNA tetrahedron is about 6k. Supposing one uranyl ion (UO_2^{2+}) binds to each phosphate group in DNA,[171] the molecular weight of attached uranyl ions is about 16.6 MD. The effective volume of the DNA nanostructure is assumed to be the volume of the cylinder containing the DNA tetrahedron, which is 8.6 x 10^{-22} m^3. Then the density of strengthened DNA tetrahedron calculated to be 70.7 kg/m^3.

4.5.3 Calculation of effective hardness and Young's modulus of the free-standing DNA tetrahedron

To further understand the excellence of this free-standing nanostructure, hardness/density and stiffness/density was investigated. The effective hardness and Young's modulus of the nanostructure were defined by:

$$\sigma = F/A_0$$

$$E = \frac{F/A_0}{\Delta L/L_0}$$

where

F is the collapsing force collected from the force mapping

A_0 is the effective surface area that the free-standing tetrahedrons covered; $A_0 = 100^2 \times \sqrt{3/4}$ nm^2

E is the Young's modulus (modulus of elasticity)

ΔL is the displacement in the linear force response before collapsing

L_0 is the displacement between the point-contact and unloading

4.5.4 Euler Buckling analysis of the Young's modulus of the individual rod in the DNA tetrahedron

The axial load (F) on the column is the axial component of the collapsing force (F_C) applied on the top apex of DNA tetrahedron from the AFM tip, which is

$$F = F_C/\sqrt{6}$$

The critical force loaded on the column can also be calculated using Euler Buckling formula

$$F = \frac{\pi^2 EI}{(KL)^2}$$

Where E = Young's modulus,

I = area moment of inertia of the cross section of the rod with a radius r (5.8 nm), which is $1/4\pi r^4$.

L = unsupported length of DNA rod (100 nm).

K = column effective length factor. In the case of the DNA rod, the bottom end is fixed on the ground and the top end is free to move laterally, so K = 2.0.

4.6 CONCLUSION

By absorbing uranyl acetate on a DNA frame followed by lyophilization, a DNA tetrahedral structure can be maintained after the drying procedure. With our method, we are the first to convert the 3D DNA nanostructure with high precision to free-standing low-density, high-strength material. The superior mechanical properties were provided by the thin film of uranyl acetate absorbed on the DNA frame by the binding between UO_2^{2+} and phosphate group in DNA. Thanks to the programmable and precise control of DNA nanotechnology, our free-standing 3D DNA nanostructure can offer more versatile shape and better design for the hierarchical lattice material. This work lays the foundation for the future exploration of free-standing and medium free structural properties of presumably soft nanostructure, including DNA framework multi-way junctions.

5.0 SUMMARY AND OUTLOOK

5.1 SUMMARY

In this dissertation, I have demonstrated our effort in addressing the challenge of the limited stability of DNA nanostructures and showed direct nanofabrication processes with the faithful preservation of structural information of DNA nanostructure.

In chapter two, I reported the study of the kinetic behavior of the DNA-mediated HF etching of SiO_2. This vapor phase etching is favorable in that it offers mild conditions that will not lift off or destroy the DNA nanostructure. The DNA can enhance the adsorption of water near its vicinity in nanoscale during the etching. There are several parameters affecting the selectivity of etching and the outcome of the pattern transfer, such as temperature, pressure, relative composition of gas phase etchants, and duration of etching. After systematic study of each parameter, I identified the optimized pattern transfer condition to produce 11 nm resolution patterns with high contrast. The as-patterned SiO_2 layer could also be used as a hard mask to produce sub-20 nm features in the Si substrate by plasma etching. These results highlight the potential application of DNA nanostructures as a template for general-purpose nanofabrication.

In chapter three, we have overcome the limited thermal stability of DNA nanostructures by covering DNA with a protective film. In this case, the DNA nanostructure is not only the template, but also the material source for fabrication of carbon nanostructures. The 20 nm Al_2O_3

coating, prepared by ALD, is a perfect protective film for shape and material preservation of DNA nanostructure at high temperature. 1D and 2D DNA nanostructures in different scales can be converted to carbon nanostructure with the same shape through high temperature annealing. The resulting carbon nanostructure is stable enough to store in an ambient environment for over a month and mechanically stable under AFM imaging conditions. It is not thermally stable either under laser illumination in air or at 800 ^{o}C in H_2, however. Our work showed a new direction to apply the DNA nanostructures as material templates for high temperature solid state chemistries.

In chapter four, I reported that by absorbing uranyl acetate on a DNA frame followed by lyophilization, the mechanical property of DNA tetrahedral structure was improved significantly, at least two orders of magnitudes higher than the reported value in literature. This is the first report of obtaining 3D hollow DNA nanostructure after the drying procedure, and the capillary force is only 1/10 of the collapsing force threshold of the 3D DNA tetrahedron prepared with our method. The structural information of free-standing DNA nanostructure was maintained with high precision. The free-standing 3D hollow DNA structure is a low-density, high-strength material, comparable to the brittle nanolattice.[126] The superior mechanical properties were provided by the thin film of uranyl acetate absorbed on the DNA frame by the binding between UO_2^{2+} and phosphate group in DNA. Our method can offer a more versatile shape and better design for the hierarchical lattice material from programmbly-shape DNA nanostructure. Since a lot of fabrication methods are solid-state chemistry, such as ALD and lithography, this work lays the foundation for the future exploration of nanofabrication using 3D DNA nanostructure.

In summary, we reported various methods to address the major challenge in limited stability of DNA nanostructure in direct nanofabrication. The labile chemical stability can be resolved by selecting the proper conditions for etching; the poor thermal stability can be resolved

by covering with a protective film; and the limited mechanical property can be improved by absorbing uranyl acetate and lyophilization. With our methods, we have demonstrated the direct nanofabrication of different material structures from 1D, 2D, and 3D DNA nanostructures. Our work defines the fundamental principles and creates new frontiers for researchers to use DNA nanostructures for nanoscale fabrication with precise control and high resolution.

5.2 FUTURE PERSPECTIVE

The successful nanofabrication using DNA nanostructure discussed above will lead to many new opportunities and innovative applications. In the following section, I will discuss the potential of DNA based nanofabrication beyond our work in this dissertation.

5.2.1 Fabrication of semiconductor nanostructure from DNA nanostructure

DNA nanostructures contain not only the rich structural information, but also chemical material. The DNA double helix is made of a phosphate backbone, sugar, and 4 bases. In the meantime, the metal cation and charge-compensating anion are also introduced to the system during the synthesis and deposition of the DNA nanostructure. We can not only convert the organic components to porous carbon material by shape-conserving carbonization, but also produce other inorganic material from the DNA nanostructure. Due to the limited stability, the organic components of DNA nanostructure would degrade over 300 ^{o}C or after UV/O_3 treatment.[49, 52] However, the shape of the nanostructure can be preserved identically in these environments, even over 800 ^{o}C. In this scenario, the resulting DNA-shaped nanostructure consists of salt

residue, including Mg, following decomposition of DNA.[49, 52] Considering that the phosphate group in DNA will not be desorbed from the substrate during room temperature oxidation, we could obtain metal phosphate nanostructure after the removal of organic components of DNA with UV/O_3 treatment. The Mg salt could be substituted by other divalent transitional metal cation, such as Ni^{2+}, to serve as charge balance cation. The resulting nickel phosphate structure could be reduced by a gas phase reduction to produce nickel phosphide (Ni_2P) nanostructure, which is a fascinating semiconductor material widely used in electronics and catalysis applications.[173]

5.2.2 Nanofabrication based on free-standing 3D DNA nanostructure

Because the 2D nanofabrication has reached a bottleneck to obtain higher efficiency to generate higher resolution material on the planar surface at a reasonable cost, people have turned to 3D nanofabrication for more opportunities. The fabrication of 3D storage structure is able to achieve larger storage volume at lower cost. In addition, many 3D nanostructures have unique properties for designed-based application. For example, a nanoscale carbon-based truss structure could offer a high strength-to-weight ratio.[174] Arrays of 2D nanoscale crosses and 3D coils could offer novel photonic response and energy-absorbing properties, respectively.[175, 176] However, the fabrication of these irregularly shaped nanostructure is extremely challenging using existing approaches.

Recent structural DNA nanotechnology is able to generate arbitrarily-shaped 3D DNA nanostructure with numerous complexities, suitable for the applications discussed above. However, the 3D DNA based nanofabrication has been limited in the solution phase metallization and many fabrication methods, such as ALD and lithography, are solid-state

chemistry in dry environment. With our method of producing a free-standing DNA tetrahedron, the nanofabrication using 3D DNA is freed from solution and leads to a wider range of opportunities. For example, one can generate higher strength material by ALD of ceramic material onto the free-standing DNA tetrahedron. One can also produce the 3D porous carbon material from the free-standing 3D DNA nanostructure by shape-conserving carbonization. Furthermore, after self-assembly of various compositions of materials on the 3D DNA nanostructure, our method allows it to be used as 3D integrated circuits or 3D NAND.

In summary, the structural DNA nanotechnology provides highly versatile methods for building 2D and 3D nanostructures of quite remarkable complexity, which are ideal templates for design-based nanofabrication. With proper treatment, the nanofabrication based on these DNA nanostructures would have a wide range of applications in nanoelectronics, nanophotonics, mechanical actuation, and energy storage.

BIBLIOGRAPHY

1. Endo, M.; Sugiyama, H. Chemical Approaches to DNA Nanotechnology. *ChemBioChem* **2009,** *10*, 2420-2443.

2. Becerril, H. A.; Woolley, A. T. DNA-templated nanofabrication. *Chem. Soc. Rev.* **2009,** *38*, 329-337.

3. Dietz, H.; Douglas, S. M.; Shih, W. M. Folding DNA into Twisted and Curved Nanoscale Shapes. *Science* **2009,** *325*, 725-730.

4. Douglas, S. M.; Dietz, H.; Liedl, T.; Hogberg, B.; Graf, F.; Shih, W. M. Self-assembly of DNA into nanoscale three-dimensional shapes. *Nature* **2009,** *459*, 414-418.

5. Yang, D.; Campolongo, M. J.; Tran, T. N. N.; Ruiz, R. C. H.; Kahn, J. S.; Luo, D. Novel DNA materials and their applications. *Wiley Interdiscip. Rev. Nanomed. Nanobiotechnol.* **2010,** *2*, 648-669.

6. Han, D.; Pal, S.; Nangreave, J.; Deng, Z.; Liu, Y.; Yan, H. DNA origami with complex curvatures in three-dimensional space. *Science* **2011,** *332*, 342-6.

7. Pinheiro, A. V.; Han, D.; Shih, W. M.; Yan, H. Challenges and opportunities for structural DNA nanotechnology. *Nat. Nanotechnol.* **2011,** *6*, 763-772.

8. Zhang, G.; Surwade, S. P.; Zhou, F.; Liu, H. DNA nanostructure meets nanofabrication. *Chem. Soc. Rev.* **2013,** *42*, 2488-2496.

9. Rothemund, P. W. K. Folding DNA to create nanoscale shapes and patterns. *Nature* **2006,** *440*, 297-302.

10. Yang, Y.; Han, D.; Nangreave, J.; Liu, Y.; Yan, H. DNA Origami with Double-Stranded DNA As a Unified Scaffold. *Acs Nano* **2012**.

11. Zheng, J.; Birktoft, J. J.; Chen, Y.; Wang, T.; Sha, R.; Constantinou, P. E.; Ginell, S. L.; Mao, C.; Seeman, N. C. From molecular to macroscopic via the rational design of a self-assembled 3D DNA crystal. *Nature* **2009,** *461*, 74-77.

12. He, Y.; Chen, Y.; Liu, H. P.; Ribbe, A. E.; Mao, C. D. Self-assembly of hexagonal DNA two-dimensional (2D) arrays. *J. Am. Chem. Soc.* **2005,** *127*, 12202-12203.

13. Hung, A. M.; Noh, H.; Cha, J. N. Recent advances in DNA-based directed assembly on surfaces. *Nanoscale* **2010,** *2*, 2530-2537.

14. Gerdon, A. E.; Oh, S. S.; Hsieh, K.; Ke, Y.; Yan, H.; Soh, H. T. Controlled Delivery of DNA Origami on Patterned Surfaces. *Small* **2009,** *5*, 1942-1946.

15. Kershner, R. J.; Bozano, L. D.; Micheel, C. M.; Hung, A. M.; Fornof, A. R.; Cha, J. N.; Rettner, C. T.; Bersani, M.; Frommer, J.; Rothemund, P. W. K.; Wallraff, G. M. Placement and orientation of individual DNA shapes on lithographically patterned surfaces. *Nat. Nanotechnol.* **2009,** *4*, 557-561.

16. Seeman, N. C. Nucleic acid junctions and lattices. *J. Theoret. Biol.* **1982,** *99*, 237-247.

17. Mao, C.; Sun, W.; Seeman, N. C. Designed two-dimensional DNA Holliday junction arrays visualized by atomic force microscopy. *J. Am. Chem. Soc.* **1999,** *121*, 5437-5443.

18. Fu, J.; Liu, M.; Liu, Y.; Yan, H. Spatially-interactive biomolecular networks organized by nucleic acid nanostructures. *Acc. Chem. Res.* **2012,** *45*, 1215-1226.

19. Yan, H.; Park, S. H.; Finkelstein, G.; Reif, J. H.; LaBean, T. H. DNA-templated self-assembly of protein arrays and highly conductive nanowires. *Science* **2003,** *301*, 1882-1884.

20. Fu, T. J.; Seeman, N. C. DNA double-crossover molecules. *Biochemistry* **1993,** *32*, 3211-3220.

21. Mathieu, F.; Liao, S.; Kopatsch, J.; Wang, T.; Mao, C.; Seeman, N. C. Six-helix bundles designed from DNA. *Nano. Lett.* **2005,** *5*, 661-665.

22. Park, S. H.; Barish, R.; Li, H.; Reif, J. H.; Finkelstein, G.; Yan, H.; LaBean, T. H. Three-helix bundle DNA tiles self-assemble into 2D lattice or 1D templates for silver nanowires. *Nano. Lett.* **2005,** *5*, 693-696.

23. Shih, W. M.; Quispe, J. D.; Joyce, G. F. A 1.7-kilobase single-stranded DNA that folds into a nanoscale octahedron. *Nature* **2004,** *427*, 618-621.

24. Goodman, R. P.; Schaap, I. A. T.; Tardin, C. F.; Erben, C. M.; Berry, R. M.; Schmidt, C. F.; Turberfield, A. J. Rapid Chiral Assembly of Rigid DNA Building Blocks for Molecular Nanofabrication. *Science* **2005,** *310*, 1661-1665.

25. Chen, J.; Seeman, N. C. Synthesis from DNA of a molecule with the connectivity of a cube. *Nature* **1991,** *350*, 631-633.

26. He, Y.; Ye, T.; Su, M.; Zhang, C.; Ribbe, A. E.; Jiang, W.; Mao, C. Hierarchical self-assembly of DNA into symmetric supramolecular polyhedra. *Nature* **2008,** *452*, 198-201.

27. Andersen, E. S.; Dong, M.; Nielsen, M. M.; Jahn, K.; Lind-Thomsen, A.; Mamdouh, W.; Gothelf, K. V.; Besenbacher, F.; Kjems, J. DNA origami design of dolphin-shaped structures with flexible tails. *ACS Nano* **2008,** *2*, 1213-8.

28. Douglas, S. M.; Marblestone, A. H.; Teerapittayanon, S.; Vazquez, A.; Church, G. M.; Shih, W. M. Rapid prototyping of 3D DNA-origami shapes with caDNAno. *Nuc. Acids Res.* **2009,** *37*, 5001-6.

29. Zhang, H. L.; Chao, J.; Pan, D.; Liu, H. J.; Huang, Q.; Fan, C. H. Folding super-sized DNA origami with scaffold strands from long-range PCR. *Chem. Commun.* **2012,** *48*, 6405-6407.

30. Douglas, S. M.; Bachelet, I.; Church, G. M. A logic-gated nanorobot for targeted transport of molecular payloads. *Science* **2012,** *335*, 831-834.

31. Lin, C.; Jungmann, R.; Leifer, A. M.; Li, C.; Levner, D.; Church, G. M.; Shih, W. M.; Yin, P. Submicrometre geometrically encoded fluorescent barcodes self-assembled from DNA. *Nat. Chem.* **2012,** *4*, 832-839.

32. Jungmann, R.; Avendano, M. S.; Woehrstein, J. B.; Dai, M.; Shih, W. M.; Yin, P. Multiplexed 3D cellular super-resolution imaging with DNA-PAINT and Exchange-PAINT. *Nat. Meth.* **2014,** *11*, 313-318.

33. Scheible, M. B.; Ong, L. L.; Woehrstein, J. B.; Jungmann, R.; Yin, P.; Simmel, F. C. A Compact DNA Cube with Side Length 10 nm. *Small* **2015,** *11*, 5200-5205.

34. Sun, W.; Boulais, E.; Hakobyan, Y.; Wang, W. L.; Guan, A.; Bathe, M.; Yin, P. Casting inorganic structures with DNA molds. *Science* **2014,** *346*.

35. Pilo-Pais, M.; Goldberg, S.; Samano, E.; Labean, T. H.; Finkelstein, G. Connecting the nanodots: programmable nanofabrication of fused metal shapes on DNA templates. *Nano. Lett.* **2011,** *11*, 3489-92.

36. Liu, J.; Geng, Y.; Pound, E.; Gyawali, S.; Ashton, J. R.; Hickey, J.; Woolley, A. T.; Harb, J. N. Metallization of branched DNA origami for nanoelectronic circuit fabrication. *ACS Nano* **2011,** *5*, 2240-7.

37. Maune, H. T.; Han, S.-p.; Barish, R. D.; Bockrath, M.; Goddard, I. I. A.; RothemundPaul, W. K.; Winfree, E. Self-assembly of carbon nanotubes into two-dimensional geometries using DNA origami templates. *Nat. Nanotechnol.* **2010,** *5*, 61-66.

38. Wei, B.; Dai, M.; Yin, P. Complex shapes self-assembled from single-stranded DNA tiles. *Nature* **2012,** *485*, 623-626.

39. Mathur, D.; Henderson, E. R. Complex DNA Nanostructures from Oligonucleotide Ensembles. *ACS Synth. Biol.* **2013,** *2*, 180-185.

40. Ke, Y.; Ong, L. L.; Shih, W. M.; Yin, P. Three-Dimensional Structures Self-Assembled from DNA Bricks. *Science* **2012,** *338*, 1177-1183.

41. Ke, Y.; Ong, L. L.; Sun, W.; Song, J.; Dong, M.; Shih, W. M.; Yin, P. DNA brick crystals with prescribed depths. *Nat. Chem.* **2014,** *6*, 994-1002.

42. Surwade, S. P.; Zhou, F.; Wei, B.; Sun, W.; Powell, A.; O'Donnell, C.; Yin, P.; Liu, H. Nanoscale Growth and Patterning of Inorganic Oxides Using DNA Nanostructure Templates. *J. Am. Chem. Soc.* **2013,** *135*, 6778-6781.

43. Jin, Z.; Sun, W.; Ke, Y.; Shih, C.-J.; Paulus, G. L.; Wang, Q. H.; Mu, B.; Yin, P.; Strano, M. S. Metallized DNA nanolithography for encoding and transferring spatial information for graphene patterning. *Nat. Commun.* **2013,** *4*, 1663.

44. Endo, M.; Sugita, T.; Katsuda, Y.; Hidaka, K.; Sugiyama, H. Programmed ‐ assembly system using DNA jigsaw pieces. *Chem. Eur. J.* **2010,** *16*, 5362-5368.

45. Woo, S.; Rothemund, P. W. Programmable molecular recognition based on the geometry of DNA nanostructures. *Nat. Chem.* **2011,** *3*, 620-7.

46. Iinuma, R.; Ke, Y.; Jungmann, R.; Schlichthaerle, T.; Woehrstein, J. B.; Yin, P. Polyhedra Self-Assembled from DNA Tripods and Characterized with 3D DNA-PAINT. *Science* **2014,** *344*, 65-69.

47. Kershner, R. J.; Bozano, L. D.; Micheel, C. M.; Hung, A. M.; Fornof, A. R.; Cha, J. N.; Rettner, C. T.; Bersani, M.; Frommer, J.; Rothemund, P. W. K.; Wallraff, G. M. Placement and orientation of individual DNA shapes on lithographically patterned surfaces. *Nat Nano* **2009,** *4*, 557-561.

48. Gates, K. S. An Overview of Chemical Processes That Damage Cellular DNA: Spontaneous Hydrolysis, Alkylation, and Reactions with Radicals. *Chem. Res. Toxicol.* **2009,** *22*, 1747-1760.

49. Kim, H.; Surwade, S. P.; Powell, A.; O'Donnell, C.; Liu, H. Stability of DNA Origami Nanostructure under Diverse Chemical Environments. *Chem. Mater.* **2014,** *26*, 5265-5273.

50. Lindahl, T. Instability and decay of the primary structure of DNA. *Nature* **1993,** *362*, 709-715.

51. Lindahl, T.; Nyberg, B. Rate of depurination of native deoxyribonucleic acid. *Biochemistry* **1972,** *11*, 3610-3618.

52. Zhou, F.; Michael, B.; Surwade, S. P.; Ricardo, K. B.; Zhao, S.; Liu, H. Mechanistic Study of the Nanoscale Negative-Tone Pattern Transfer from DNA Nanostructures to SiO2. *Chem. Mater.* **2015,** *27*, 1692-1698.

53. Mogab, C. J.; Adams, A. C.; Flamm, D. L. Plasma etching of Si and SiO<inf>2</inf>—The effect of oxygen additions to CF<inf>4</inf> plasmas. *J. Appl. Phys* **1978,** *49*, 3796-3803.

54. Braun, E.; Eichen, Y.; Sivan, U.; Ben-Yoseph, G. DNA-templated assembly and electrode attachment of a conducting silver wire. *Nature* **1998,** *391*, 775-778.

55. Liu, J.; Geng, Y.; Pound, E.; Gyawali, S.; Ashton, J. R.; Hickey, J.; Woolley, A. T.; Harb, J. N. Metallization of Branched DNA Origami for Nanoelectronic Circuit Fabrication. *ACS Nano* **2011,** *5*, 2240-2247.

56. Schreiber, R.; Kempter, S.; Holler, S.; Schüller, V.; Schiffels, D.; Simmel, S. S.; Nickels, P. C.; Liedl, T. DNA Origami-Templated Growth of Arbitrarily Shaped Metal Nanoparticles. *Small* **2011,** *7*, 1795-1799.

57. Tagawa, M.; Shohda, K.-i.; Fujimoto, K.; Suyama, A. Stabilization of DNA nanostructures by photo-cross-linking. *Soft. Matter.* **2011,** *7*, 10931-10934.

58. Kuzyk, A.; Schreiber, R.; Fan, Z.; Pardatscher, G.; Roller, E.-M.; Hoegele, A.; Simmel, F. C.; Govorov, A. O.; Liedl, T. DNA-based self-assembly of chiral plasmonic nanostructures with tailored optical response. *Nature* **2012,** *483*, 311-314.

59. Pearson, A. C.; Liu, J.; Pound, E.; Uprety, B.; Woolley, A. T.; Davis, R. C.; Harb, J. N. DNA Origami Metallized Site Specifically to Form Electrically Conductive Nanowires. *J. Phys. Chem. B* **2012,** *116*, 10551-10560.

60. Pilo-Pais, M.; Goldberg, S.; Samano, E.; LaBean, T. H.; Finkelstein, G. Connecting the Nanodots: Programmable Nanofabrication of Fused Metal Shapes on DNA Templates. *Nano Letters* **2011,** *11*, 3489-3492.

61. Deng, Z.; Mao, C. Molecular Lithography with DNA Nanostructures. *Angew. Chem. Int. Ed.* **2004,** *43*, 4068-4070.

62. Becerril, H. A.; Woolley, A. T. DNA shadow nanolithography. *Small* **2007,** *3*, 1534-1538.

63. He, Y.; Ye, T.; Ribbe, A. E.; Mao, C. DNA-Templated Fabrication of Two-Dimensional Metallic Nanostructures by Thermal Evaporation Coating. *J. Am. Chem. Soc.* **2011,** *133*, 1742-1744.

64. Khandelwal, G.; Bhyravabhotla, J. A Phenomenological Model for Predicting Melting Temperatures of DNA Sequences. *PLoS ONE* **2010,** *5*, e12433.

65. Aoi, K.; Takasu, A.; Okada, M. DNA-based polymer hybrids Part 1. Compatibility and physical properties of poly(vinyl alcohol)/DNA sodium salt blend. *Polymer* **2000,** *41*, 2847-2853.

66. Zhang, G.; Surwade, S. P.; Zhou, F.; Liu, H. DNA nanostructure meets nanofabrication. *Chem. Soc. Rev.* **2013,** *42*, 2488-2496.

67. He, Y.; Liu, H.; Chen, Y.; Tian, Y.; Deng, Z.; Ko, S. H.; Ye, T.; Mao, C. DNA-based nanofabrications. *Microsc. Res. Techniq.* **2007,** *70*, 522-529.

68. Surwade, S. P.; Zhao, S.; Liu, H. Molecular Lithography through DNA-Mediated Etching and Masking of SiO2. *J. Am. Chem. Soc.* **2011,** *133*, 11868-11871.

69. Becerril, H. A.; Woolley, A. T. DNA-templated nanofabrication. *Chemical Society Reviews* **2009,** *38*, 329-337.

70. Pilo-Pais, M.; Goldberg, S.; Samano, E.; LaBean, T. H.; Finkelstein, G. Connecting the Nanodots: Programmable Nanofabrication of Fused Metal Shapes on DNA Templates. *Nano Lett.* **2011,** *11*, 3489-3492.

71. Carta, G.; El Habra, N.; Crociani, L.; Rossetto, G.; Zanella, P.; Zanella, A.; Paolucci, G.; Barreca, D.; Tondello, E. CVD of MgO Thin Films from Bis(methylcyclopentadienyl) Magnesium. *Chem. Vap. Deposition* **2007,** *13*, 185-189.

72. Lim, B. S.; Rahtu, A.; Gordon, R. G. Atomic layer deposition of transition metals. *Nat. Mater.* **2003,** *2*, 749-754.

73. Niinisto, J.; Putkonen, M.; Niinisto, L.; Stoll, S. L.; Kukli, K.; Sajavaara, T.; Ritala, M.; Leskela, M. Controlled growth of HfO2 thin films by atomic layer deposition from cyclopentadienyl-type precursor and water. *J. Mater. Chem.* **2005,** *15*, 2271-2275.

74. Lin, Y.; Shen, X.; Wang, J.; Bao, L.; Zhang, Z.; Pang, D. Measuring radial Young's modulus of DNA by tapping mode AFM. *Chin. Sci. Bull.* **2007,** *52*, 3189-3192.

75. Cocco, S.; Marko, J. F.; Monasson, R. Theoretical models for single-molecule DNA and RNA experiments: from elasticity to unzipping. *C. R. Phys.* **2002,** *3*, 569-584.

76. Marko, J. F.; Cocco, S. The micromechanics of DNA. *Phys. World* **2003,** *16*, 37-41.

77. Kauert, D. J.; Kurth, T.; Liedl, T.; Seidel, R. Direct Mechanical Measurements Reveal the Material Properties of Three-Dimensional DNA Origami. *Nano. Lett.* **2011,** *11*, 5558-5563.

78. Pfitzner, E.; Wachauf, C.; Kilchherr, F.; Pelz, B.; Shih, W. M.; Rief, M.; Dietz, H. Rigid DNA Beams for High-Resolution Single-Molecule Mechanics. *Angew. Chem.* **2013,** *125*, 7920-7925.

79. Weizmann, Y.; Braunschweig, A. B.; Wilner, O. I.; Cheglakov, Z.; Willner, I. A polycatenated DNA scaffold for the one-step assembly of hierarchical nanostructures. *Proc. Natl. Acad. Sci.* **2008,** *105*, 5289-5294.

80. Smith, D. M.; Schuller, V.; Forthmann, C.; Schreiber, R.; Tinnefeld, P.; Liedl, T. A Structurally Variable Hinged Tetrahedron Framework from DNA Origami. *J. Nuc. Acids* **2011,** *2011*, 9.

81. Tian, C.; Li, X.; Liu, Z.; Jiang, W.; Wang, G.; Mao, C. Directed Self-Assembly of DNA Tiles into Complex Nanocages. *Angew. Chem.* **2014,** *126*, 8179-8182.

82. Zhang, C.; Su, M.; He, Y.; Zhao, X.; Fang, P.-a.; Ribbe, A. E.; Jiang, W.; Mao, C. Conformational flexibility facilitates self-assembly of complex DNA nanostructures. *Proc. Natl. Acad. Sci.* **2008,** *105*, 10665-10669.

83. Zhang, C.; Ko, S. H.; Su, M.; Leng, Y.; Ribbe, A. E.; Jiang, W.; Mao, C. Symmetry Controls the Face Geometry of DNA Polyhedra. *J. Am. Chem. Soc.* **2009,** *131*, 1413-1415.

84. Andersen, E. S.; Dong, M.; Nielsen, M. M.; Jahn, K.; Subramani, R.; Mamdouh, W.; Golas, M. M.; Sander, B.; Stark, H.; Oliveira, C. L. P.; Pedersen, J. S.; Birkedal, V.; Besenbacher, F.; Gothelf, K. V.; Kjems, J. Self-assembly of a nanoscale DNA box with a controllable lid. *Nature* **2009,** *459*, 73-76.

85. Whidden, T. K.; Allgair, J.; Ryan, J. M.; Kozicki, M. N.; Ferry, D. K. Catalyzed HF Vapor Etching of Silicon Dioxide for Microlithographic and Nanolithographic Masks. *J. Electrochem. Soc.* **1995,** *142*, 1199-1205.

86. Allgair, J.; Ryan, J. M.; Song, H. J.; Kozicki, M. N.; Whidden, T. K.; Ferry, D. K. Nanoscale patterning of silicon dioxide thin films by catalyzed HF vapor etching. *Nanotechnology* **1996,** *7*, 351-355.

87. Anguita, J.; Briones, F. HF/H2O vapor etching of SiO2 sacrificial layer for large-area surface-micromachined membranes. *Sens. Actuators, A* **1998,** *64*, 247-251.

88. Kang, J. K.; Musgrave, C. B. The mechanism of HF/H2O chemical etching of SiO2. *J. Chem. Phys.* **2002,** *116*, 275-280.

89. Lee, C. S.; Baek, J. T.; Yoo, H. J.; Woo, S. I. Modeling and characterization of gas-phase etching of thermal oxide and TEOS oxide using anhydrous HF and CH3OH. *J. Electrochem. Soc.* **1996,** *143*, 1099-1103.

90. Mizushima, S. Determination of the amount of gas adsorption on SiO2/Si(100) surfaces to realize precise mass measurement. *Metrologia* **2004,** *41*, 137-144.

91. Balkose, D.; Alp, B.; Ulku, S. Water vapour adsorption on DNA. *J. Therm. Anal. Calorim.* **2008,** *94*, 695-698.

92. Watanabe, H.; Kitajima, H.; Honma, I.; Ona, H.; Wilhelm, R. J.; Sophie, A. J. L. Influence of Water Adsorption/Desorption Processes on the Selectivity of Vapor HF Etching. *J. Electrochem. Soc.* **1995,** *142*, 1332-1340.

93. Gui, X. C.; Wei, J. Q.; Wang, K. L.; Cao, A. Y.; Zhu, H. W.; Jia, Y.; Shu, Q. K.; Wu, D. H. Carbon Nanotube Sponges. *Adv. Mater.* **2010,** *22*, 617-+.

94. Frackowiak, E.; Beguin, F. Carbon materials for the electrochemical storage of energy in capacitors. *Carbon* **2001,** *39*, 937-950.

95. Gallego, N. C.; Klett, J. W. Carbon foams for thermal management. *Carbon* **2003,** *41*, 1461-1466.

96. Klett, J.; Hardy, R.; Romine, E.; Walls, C.; Burchell, T. High-thermal-conductivity, mesophase-pitch-derived carbon foams: effect of precursor on structure and properties. *Carbon* **2000,** *38*, 953-973.

97. Zhang, L. L.; Zhao, X. S. Carbon-based materials as supercapacitor electrodes. *Chem. Soc. Rev.* **2009,** *38*, 2520-2531.

98. Balandin, A. A. Thermal properties of graphene and nanostructured carbon materials. *Nat. Mater.* **2011,** *10*, 569-581.

99. Ji, X. L.; Lee, K. T.; Nazar, L. F. A highly ordered nanostructured carbon-sulphur cathode for lithium-sulphur batteries. *Nat. Mater.* **2009,** *8*, 500-506.

100. Chesnokov, S. A.; Nalimova, V. A.; Rinzler, A. G.; Smalley, R. E.; Fischer, J. E. Mechanical energy storage in carbon nanotube springs. *Phys. Rev. Lett.* **1999,** *82*, 343-346.

101. Sazanov, Y. N.; Gribanov, A. V. Criteria of polymer carbonization. *Russ. J. Appl. Chem+.* **2009,** *82*, 473-482.

102. Lee, J.; Kim, J.; Hyeon, T. Recent progress in the synthesis of porous carbon materials. *Adv. Mater.* **2006,** *18*, 2073-2094.

103. Xia, Y. D.; Yang, Z. X.; Mokaya, R. Templated nanoscale porous carbons. *Nanoscale* **2010,** *2*, 639-659.

104. Sakintuna, B.; Yurum, Y. Templated porous carbons: A review article. *Ind. Eng. Chem. Res.* **2005,** *44*, 2893-2902.

105. Zhang, H. L.; Chao, J.; Pan, D.; Liu, H. J.; Huang, Q.; Fan, C. H. Folding super-sized DNA origami with scaffold strands from long-range PCR. *Chemical Communications* **2012,** *48*, 6405-6407.

106. Wei, B.; Dai, M. J.; Yin, P. Complex shapes self-assembled from single-stranded DNA tiles. *Nature* **2012,** *485*, 623.

107. Zhao, Z.; Liu, Y.; Yan, H. Organizing DNA Origami Tiles into Larger Structures Using Preformed Scaffold Frames. *Nano. Lett.* **2011,** *11*, 2997-3002.

108. Woo, S.; Rothemund, P. W. K. Programmable molecular recognition based on the geometry of DNA nanostructures. *Nat. Chem.* **2011,** *3*, 620-627.

109. Endo, M.; Sugita, T.; Rajendran, A.; Katsuda, Y.; Emura, T.; Hidaka, K.; Sugiyama, H. Two-dimensional DNA origami assemblies using a four-way connector. *Chem. Commun.* **2011,** *47*, 3213-3215.

110. Castro, C. E.; Kilchherr, F.; Kim, D. N.; Shiao, E. L.; Wauer, T.; Wortmann, P.; Bathe, M.; Dietz, H. A primer to scaffolded DNA origami. *Nat. Mater.* **2011,** *8*, 221-229.

111. Seeman, N. C. Nanomaterials Based on DNA. *Annuc. Rev. Biochem.* **2010,** *79*, 65-87.

112. Seeman, N. C. An overview of structural DNA Nanotechnology. *Mol. Biotechnol.* **2007,** *37*, 246-257.

113. Liu, W. Y.; Zhong, H.; Wang, R. S.; Seeman, N. C. Crystalline Two-Dimensional DNA-Origami Arrays. *Angew. Chem. Int. Ed.* **2011,** *50*, 264-267.

114. Nakao, H.; Tokonami, S.; Yamamoto, Y.; Shiigi, H.; Takeda, Y. Fluorescent carbon nanowires made by pyrolysis of DNA nanofibers and plasmon-assisted emission enhancement of their fluorescence. *Chem. Commun.* **2014,** *50*, 11887-11890.

115. Sokolov, A. N.; Yap, F. L.; Liu, N.; Kim, K.; Ci, L. J.; Johnson, O. B.; Wang, H. L.; Vosgueritchian, M.; Koh, A. L.; Chen, J. H.; Park, J.; Bao, Z. N. Direct growth of aligned graphitic nanoribbons from a DNA template by chemical vapour deposition. *Nat. Commun.* **2013,** *4*.

116. Gibson, L. J.; Ashby, M. F. *Cellular solids : structure and properties*. Cambridge University Press: 1997.

117. Fan, H.; Hartshorn, C.; Buchheit, T.; Tallant, D.; Assink, R.; Simpson, R.; Kissel, D. J.; Lacks, D. J.; Torquato, S.; Brinker, C. J. Modulus-density scaling behaviour and framework architecture of nanoporous self-assembled silicas. *Nat. Mater.* **2007,** *6*, 418-423.

118. Qiu, L.; Liu, J. Z.; Chang, S. L. Y.; Wu, Y.; Li, D. Biomimetic superelastic graphene-based cellular monoliths. *Nat. Commun.* **2012,** *3*, 1241.

119. Tillotson, T. M.; Hrubesh, L. W. Transparent ultralow-density silica aerogels prepared by a two-step sol-gel process. *J. Non-Cryst. Solids* **1992,** *145*, 44-50.

120. Kim, S.-H.; Kim, H.; Kim, N. J. Brittle intermetallic compound makes ultrastrong low-density steel with large ductility. *Nature* **2015,** *518*, 77-79.

121. Zheng, X.; Lee, H.; Weisgraber, T. H.; Shusteff, M.; DeOtte, J.; Duoss, E. B.; Kuntz, J. D.; Biener, M. M.; Ge, Q.; Jackson, J. A.; Kucheyev, S. O.; Fang, N. X.; Spadaccini, C. M. Ultralight, ultrastiff mechanical metamaterials. *Science* **2014,** *344*, 1373-1377.

122. Schaedler, T. A.; Jacobsen, A. J.; Torrents, A.; Sorensen, A. E.; Lian, J.; Greer, J. R.; Valdevit, L.; Carter, W. B. Ultralight Metallic Microlattices. *Science* **2011,** *334*, 962-965.

123. Torrents, A.; Schaedler, T. A.; Jacobsen, A. J.; Carter, W. B.; Valdevit, L. Characterization of nickel-based microlattice materials with structural hierarchy from the nanometer to the millimeter scale. *Acta Mater.* **2012,** *60*, 3511-3523.

124. Bauer, J.; Hengsbach, S.; Tesari, I.; Schwaiger, R.; Kraft, O. High-strength cellular ceramic composites with 3D microarchitecture. *Proc. Natl. Acad. Sci.* **2014,** *111*, 2453-2458.

125. Kucheyev, S. O.; Stadermann, M.; Shin, S. J.; Satcher, J. H.; Gammon, S. A.; Letts, S. A.; van Buuren, T.; Hamza, A. V. Super-Compressibility of Ultralow-Density Nanoporous Silica. *Adv. Mater.* **2012,** *24*, 776-780.

126. Meza, L. R.; Das, S.; Greer, J. R. Strong, lightweight, and recoverable three-dimensional ceramic nanolattices. *Science* **2014,** *345*, 1322-1326.

127. Kim, K. H.; Oh, Y.; Islam, M. F. Graphene coating makes carbon nanotube aerogels superelastic and resistant to fatigue. *Nat. Nanotechnol.* **2012,** *7*, 562-566.

128. Cheung, K. C.; Gershenfeld, N. Reversibly Assembled Cellular Composite Materials. *Science* **2013,** *341*, 1219-1221.

129. Worsley, M. A.; Kucheyev, S. O.; Satcher, J. H.; Hamza, A. V.; Baumann, T. F. Mechanically robust and electrically conductive carbon nanotube foams. *Appl. Phys. Lett.* **2009,** *94*, 073115.

130. Jang, D.; Meza, L. R.; Greer, F.; Greer, J. R. Fabrication and deformation of three-dimensional hollow ceramic nanostructures. *Nat. Mater.* **2013,** *12*, 893-898.

131. Meza, L.; Greer, J. Mechanical characterization of hollow ceramic nanolattices. *J. Mater. Sci.* **2014,** *49*, 2496-2508.

132. Biener, M. M.; Ye, J.; Baumann, T. F.; Wang, Y. M.; Shin, S. J.; Biener, J.; Hamza, A. V. Ultra-strong and Low-Density Nanotubular Bulk Materials with Tunable Feature Sizes. *Adv. Mater.* **2014,** *26*, 4808-4813.

133. Winfree, E.; Liu, F.; Wenzler, L. A.; Seeman, N. C. Design and self-assembly of two-dimensional DNA crystals. *Nature* **1998,** *394*, 539-544.

134. Rothemund, P. W. K.; Papadakis, N.; Winfree, E. Algorithmic Self-Assembly of DNA Sierpinski Triangles. *PLoS Biol* **2004,** *2*, e424.

135. Linko, V.; Dietz, H. The enabled state of DNA nanotechnology. *Curr. Opin. Biotechnol.* **2013,** *24*, 555-561.

136. Zhang, Y.; Seeman, N. C. Construction of a DNA-Truncated Octahedron. *J. Am. Chem. Soc.* **1994,** *116*, 1661-1669.

137. Rothemund, P. W. K.; Andersen, E. S. NANOTECHNOLOGY The importance of being modular. *Nature* **2012,** *485*, 584-585.

138. Zhang, G.; Surwade, S. P.; Zhou, F.; Liu, H. DNA nanostructure meets nanofabrication. *Chem. Soc. Rev.* **2013**.

139. Pillers, M. A.; Lieberman, M. Thermal stability of DNA origami on mica. *J. Vac. Sci. Technol. B* **2014,** *32*, -.

140. Surwade, S. P.; Zhao, S.-C.; Liu, H.-T. Molecular lithography through DNA-mediated etching and masking of SiO2. *J. Am. Chem. Soc.* **2011,** *133*, 11868-11871.

141. Vivien, L. *Handbook of silicon photonics*. Boca Raton : CRC Press, Taylor & Francis, [2013]: **2013,** pp, 61.

142. http://www.nupack.org/partition/new_from_job/469528?token=jS0GBkC6kT (accessed December 2015).

143. Hung, A. M.; Micheel, C. M.; Bozano, L. D.; Osterbur, L. W.; Wallraff, G. M.; Cha, J. N. Large-area spatially ordered arrays of gold nanoparticles directed by lithographically confined DNA origami. *Nat. Nanotechnol.* **2010,** *5*, 121-126.

144. http://www.sciencelab.com/msds.php?msdsId=9927321 (accessed December 2015).

145. http://www.sciencelab.com/msds.php?msdsId=9924412 (accessed December 2015).

146. http://www.sciencelab.com/msds.php?msdsId=9924296 (accessed December 2015).

147. http://www.honeywell.com/sites/docs/doc128e30a-f9d1a7e532-e0df9bfada07602278603c6cb43673fb.pdf (accessed December 2015).

148. Anguita, J.; Briones, F. HF/H2O vapor etching of SiO2 sacrificial layer for large-area surface-micromachined membranes. *Sens. Actuators, A-Phys* **1998,** *64*, 247-251.

149. Torek, K.; Ruzyllo, J.; Grant, R.; Novak, R. Reduced Pressure Etching of Thermal Oxides in Anhydrous HF/alcoholic Gas Mixtures. *J. Electrochem. Soc.* **1995,** *142*, 1322-1326.

150. *The Merck index of chemicals and drugs; an encyclopedia for the chemist, pharmacist, physician, and allied professions*. 6 ed.; RAHWAY, N.J., U.S.A.: MERCK & CO., INC., **1952**, pp, 546; p 546.

151. Vig, J. R. UV/ozone cleaning of surfaces. *J. Vac. Sci. Technol. A* **1985,** *3*, 1027-1034.

152. Williams, k. R. Etch Rates for Micromachining Processing. *J. Microelectromech. Syst.* **1996,** *5*, 14.

153. Zhao, Z.; Liu, Y.; Yan, H. Organizing DNA Origami Tiles into Larger Structures Using Preformed Scaffold Frames. *Nano Lett.* **2011,** *11*, 2997-3002.

154. Castro, C. E.; Kilchherr, F.; Kim, D. N.; Shiao, E. L.; Wauer, T.; Wortmann, P.; Bathe, M.; Dietz, H. A primer to scaffolded DNA origami. *Nat. Methods* **2011,** *8*, 221-229.

155. Seeman, N. C. Nanomaterials Based on DNA. *Annu. Rev. Biochem.* **2010,** *79*, 65-87.

156. Han, D. R.; Pal, S.; Nangreave, J.; Deng, Z. T.; Liu, Y.; Yan, H. DNA Origami with Complex Curvatures in Three-Dimensional Space. *Science* **2011,** *332*, 342-346.

157. Sazanov, Y. N.; Gribanov, A. V. Criteria of polymer carbonization. *Russ. J. Appl. Chem+* **2009,** *82*, 473-482.

158. Li, Z.; Wang, Y.; Kozbial, A.; Shenoy, G.; Zhou, F.; McGinley, R.; Ireland, P.; Morganstein, B.; Kunkel, A.; Surwade, S. P.; Li, L.; Liu, H. Effect of airborne contaminants on the wettability of supported graphene and graphite. *Nat. Mater.* **2013,** *12*, 925-931.

159. Park, S.-H. K.; Hwang, C.-S.; Ryu, M.; Yang, S.; Byun, C.; Shin, J.; Lee, J.-I.; Lee, K.; Oh, M. S.; Im, S. Transparent and Photo-stable ZnO Thin-film Transistors to Drive an Active Matrix Organic-Light- Emitting-Diode Display Panel. *Adv. Mater.* **2009,** *21*, 678-682.

160. Zhou, F.; Li, Z.; Shenoy, G. J.; Li, L.; Liu, H. Enhanced Room-Temperature Corrosion of Copper in the Presence of Graphene. *ACS Nano* **2013,** *7*, 6939-6947.

161. Tuinstra, F.; Koenig, J. L. Raman Spectrum of Graphite. *J. Chem. Phys.* **1970,** *53*, 1126-1130.

162. Cançado, L. G.; Takai, K.; Enoki, T.; Endo, M.; Kim, Y. A.; Mizusaki, H.; Jorio, A.; Coelho, L. N.; Magalhães-Paniago, R.; Pimenta, M. A. General equation for the determination of the crystallite size La of nanographite by Raman spectroscopy. *Appl. Phys. Lett.* **2006,** *88*, 163106.

163. Lucchese, M. M.; Stavale, F.; Ferreira, E. H. M.; Vilani, C.; Moutinho, M. V. O.; Capaz, R. B.; Achete, C. A.; Jorio, A. Quantifying ion-induced defects and Raman relaxation length in graphene. *Carbon* **2010,** *48*, 1592-1597.

164. Yu, J.-S.; Yoon, S. B.; Chai, G. S. Ordered uniform porous carbon by carbonization of sugars. *Carbon* **2001,** *39*, 1442-1446.

165. Nemes-Incze, P.; Osváth, Z.; Kamarás, K.; Biró, L. P. Anomalies in thickness measurements of graphene and few layer graphite crystals by tapping mode atomic force microscopy. *Carbon* **2008,** *46*, 1435-1442.

166. Kaburagi, Y.; Hishiyama, Y. Highly Crystallized Graphite Films Prepared by High-Temperature Heat-Treatment from Carbonized Aromatic Polyimide Films. *Carbon* **1995,** *33*, 773-777.

167. Hishiyama, Y.; Yoshida, A.; Kaburagi, Y.; Inagaki, M. Graphite Films Prepared from Carbonized Polyimide Films. *Carbon* **1992,** *30*, 333-337.

168. Heyman, A.; Musgrave, C. B. A Quantum Chemical Study of the Atomic Layer Deposition of Al2O3 Using AlCl3 and H2O as Precursors. *J. Phys. Chem. B* **2004,** *108*, 5718-5725.

169. Smith, D. M.; Sch; #252; ller, V.; Forthmann, C.; Schreiber, R.; Tinnefeld, P.; Liedl, T. A Structurally Variable Hinged Tetrahedron Framework from DNA Origami. *J. Nuc. Acids* **2011,** *2011*, 9.

170. Fleck, N. A.; Deshpande, V. S.; Ashby, M. F. *Micro-architectured materials: past, present and future*. 2010; Vol. 466, p 2495-2516.

171. Hayat, M. A. *Stains and cytochemical methods*. Springer Science & Business Media: 1993, pp. 362.

172. Li, L.; Liu, L.; Tabata, O.; Li, W. In *Elasticity measurement of DNA origami nanotube in liquid with tapping mode AFM*, Nano/Micro Engineered and Molecular Systems (NEMS), 2014 9th IEEE International Conference on, IEEE: 2014; pp 684-687.

173. Wang, A.; Qin, M.; Guan, J.; Wang, L.; Guo, H.; Li, X.; Wang, Y.; Prins, R.; Hu, Y. The synthesis of metal phosphides: reduction of oxide precursors in a hydrogen plasma. *Angew. Chem.* **2008,** *120*, 6141-6143.

174. Deb, K.; Gulati, S. Design of truss-structures for minimum weight using genetic algorithms. *Finite Elem. Anal. Des.* **2001,** *37*, 447-465.

175. Watts, C. M.; Liu, X. L.; Padilla, W. J. Metamaterial Electromagnetic Wave Absorbers. *Adv. Mater.* **2012,** *24*, Op98-Op120.

176. Gansel, J. K.; Thiel, M.; Rill, M. S.; Decker, M.; Bade, K.; Saile, V.; von Freymann, G.; Linden, S.; Wegener, M. Gold Helix Photonic Metamaterial as Broadband Circular Polarizer. *Science* **2009,** *325*, 1513-1515.